Detection of small biomolecules by plasmonic nanoparticles (LSPR sensing)

Dissertation

To Fulfill the
Requirements for the Degree of
"doctor rerum naturalium" (Dr. rer. nat.)

Submitted to the Council of the Faculty
of Biology and Pharmacy
of the Friedrich Schiller University Jena

by Jacqueline Jatschka MSc.

born on 15.03.1988 in Vienna/Austria

Reviewers:

Prof. Dr. Stefan H. Heinemann
Institut für Biochemie und Biophsyik
Friedrich Schiller Universität Jena
Hans-Knöll-Str. 2
07745 Jena
Germany

PD Dr. Wolfgang Fritzsche
Leibniz-Institut für photonische Technologien e.V.
Albert-Einstein-Str. 9
07745 Jena
Germany

Prof. Dr. Colette McDonagh
Department Physical Sciences
Dublin City University
Glasnevin
Dublin 9
Ireland

Day of public defense: April 18t̂h, 2018

"*All things are ready, if our mind be so.*"
– William Shakespeare

Table of Contents

Abbreviations and nomenclature

AFM	Atomic Force Microscopy
ATR	Attenuated Total internal Reflection
Au	gold
BSA	Bovine Serum Albumin
DNA	Deoxyribonucleic Acid
DS	Dextran Sulfate
G-quadruplex	Guanine rich DNA forming a quadruplex
LbL	Layer-by-Layer
LSPR	Localized Surface Plasmon Resonance and setup with densely adsorbed nanostructures
l_d	Penetration depth
MCH	Mercaptohexanol
n_{eff}	Effective refractive index
NP	Nanoparticle
PAH	Poly(allylamine hydrochloride)
PEL	Polyelectrolyte
PCR	Polymerase Chain Reaction
PSA	Pressure Sensitive Adhesive
PSS	Poly(sodium 4-styrenesulfonate)
RIU	Refractive Index Unit
SPR	Surface Plasmon Resonance
SAMs	Self-assembled Monolayers
ssDNA	single-stranded DNA
sLSPR	single noble metal nanoparticle detection
S_b	bulk Sensitivity
S_s	surface Sensitivity
SEM	Scanning Electron Microscope
TEM	Transmission Electron Microscopy
T_m	melting Temperature
λ_{max}	LSPR wavelength maximum

1 Introduction

There is an evident need for the detection of chemical and biological materials in today's world. A wide variety of compounds exist that can be harmful to human health, livestock, plants and the environment in general.

Especially in health care a fast analysis of blood or serum with low-cost devices is of high interest. Diseases diagnosed in an early stage lead to an early treatment and faster cure of patients. Additionally, there is a need to detect low levels of other compounds in the living system induced, for instance, by accidental or intentional poisoning. [1, 2]

During the last 60 years the development of biosensors shows promising results to meet the mentioned today's and future needs. The development of the first biosensor and therefore the start of the detection of biomolecules is stated back to Leland C. Clark, commonly named "father of biosensor". He published his definitive paper [3] on oxygen electrodes in 1956. In the following years he expanded the range of analyte detection by adding enzymes on the surface of the electrode. In 1962 [4], he published the first amperometric enzyme electrode for glucose measurements, which is the basis of the modern-day glucose sensor used by diabetics all over the world.

This first sensing principle was the starting point for a big variety of biosensor concepts. Each biosensor consists of three basic components: biorecognition element (designed for specific binding of an analyte), the transducer (converts the molecular interaction to a measurable physical property) and the auxiliary electronics (to present and interpret the transducer signal). If an analyte is binding to the biorecognition element, a signal is induced at the transducer that is finally detected and processed. (see Figure 1.1)

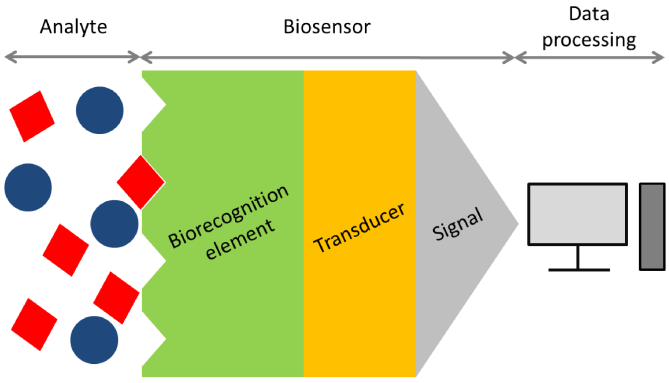

Figure 1.1: General principle of a biosensor. A biorecognition element designed specifically for an analyte is directly connected to a transducer. If an analyte binds to the biorecognition element, the binding event induces a signal at the transducer, which is detected and processed with auxiliary electronics.

Every component can be adjusted to the sensing needs. Today the combination of biology with physicochemical transducers is harnessed to achieve complex bioanalytical measurements with simple setups. There is a strong interest in low-cost biosensors with a fast and real-time detection of the target analyte for routine point-of-care clinical evaluation or real-time diagnosis of diseases. The variety of biological sensing elements and transducers give the opportunity to use biosensors for a wide range of analytical tasks and in versatile application fields from medical diagnostics through drug discovery/design, biomolecular engineering, food industry or environmental control.[2, 5, 6, 7, 8, 9]

1.1 Transducer - surface plasmon polariton

Different kinds of physiochemical transducers were established since the first development. They can be classified in electrochemical, optical, electronic, piezoelectric, gravimetric and pyroelectric biosensors. Further, various signal changes induced by mass, heat, sound, electricity and light can be used for a bioanalytical detection. [5, 6, 7, 8]

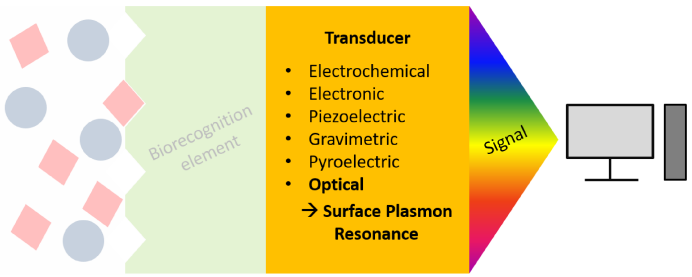

Figure 1.2: Schematic of the biosensor, focusing on the transducer. Transducer with various physical properties can be used, which lead to a detectable signal. The focus is on optical transducer based on Surface Plasmon Resonance.

During the last years especially the development of optical transducers was a fast-paced field because they are resistant to electromagnetic interference and adequate to perform remote sensing. Furthermore, multiplexed detection can be performed within a single device. Optical sensing methods can be classified in label-based methods, e.g. chemiluminescence and fluorescence, and label-free methods, e.g. light absorption and scattering, reflectance and surface plasmon resonance (SPR).

In label-based detection, either target molecules or biorecognition molecules are labeled with tags, e.g. in case of fluorescent-based detection with dyes, which re-emit light upon light excitation. The fluorescence intensity gives information about the presence of the target molecules and the interaction strength between the target and the biorecognition molecules. The main advantage of this detection technique is the high sensitivity with the detection limit down to a single molecule, but the labeling may interfere with the function of a biomolecule. In addition, quantitative analysis is not possible because the number of fluorophores cannot be controlled precisely on each molecule. [10, 11, 12]

In contrast, label-free detection is relatively easy and cheap to perform, because molecules are not labeled or altered, they are detected in their natural forms. Additionally, information about molecule interactions can be gained by quantitative and kinetic measurements. The resulting kinetic data can be used for further analysis of molecular affinity constants, interaction specificity and reaction kinetics. This cannot be measured by endpoint measurement techniques, such as enzyme-linked immunosorbent assay (ELISA). The label-free detection

leads to a continuous, fast, sensitive, selective and real-time detection of the analyte binding to the sensor surface, and the transducer can be reused.[13, 8, 14, 11]

The label-free detection includes several different techniques, e.g. refractive index detection, optical absorption detection and Raman spectroscopic detection. Different kinds of sensors, such as optical interferometers, grating coupler, and SPR are based on changes of refractive index label-free detection. These sensors can detect both the refractive index of the bulk solution (refractometer) and the refractive index change induced by molecule binding (biosensor). [11, 12]

The scope of the thesis will be limited to surface plasmon based biosensors. The main principle is the detection of refractive index changes close to the surface vicinity of metal nanostructures, caused by recognition events or chemical reactions.

1.1.1 Generation of surface plasmon polaritons

In general, plasmonics deals with light-matter interactions, i.e. it describes the interaction between light as external electromagnetic field and metal. For example, in nanophotonics plasmonics is a major topic to describe how electromagnetic fields can be confined on the order of or smaller than the wavelength of visible light. [15]

The plasmons are the quantization of the plasma oscillation, like photons are for light or phonons are for mechanical vibrations. Plasma oscillation is also described as oscillation of free electron density in a metal with respect to the fixed counter ions. To explain the plasma oscillation a short gedankenexperiment: Imagine a cube of metal is placed in an external electric field pointing to the left. Electrons will move to the right side and uncover the positive ions on the left side. They will move until the field inside the metal is canceled. If the external electric field gets negative the electrons move back to the left side because they are attracted to the positive ions on the left side. The so-called plasma frequency describes the movement or so-called momentum of the electrons and has to be fulfilled to induce plasma oscillation. [8]

If the light frequency is below the plasma frequency, the light will be reflected from the metal because the energy will be too low to move the electrons. If the light frequency is higher than the plasma frequency, the light will transmit through the metal surface because the electrons in the metal cannot respond fast enough. Only if the light frequency is the same as the plasma frequency, plasma oscillation is induced.

For the generation of surface plasmons, free electrons at the interface of two materials have to be present. This implies that one material is a metal, where free conduction electrons are abundant. In general, materials which possess a negative real and small positive imaginary

dielectric constant can support surface plasmon resonance. On a metal surface, plasmons are called surface plasmon polaritons and propagate in the x- and y-directions along the metal-dielectric interface. In the z-direction they decay evanescently with $1/e$ decay lengths and have their maximum at the surface, which is typical for surface waves. [11]

The surface plasmon mode depends on the geometry of the plasmonic structure and the environmental parameters. This is the key to use plasmonic structures as biosensors. If the environment is changed by binding of biomolecules to the surface of the metal, a change of the plasmon mode will be induced. There are different methods to detect surface plasmon resonance, which mainly depend on the sensing signal, e.g. spectral, angular and localized. [16]

1.1.2 Surface plasmon resonance detection

The most frequent method for excitation of surface plasmons is by means of a prism coupler and the attenuated total internal reflection (ATR). Two main methods based on ATR are: Kretschmann geometry and Otto geometry. [17] The main focus will be here on the Kretschmann geometry, which will be used as measuring principle in this thesis. The Kretschmann configuration uses a thin metallic layer attached on the back side of a prism with a high refractive index (n_p). An example for a setup is shown in Figure 1.3, where a monochromatic light with a range of incident angles is used.

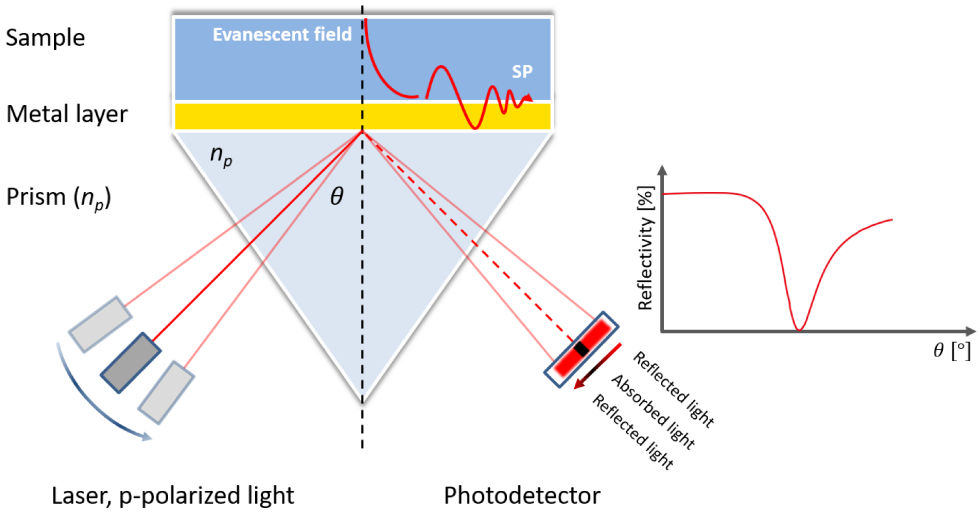

Figure 1.3: SPR setup in Kretschmann configuration with p-polarized light source, a prism with specific refractive index (n_p), a gold layer on top of the prism and a photodetector for signal detection. At a specific incident angle θ of the light, surface plasmon resonance is induced on top of the gold film and a signal drop is detected on the photodetector.

Plasmon excitation occurs at a specific incident angle of the light, which leads to a transfer of energy from the incident light wave into a surface plasmon and the following dissipation in the metal film.[17] If surface plasmons are generated, the reflectivity spectra show dips at the resonant angle. A reduction of power in the reflected light is detected[18]:

$$sin\theta_{sp} = \frac{1}{n_p}\sqrt{\frac{\epsilon_m(\lambda)\epsilon_d}{\epsilon_m(\lambda)+\epsilon_d}} \tag{1.1}$$

where θ_{sp} is the specific angle of incidence, n_p describes the refractive index of the prism, $\epsilon_m(\lambda)$ is a wavelength dependent dielectric constant of the metal film, λ is the excitation wavelength and ϵ_p is the dielectric constant of the dielectric layer.

If the refractive index is changed in vicinity to the gold surface, the incident angle for the plasmon excitation changes and the dip in the reflectivity spectrum shifts. This alteration can be described as change of the effective refractive index (n_{eff}):

$$\Delta n_{eff}(d, n_l, n_b) = \frac{\Delta\theta_{res}}{S_b}[RIU] \tag{1.2}$$

where d is the thickness of the adsorbed layer, n_l and n_b the refractive indices of the layer and the bulk respectively, θ_{res} the plasmon resonance angle and S_b the bulk sensitivity.

1.1.3 Localized surface plasmon resonance

Even though the SPR sensing systems dominate the commercial instrumentation, noble metal nanoparticles and their promising use as plasmonic biosensors were rediscovered in the last decades. Plasmonic nanoparticles are well known for their unique optical properties. By an external incident light beam, density oscillations of the nanoparticle's conduction electrons are induced at specific frequencies, which is known under the term localized surface plasmon resonance (LSPR). This occurring resonance is influenced by changes of the local refractive index of the surrounding medium. This fact gives the opportunity to use noble metal nanoparticles as label-free bioanalytical sensors.

Biomolecules directly bound on the nanoparticle's surface lead to a change of the local refractive index and a shift of the spectrum (see Figure 1.4). The spectral change can be detected by micro-spectroscopy.

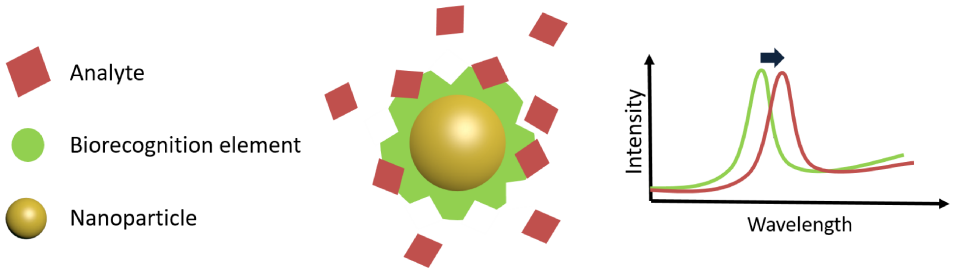

Figure 1.4: Schematic diagram depicting the use of nanoparticles as biosensor. The biorecognition element is directly bound to the nanoparticle's surface. If the target analyte binds to the biorecognition element, the local refractive index of the nanoparticle changes and the detected signal shifts.

Already in the 1980s and 1990s noble metal nanoparticles in solutions were used as biosensors and immunoassays. Examples are colorimetric assays based on the large optical cross sections of noble metal nanoparticles or aggregations assays based on color changes after clustering of the nanoparticles. The first label-free refractometric LSPR sensing was reported by Mirkin et al. [19] and Alivisatos et al. [20], showing that molecular adsorption on gold nanoparticles leads to a color shift of the colloidal solution.

During the last decade, LSPR sensing on nanoparticles immobilized on a substrate came into focus. This composition allows to combine LSPR sensing with microfluidics and to build compact and even portable instruments at low costs. [8] Further, the LSPR sensing can be optimized to the application because the LSPR depends strongly on material, size and shape of the nanoparticles. In general, five strategies can be differentiated to apply metal nanoparticles and their LSPR-based sensing properties [21]:

1. use nanoparticles as labels and detect their LSPR absorbance/scattering ($\Delta C_{abs/sca}$)
2. induce metal nanoparticle aggregation by analyte binding and detect the subsequent LSPR wavelength shift ($\Delta C_{abs/sca}$)
3. detect analyte induced distance changes (Δd) in linked metal nanoparticles (so-called plasmonic rulers)
4. detect LSPR wavelength shift induced by bulk refractive index changes of the surrounding medium (Δn_b)
5. detect LSPR wavelength shift induced by analyte binding on the nanoparticle surface (Δn_s)

LSPR theory

If light interacts with particles much smaller than the incident wavelength, so-called nanoparticles, the particle's free electrons are responsible for the collective oscillation and it is termed localized surface plasmon resonance (LSPR). The plasmon oscillates locally around the nanoparticles, therefore "localized" surface plasmon resonance, with a specific frequency. (Figure 1.5) Comparable to the SPR, the electric field close to the nanoparticle's surface is enhanced and decays exponentially. [22]

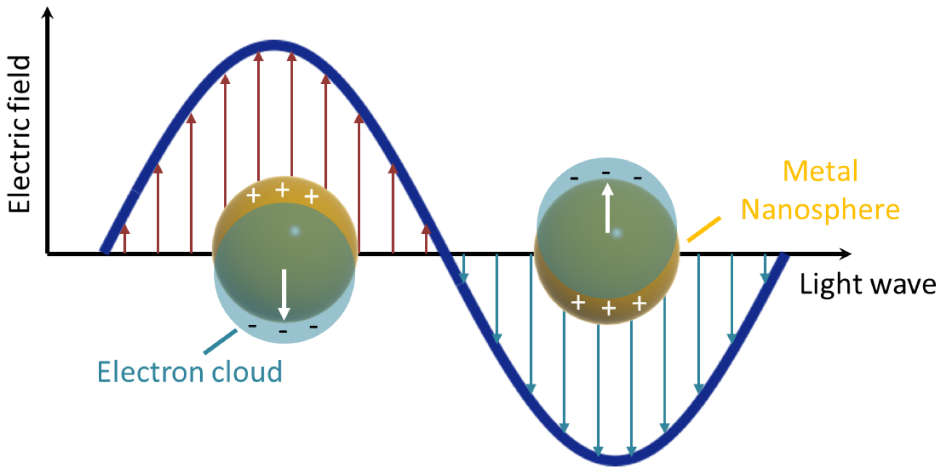

Figure 1.5: Schematic diagram illustrating the interaction between the electric field of incident light and free electrons of a metal nanosphere. The electric field causes a shift of the free electrons in one direction. A dipole is induced at the metal nanosphere, which alters according to the electric field. If the frequency of the dipole plasmon is nearly the same as the incident light, the localized surface plasmon resonance condition is reached. [23]

Michael Faraday (1791-1867) and Gustav Mie (1868-1957) started to understand the physics of nanoparticle plasmons. Already 1908 Gustav Mie published an analytical solution to Maxwell's equations, describing the interaction of light with spherical particles. [24] He explained the response of an uncharged spherical particle to an electromagnetic field in a homogenous medium. Mie was the first who applied this to the problem of light scattering of metal spheres. The scattering, absorption and extinction of nanoparticles is described by wavelength dependent cross-sections. If a cuvette of the thickness d is filled with a particle solution with the number density n, an intensity loss ΔI of an incident parallel beam passing the cuvette is given by [25]:

$$\Delta I = I_0(1 - e^{-n(C_{abs}+C_{sca})d}) = I_0(1 - e^{-nC_{ext}d}) \tag{1.3}$$

The resulting total scattering, absorption and extinction cross-sections are described as following [26]:

$$C_{sca} = \frac{2\pi}{|k|^2}\sum_{n=1}^{\infty}(2n+1)(|a_n|^2 + |b_n|^2) \tag{1.4}$$

$$C_{ext} = \frac{2\pi}{|k|^2}\sum_{n=1}^{\infty}(2n+1)[Re(a_n + b_n)] \tag{1.5}$$

$$C_{abs} = C_{ext} - C_{sca} \tag{1.6}$$

where k describes the incoming wavevector and n are integers that represent dipole, quadrupole and higher multipoles of the scattering, which depend on the shape of the nanoparticle (see anisotropic nanoparticles 1.1.3). The terms a_n and b_n are composed of Riccati-Bessel functions ψ_n and χ_n:

$$a_n = \frac{m\psi_n(mx)\psi_n'(x) - \psi_n'(mx)\psi_n(x)}{m\psi_n(mx)\chi_n'(x) - \psi_n'(mx)\chi_n(x)} \tag{1.7}$$

$$b_n = \frac{\psi_n(mx)\psi_n'(x) - m\psi_n'(mx)\psi_n(x)}{\psi_n(mx)\chi_n'(x) - m\psi_n'(mx)\chi_n(x)} \tag{1.8}$$

In the equations $m = \tilde{n}/n_m$ and gives the relation between the complex refractive index of the metal ($\tilde{n} = n_{Re} + in_{Im}$) and the real refractive index of the surrounding medium (n_m). x stands for $x = k_m r$, where $k_m = 2\pi/\lambda_m$ is the wavenumber in the medium, and r is the radius of the particle. [22] The equation shows that the propagating field of the nanoparticle can be

tuned by the size of the nanoparticle because the size influences the relative magnitude of the scattering and absorption cross-section. The absorption cross-section mainly dominates at nanoparticles smaller than 20 nm. If the size of the nanoparticle is increased, the scattering cross-section of the nanoparticles is increased, too. This ratio of scattering to absorption is only influenced by the size of the nanoparticle, not by its aspect ratio. [27]

Both equations 1.7 and 1.8 have the real refractive index of the surrounding medium included. Therefore, a change of the surrounding medium has direct influence on the extinction (and scattering) of the particle. This is the reason why nanoparticles can be used as transducers. Changes in the surrounding, e.g. adsorption of biomolecules, cause a change in the LSPR extinction (or scattering) wavelength maximum λ_{max}:

$$\Delta\lambda_{max} = m\Delta n \left[1 - exp\left(\frac{-2d}{l_d}\right)\right] \tag{1.9}$$

Here m stands for the bulk refractive index response of the nanoparticles, Δn describes the refractive index change, d is the thickness of the adsorbate layer and l_d is the characteristic penetration depth of the nanoparticles' electromagnetic field.[28]

Anisotropic nanoparticles

As described by the equation 1.4 and following, the shape and the size of the nanoparticles contribute strongly to the spectral properties. Various shapes, such as spheres, triangles, cubes, prisms, nanorods, nanostars, etc. have been already prepared to tune the LSPR band from visible to infrared region. During , two main factors can be influenced:

- increase of edges and sharpness, which leads to a red shift of extinction spectra due to an increase in charge separation
- increase of the particle symmetry, which increases the LSPR intensity

The number of peaks in the LSPR spectrum depends on the number of modes in which a nanoparticle can be polarized. Especially anisotropic nanoparticles are sensitive to polarizations of the incident light. [29] For example, oblonged nanoparticles, e.g. nanorods or nanopeanuts, show two resonance states in longitudinal and transverse direction. If the incident light is polarized parallel to the main axis of the nanoparticle, the spectral maximum comes from the longitudinal resonance. On the other hand, if the light is polarized perpendicularly to the main axis, the spectrum gives information about the transverse resonance. [30]

The sensitivity of nanoparticles depends also on geometric parameters. For example, a size change from 10 to 100 nm of spherical gold nanoparticles causes a red shift of 47 nm, and a change of aspect ratio from 2.5 to 3.5 for an elliptical nanoparticle leads to a longitudinal band change of 92 nm. [31] The shape of the nanoparticle influences the refractive index sensitivity as well. McFarland et al. [32] showed that the highest sensitivities were reached with silver nanorods, followed by silver triangles and silver spheres. Nanostructures with high aspect ratios or sharp edges usually result in LSPR spectra showing several modes and a high sensitivity to refractive index changes in the surrounding medium.

1.2 Biorecognition element - DNA

A biosensor is a detection and analysis tool incorporating a biological sensing element or so-called biorecognition element. The choice of the biorecognition element depends on the target analyte of interest and is crucial to guarantee specific binding. A variety of recognition elements can be used, such as antibodies, antigens, nucleic acids, lipid membranes, viruses, cells enzymes, etc. [33, 34, 35]

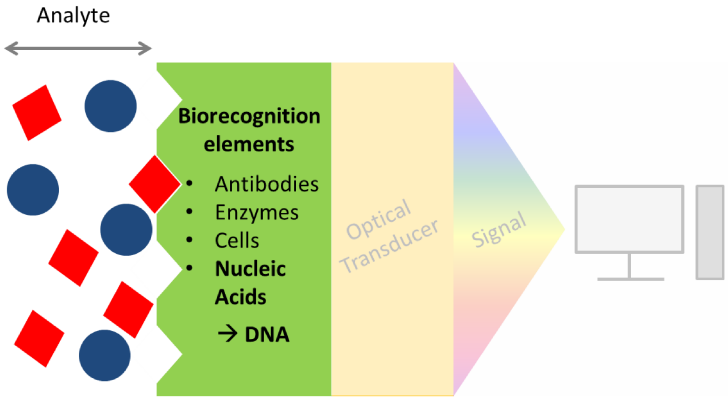

Figure 1.6: Schematic of the biosensor, focusing on the biorecognition element. According to the target analyte various biorecognition elements can be used. The focus is on nucleic acids, especially DNA as biorecognition element.

According to the nature of biorecognition events two types of biosensors can be differentiated [36]:

1. Bioaffinity sensors: the target analyte binds to a surface-confined ligand partner (e.g. antibody, nucleic acid)

2. Biocatalytic sensors: an immobilized enzyme is used for recognizing the target, e.g. biosensors with immobilized glucose oxidase are used for diabetes monitoring

During the last two decades the interest in bioaffinity sensors based on nucleic acids increased. In 1953, Watson and Crick published the discovery of the double helical structure of deoxyribonucleic acid (DNA) [37], which is the base for hybridization-based affinity detection. After the invention of DNA chemical synthesis it was possible to reproduce single-stranded DNA (ssDNA) with designed sequences. [38] The key property for bioanalytical analysis is the specific hybridization of nucleic acids to complementary sequences. Several methods were established based on DNA hybridization for example southern blotting or nucleic acid amplifications, e.g. polymerase chain reaction (PCR). The starting point for a revolution

in genetic analysis was the sequencing of the human genome. A new goal in molecular biology arose: rapid extraction and analysis of genetic information, which can be used for DNA sequencing, gene mapping, clinical diagnosis of inherited diseases and rapid detection of infectious microorganisms. [1, 39, 40, 41, 13]

The first DNA biosensor was mentioned in 1988 by Fawcett et al. [42]. The DNA was detected with a piezoelectric transducer. Additionally DNA biosensors with electrochemical and optical (especially SPR) transducers were broadly studied in the 1990s. During the last two decades a great effort has been devoted to improve the selectivity and sensitivity of DNA biosensors and miniaturization to decrease the sample volumes. Today the DNA detection is of great interest in many fields: DNA diagnostics, drug development, gene analysis, fast detection of biological warfare agents and forensic applications. [1]

The DNA biosensor takes advantage of the binding of complementary ssDNA sequences. The probe or capture DNA is immobilized onto the transducer surface to recognize its complementary target DNA by hybridization and the transduction for a successful hybridization is measured depending on the transducer. [13]

Hybridization can be performed in two ways: target DNA hybridizes to a surface-tethered capture DNA (solid-phase hybridization) or the hybridization occurs between the target DNA and randomly distributed capture DNA in solution (solution-phase hybridization) [43]. These hybridization schemes show different behaviors. The focus in this work is on the solid-phase hybridization; the capture DNA is bound to a surface and the target DNA hybridizes to it. Solid-phase hybridization give the opportunity to wash off non-specific bonding sequences, and only strongly paired strands will remain hybridized.

1.2.1 DNA detection on gold surfaces

The SPR sensor chip producer Xantec states on its website: "The quality of the data obtained with a SPR system depends mainly on the sensor chip surface." [44] Hence, the chip surface has to be additionally prepared and adjusted to the experimental needs. The company BIAcore for example, which successfully established the SPR system, had one of the strongest patent protections in the immobilization chemistry of the DNA to gold. To immobilize the desired ligands, a carboxy-methylated dextran matrix is adsorbed to the gold surface by carboxyl groups and activated by ethyl(dimethylaminopropyl) carbodiimide (EDC) and N-hydroxysuccinimide (NHS). This technique increases the receptor loading capacity exponentially on the gold surface and is standard today. [5]

The penetration depths for gold surfaces are more than 200 nm. Hence, an additional dextran matrix layer of minimum 100 nm does not have a significant influence on the SPR

signal.[45] In contrast, a 100 nm dextran layer on nanoparticles exceeds their penetration depths and no biomolecule could be detected anymore. The confined field of the nanoparticles is only sensitive to changes in the close vicinity. Therefore, the ssDNA has to be immobilized directly on the nanoparticles surface to achieve the highest sensitivity. The immobilization can be performed as direct adsorption or covalent adsorption to the transducers' surface. The subsequent hybridization efficiency is strongly influenced by the surface capture DNA density, conformation of capture DNA strands and curvature of the solid surface.

Covalent adsorption

The most common covalent immobilization form are self-assembled monolayers (SAMs). Organic assemblies are formed by chemical adsorption (i.e. chemisorption) of molecular components from solution or gas phase onto the surface of solids. The molecules or ligands that form SAMs organize spontaneously into crystalline (or semicrystalline) structures. They consist of a chemical functionality ("headgroup"), with a specific affinity for a substrate. The most common example are N-alkylthiols or disulfides, which consist of an alkyl backbone chain, thiol head and functional tail groups. The thiol head group has a strong affinity to bind to metal surfaces (e.g. silver and gold) and the other functional end consists of biomolecules, the capture DNA strand, respectively. [46, 47, 48, 13]

The self-assembly process on gold is not yet fully elucidated. It is reported that the adsorption of thiols follow two or three kinetic steps. For example, Peterlinz and Georgiadis claimed that the process consists of a rapid first step and a slow third step following Langmuir adsorption kinetics and the second step is independent from the concentration (zeroth order). [49] Dilimon et al. [50] investigated the adsorption of n-tetradecanethiol (RSH) by electrochemical analysis. The results showed that after 3 minutes of fast adsorption an intermediate stage was reached, this condition continues for 5 minutes and is followed by a slow final adsorption. The intermediate region was less pronounced in solutions with higher concentrations ($> 2\,\mu M$). The intermediate state may come from the change from physisorption to chemical binding of the molecules to the surface. [51]

$$R - SH + Au \rightarrow R - S - Au + e^{-} + H^{+} \tag{1.10}$$

The arrangement of the SAM with DNA plays an important role for a high hybridization efficiency. [38] Two main points have to be considered: capture DNA accessibility and affinity of target DNA to capture DNA adsorbed on the sensor surface. A higher accessibility leads to a higher hybridization efficiency and finally to stronger signals. It depends on the conformation of the surface and ssDNA coverage density.[52]

Direct adsorption

The direct adsorption implies the immobilization of DNA on a transducer surface without nucleic acid modification. The backbone phosphate (pK_a value = 2) of a chemically synthesized DNA contains n - 1 (n = number of bases) negative charges and the bases are non-charged within a pH range from 5 to 8, therefore DNA is negatively charged at neutral pH. [38] The DNA can be directly adsorbed on a positively charged surface. In case of gold nanoparticles the surface is negatively charged, an additional positively charged layer would be needed to immobilize the DNA on the surface. Further, the DNA would adsorb flatly on the transducer surface and less binding sites would be available for the target DNA.

Recent publications [53, 54, 55, 56] showed that these disadvantages of direct DNA adsorption on gold can be circumvented by considering affinity interactions between the DNA bases and the gold surface. Spectroscopic studies have shown that a strong chemical bonding exists between DNA bases and a gold surface. Kimura-Suda et al. [53] studied the competitive adsorption between all possible pairs of unmodified oligomers to polycrystalline gold films. They showed that homo-oligonucleotides adsorb on gold with relative affinity A > C $\geq$ G > T. [53] According to Jang the strong adsorption of deoxyadenosine is caused by the N6 exocyclic amino and the N7 atom. [57] Deoxyguanosine is binding via the C=O group together with N1 nitrogen. Jang suggested that deoxycytidine binds via the N3 nitrogen as well as the keto oxygen, but corresponding to Doneux and Fojt the chemisorption occurs just via the N3 nitrogen. [58] The weakest adsorption was expressed by thymine via the C4 keto oxygen. [57]

Adenine has the highest affinity to gold; that is why it was claimed to use a poly(A) tail for the adsorption of the capture DNA to the gold surface. Pei et al. [56] showed that this method allows to define the distance between the capture sequence. The prolongation of the poly(A) tail leads to an increased distance between the DNA strands. They even showed that a faster adsorption of the DNA to the nanoparticle in solution was possible with a citrate buffer at pH = 3.0.

Curvature effects

The particle curvature, which is related to the particle diameter, plays a crucial role in controlling the DNA surface density. The highest packing density is close to the nanoparticle and the disorder increases with increased distance from the particle surface. The volume per molecule "[...]increases for spherical particles as the square of the radius with distance from the particle center (in the shape of a truncated cone) but does not change with distance from a plane." [59] On planar gold surfaces Steel et al. [60] reported maximum coverages for ssDNA on the order of ~ 5×10^{12} molecules/cm^2 ($2\,nm^2$/molecule). If the curvature of the

surface increases, it is possible to adsorb more ssDNA strands. Hill et al. [61] compared adsorption of 25-nucleotide DNA strands on nanospheres with a diameter from 10 to 200 nm. The occupied molecular area varied from $5\,nm^2$ ($2.0\,\mathrm{x}\,10^{13}/cm^2$) for the smallest to $15\,nm^2$ ($6.8\,\mathrm{x}\,10^{12}/cm^2$) for the largest particles. The smaller the nanoparticle, the higher the number of adsorbed ssDNA strands.

Effect of pH

The pH of the surrounding medium affects the DNA adsorption to the transducer and the DNA conformation. Gold nanoparticles are usually prepared by a citrate reduction method and are stabilized by weakly adsorbed citrate ions. In total the nanoparticles are negatively charged. DNA is also highly negatively charged, which leads to a repulsion between the DNA strands and the gold nanoparticles. Therefore, pH plays an important role in DNA adsorption onto gold. The pH value of the surrounding buffer plays a role in the conformation of the adsorbed ssDNA. At a pH greater than 9 deprotonation occurs for the bases thymine and guanine and at pH below 4 protonation occurs for cytosine and adenine. DNA is thereby a zwitterionic polymer. [38, 52]

Effect of coadsorption

Herne and Tarlov [62] pointed out that a low hybridization efficiency results from high surface coverage of ssDNA. The steric hindrance prevents the hybridization of the target DNA. At low surface coverages, probes can adsorb in different orientations on the surface, which again leads to a low hybridization efficiency. An increase of the ssDNA availability can be achieved by adding thiol compounds as chemical blocking agents. The length and terminal group of these compounds have a crucial effect on the sensitivity and detection limit. It was shown that with the alkanethiol mercaptohexanol (MCH) the conformation of covalently linked ssDNA on gold nanoparticles can be controlled. The addition of MCH leads to a destabilization of the DNA bases adsorbed on the gold surface. This effect improves the hybridization efficiency because the hybridization accessibility is increased by erection of the specific tethered ssDNA from the gold surface. The coadsorption of MCH has furthermore two advantages: MCH is a short alkanethiol with a hydrophilic end-group. The additional adsorption of MCH reduces steric crowding and electrostatic repulsion between the ssDNA strands and it passivates the surface and prevents thereby the nonspecific adsorption of ssDNA. To achieve the desired effects, the MCH concentration and reaction time are crucial factors. [62, 63, 52, 64]

Effect of temperature

DNA can be denaturated by heating over the melting temperature T_m. Heating destroys the hydrogen bonds between the nucleic acid strands and the base pairs. T_m depends on the conformation of the ssDNA (base order) and the saltinity of the solution. For adenine/thymine base pairing a lower temperature is needed to break up the bonding compared to the guanine/cytosine base pair. This comes from the different number of hydrogen bindings between the bases. Adenine/thymine base pair has a decreased binding stability compared to the guanine/cytosine base pair. For comparison: if a short nucleic acid sequence is extended by an adenine/thymine base pair T_m is increased for 2 K and if a guanine/cytosine base pair is added it increases for about 4 K. The hybridization temperature can be calculated from the melting temperature. The longer the DNA strand, the lower is the difference from the melting temperature to the hybridization temperature. [65] A high hybridization temperature increases the binding specificity because the increased movement of the DNA caused by the heating hinders the hydrogen bonding. At temperatures close to the melting temperature perfect paired molecules are binding to each other and mismatches lead to destabilization and separation of the double strand. At low temperature the chance of unspecific binding is increased. [65]

1.2.2 Regeneration of DNA biosensor

One main advantage of the DNA based biosensor is the regeneration of the surface-immobilized probe. The capture DNA can be reused without loss of hybridization efficiency. The regeneration can be induced thermally or chemically. For thermal regeneration the DNA has to be heated up to 90°C, which is hard to realize in a microfluidic chip due to bubble formation. In terms of chemical regeneration several possibilities were reported. The DNA can be exposed to a 10 mM sodium hydroxide (NaOH) solution for 1 min [66], to a 50 mM NaOH/0.1% sodium dodecyl sulfate (SDS) solution [67] or to 1 or 10 mM hydrogen chloride (HCl). [68, 69] Denaturation due to chemical agents has two advantages: It can be executed faster than thermal denaturation and at room temperature.

1.2.3 DNAzymes

DNA is a dynamic molecule, which can form a number of spatial arrangements, such as single-stranded hairpins, homoduplexes, triplexes and quadruplexes. A well-studied structure is the guanine quadruplex (G-quadruplex) formed by guanine quartets. As mentioned before, the usual base pairing occurs between adenine and thymine or guanine and cytosine. However, G-quartets show a variation of base pairing, the so-called Hoogsteen base pairing. The

guanine base is linked with neighboring guanine via two hydrogen bonds, as shown in Figure 1.7. These G-quartets stack on each other and form a G-quadruplex structure, if alkali metal ions are present in the center between two G-quartets. Mostly potassium or sodium cations are connected by electrostatic interactions on the guanine carbonyl. [70, 71] G-quadruplexes can be formed by one, two or four separate DNA strands. Depending on the sequence, various topologies can be created with various possible combinations of strand directions. [72]

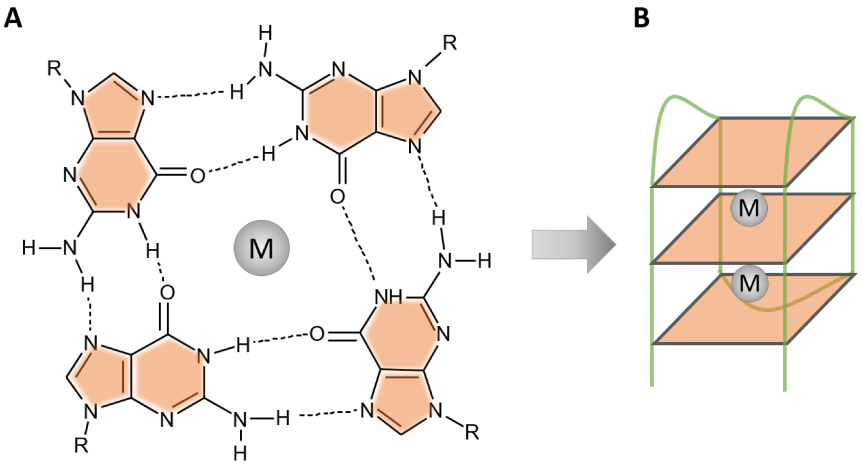

Figure 1.7: A - Chemical structure of G-quartet with metal ion in the center. The guanine bases are connected by two hydrogen bonds. B - Schematic of a G-quadruplex formed by one DNA strand (depicted in green) as example. The guanine bases form the G-quartets and are stacked above each other. Inbetween cations stabilize the G-quadruplex.

This kind of 3D DNA structure can form a complex with hemin and are called deoxyribozymes or DNAzymes due to their peroxidase-like activity. In the late 1990s Sen and co-workers [73, 74] reported that hemin could catalyze peroxidase reaction with and without enzymes to some extent. They further searched for an artificial system to increase the catalytic activity of hemin and reported that a quadruplex-forming sequence could enhance the peroxidase activity of hemin. They created a 24- and 18-nucleotide aptamer, which binds hemin and increases the peroxidase performance. Aptamers are 3D DNA structures that can selectively bind target molecules, here the iron-containing porphyrin. All DNAzymes are artificially obtained by in vitro selection (Systematic Evolution of Ligands by EXponential Enrichment, SELEX) and not present in vivo. The main advantage of DNAzymes is their thermal stability. In contrast to enzymes, DNAzymes are less susceptible to temperature variations and some sequences are stable up to 90°C. DNAzymes with peroxidase-mimicking activity have great potential in various fields. Applications include the detection of specific

DNA sequences in bioassays, detection of metal cations such as Ag^{+}, Cu^{2+}, Pb^{2+}, Hg^{2+} and Sr^{2+}, amplified detection of small molecules like cocaine or adenosine or proteins such as thrombin or lysozyme. [75, 76, 77, 70] The catalytic activity of DNAzymes can be observed by indicator reaction. In biological applications two substrates are usually used: ABTS (2,2'-azino-bis(3-ethylbenzthiazoline-6-sulphonic acid)) and luminol. ABTS in combination with H_2O_2 produces a colored product and leads to a change in the absorption spectrum. Luminol reacts with hydrogen peroxide and generates chemiluminiscence with altered intensity.

1.3 Aim & objectives

Noble metal nanoparticles with their distinct optical properties have a great potential for label-free bioanalytical sensing. Former results showed that biomolecules can be detected on immobilized nanoparticles but there is no evidence for a real-time detection. A label-free online detection of biomolecules with immobilized nanoparticles in a microfluidic chamber want to be realized.

To accomplish this goal, two sensing systems with nanoparticles will be combined with a microfluidic system. For verification, results will be compared to the commercially available SPR system. Figure 1.8 gives an overview of the investigated systems with their nomenclature. Surface plasmons are induced at a flat gold layer (SPR), in noble metal nanoparticles adsorbed densely on a glass surface (LSPR) or in single nanoparticles adsorbed on a glass surface (sLSPR). The detected signal differs between the SPR and LSPR/sLSPR system due to the different setups. The signal change induced by a change of the dielectric environment will be visualized in a sensogram.

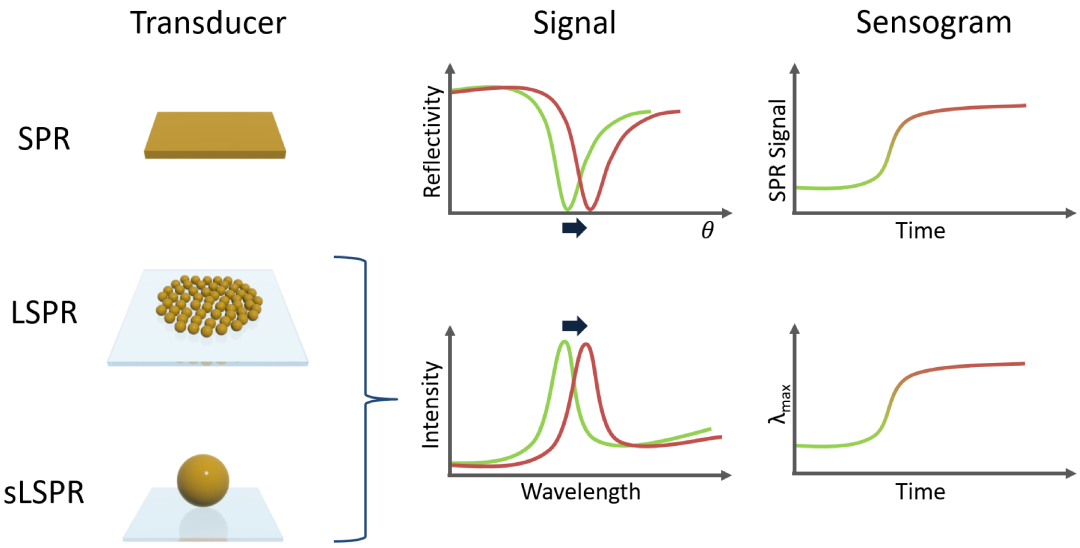

Figure 1.8: Overview of the investigated setups with their plasmonic transducer, the detected signal and the resultant sensogram.

For the LSPR and sLSPR system, microfluidic chambers will be designed and connected to a microfluidic system for a direct injection of the explored solutions. The design has to ensure the detection of the LSPR signal without significant losses, high stability, no leakages and no bubble formation. To achieve real-time measurements on single nanoparticle level (sLSPR) the microfluidic chamber and holder has to fit precisely into a microscope in transmission

geometry.

As already mentioned nanoparticles can be produced with a variety of materials, sizes and shapes. Here, spherical gold nanoparticles with the sizes 30 nm, 60 nm and 80 nm, gold nanopeanuts and silver nanoprisms with gold edges will be tested as potential transducers with the LSPR system. A protocol will be established to adsorb the nanoparticles on a glass slide with a high density to gain distinct spectra with high signal-to-noise ratio.

The new sensing systems with the different transducers will be initially evaluated by bulk refractive index measurements. The refractive index in the whole medium surrounding the nanoparticles will be changed and detected in real-time. This gives information about their applicability as transducers and their bulk refractive index sensitivities.

Next to the bulk sensitivity, the surface refractive index sensitivity has to be determined because biomolecules will bind directly on the nanoparticle surface. Nanometer thin polyelectrolyte layers with opposite charges will be adsorbed alternately on the nanoparticles with wash steps in between. This layer-by-layer (LbL) deposition mimics the adsorption of biomolecules to the nanoparticle surface. The measurements will demonstrate if the two sensing systems can be used for biomolecule detection and if the studied transducers are applicable for biosensing with the applied setups.

Additionally, the results for bulk sensitivity will be compared with the results of the SPR system. The resulting data of SPR and LSPR/sLSPR are not directly comparable, as shown in Figure 1.8. Hence, for verification the data will be converted to attain a direct comparison of the different systems. The identification of the surface sensitivities will disclose the potential of immobilized nanoparticles as biosensors.

Afterwards the LbL technique will be executed again, but polyelectrolytes will be exchanged to biomolecules. Protein multilayers will be adsorbed on the transducers. This similar measurement procedure will verify if biomolecules can be detected with the applied systems.

After adaptability tests, DNA-DNA interaction will be investigated on noble metal nanoparticles. In Figure 1.9, the achievable DNA biosensor is depicted with the different components and the sensing principle. The desired target analyte is DNA, therefore the biorecognition element is the capture DNA. The binding event will be transformed by the plasmonic nanoparticle into a change of color, respectively a spectral shift. This change of signal will be analyzed and represented in a sensogram.

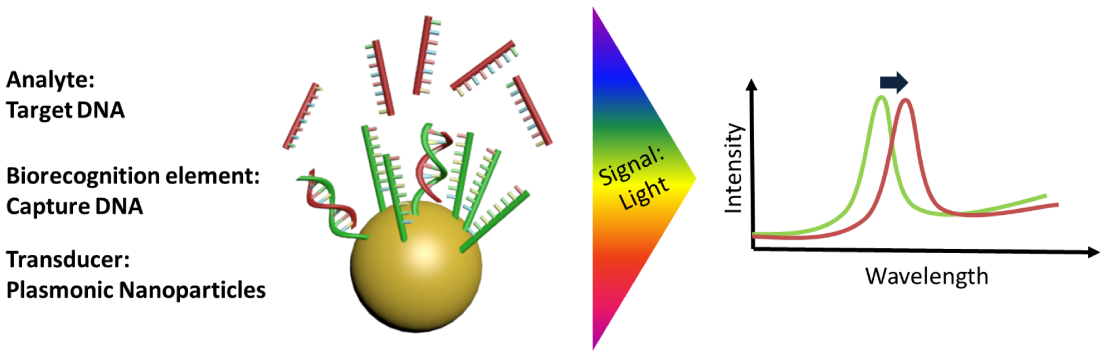

Figure 1.9: Summary of the desired biosensor components and sensing principle of this thesis.

The biofunctionalization of the nanoparticles with capture DNA will be initially investigated to ascertain if ssDNA is detectable in a microfluidic chamber in real-time. The capture DNA will be adsorbed covalently or directly to the nanoparticles. Measurements will be executed with several DNA sequences with different spacer lengths. The subsequent hybridization of the target DNA reveals if the capture DNA is accessible for the hybridization and binds specifically. Short alkanol-thiol molecules will be adsorbed additionally after biofunctionalization to explore if the hybridization effeciency can be increased. In order to reuse the transducer, the target DNA has to be removed. Investigations will be carried out to realize this regeneration procedure.

Preliminary tests will be conducted to detect the biomolecule hemin. ssDNA with a specific sequence forming a G-quadruplex will be covalently bound to the nanoparticle surface. The binding of heme to the G-quadruplex structure will be studied. A successful binding leads to a so-called DNAzyme with peroxidase activity.

2 Materials and methods

2.1 Preparation and characterization of nanostructures

For immobilization of the different nanoparticles, 15 x 15 mm glass slides (VWR International, Germany) were cleaned with rinsing agent by hand, and additionally with acetone, ethanol and water in ultrasonic bath (Bandelin Sonorex, Germany) for 10 min each. In addition, the glass slides were cleaned by oxygen plasma etching for 1 h at 380 W (Tepla, Germany). For a higher affinity of the nanoparticles to the surface the glass slides were silanized with alkoxysilane molecules (Figure 2.1). Therefore, 1 % of 3 - aminopropyltriethoxysilane (APTES) in 1 mM acetic acid was prepared and stirred for 5 min to reach a full hydrolysation. Subsequently, the glass slides were incubated with the prepared solution for 10 min and washed with water in ultrasonic bath for 3 min.

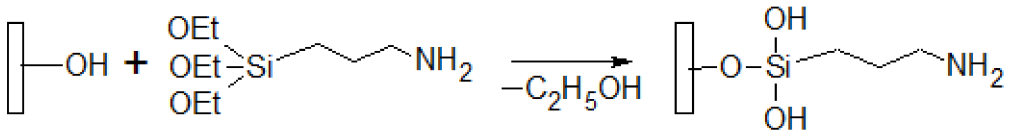

Figure 2.1: Chemical reaction of activated substrate with APTES.

For a high nanoparticle density on the LSPR glass slide the spherical gold nanoparticles solution with a diameter of 30, 60 and 80 nm from British BioCell International (UK) were centrifuged (Centrifuge Herolab UniCen 15DR, Rotor Sigma 12024-H). Depending on size the approach differed: 30 nm: 8000 rpm, 6 min; 60 nm: 6000 rpm, 6 min; 80 nm: 6000 rpm, 8 min; The total volume was 2 ml, where 1.8 ml supernatant were removed and 200μl were used as solution for the nanoparticle immobilization. 20 μl of the concentrated solution were pipetted in the middle of glass slides. After an incubation time of 1 h the glass slides were rinsed with 3dH_2O and dried under nitrogen. The silver nanopsrisms with gold edges were synthesized by Matthias Thiele. Glass slides were incubated with 20 μl of the nanoprism solution for 2 h 15 min. 5 μl of the solution were added after 1 h 15 min due to evaporation. The nanopeanuts were synthesized and immobilized by Frank Theil.

In case of the glass slides for the sLSPR measurements the density of the nanoparticles on the glass slide was adjusted by dilution of the nanoparticle solution. The stock solution of 80 nm gold nanoparticles was diluted 1:10 with 3dH_2O. The whole glass slides were incubated with 200 μl of the nanoparticles solution. Again after 1 h, the glass slides were rinsed with 3dH_2O and dried under nitrogen.

Characterization of investigated transducers

The structural characterization of the used nanoparticles was carried out by atomic force microscopy (AFM) and transmission electron microscopy (TEM). The topology of the adsorbed nanoparticles was measured by atomic force microscope Dimension TM 3100 (Digital Instruments, Veeco, USA) in tapping mode with tapping probes (Tap300-G, Budgetsensors). Further analysis of the data was realized with Gwyddion 2.31. The TEM measurements were conducted with a JEM 1400 (JEOL) with an accelerating voltage of 80 kV and the connected camera Orius 1000 (GATAN). For the measurements the nanoparticles were dried on a TEM-grid.

2.2 Preparation of microfluidic setup

To provide online detection of different analyte solutions a microfluidic setup was implemented that consisted of three parts (Figure 2.2): a syringe pump, an injection valve and a microfluidic chamber. For a continuous flow a two-syringe infusion/withdrawal pump (kd-Scientific USA model 210, ser. No.4037) was used with flow rates between $20\mu l/min$ and $500\mu l/min$ depending on application. The pump was connected by PTFE tubes with an inner diameter of 0.5 mm to an automated switching valve device (Rheodyne Automated Switching Valves model EV750-201, serial number 8594; 10 position selector) for a better and faster change of the solutions. The loop with the target solution had a capacity of $100\mu l$.

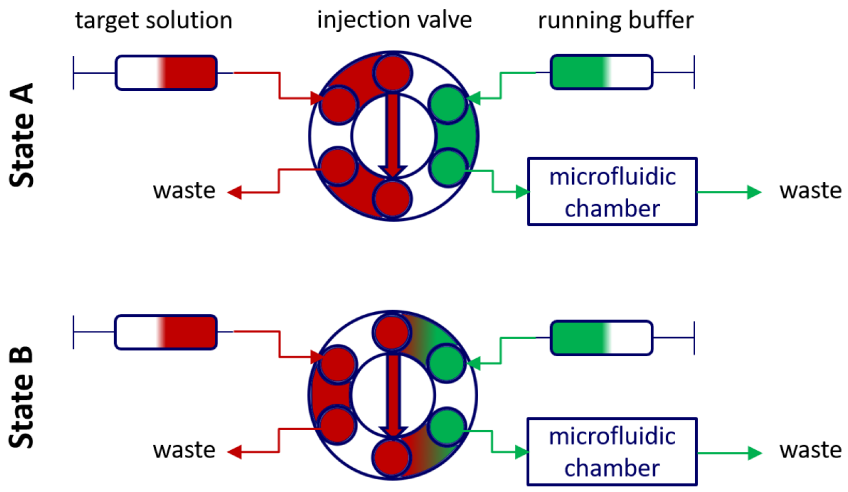

Figure 2.2: Fluid management setup for LSPR and sLSPR measurements. The running buffer and target solution are directed to the microfluidic chamber via an switching injection valve with several inlets/outlets. In State A the running buffer flows directly to the microfluidic chamber and the target solution can be infused in a loop (red arrow in the middle of the injection valve). After the switch to State B, the target solution in the loop is connected to the syringe of the running buffer and directly infused into the microfluidic chamber.

The microfluidic chamber was custom-designed and assembled by a 35 x 16 mm glass slide with drilled holes, pressure sensitive adhesive (PSA) layers (Adhesives Research, ARcare 92712) overhead transparency (Inkjet 2502 Avery) and the glass slide with the immobilized nanoparticles (see Figure 2.3. The design was sketched with CorelDraw and the different layers were cut out with a cutting plotter (Graphtec Cutting Master 2). The created chamber had a height around 200 μm and the volume for the LSPR measurements was around 3 μl and for the sLSPR measurements 7.5 μl.

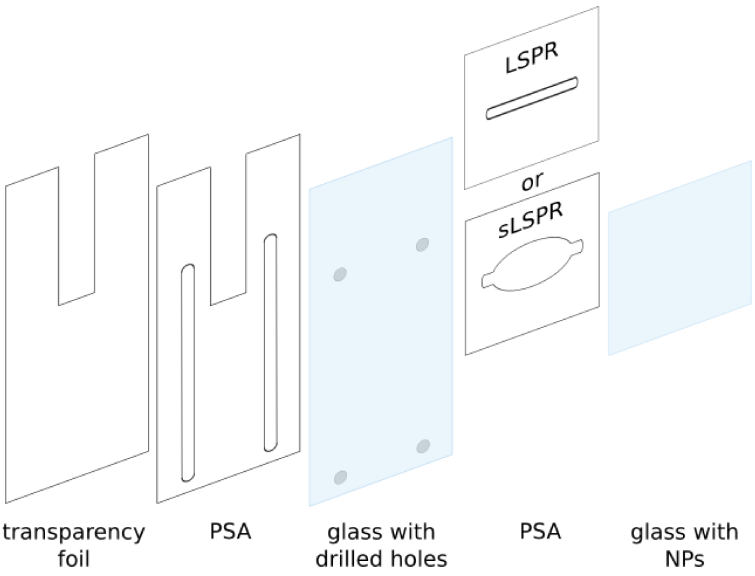

Figure 2.3: The microfluidic chamber is composed of glued layers. The individual layers are made from different materials: transparency foil, pressure sensitive adhesive (PSA) and glass. For LSPR and sLSPR two sizes of chambers were created.

2.3 Experimental setups for surface plasmon detection

2.3.1 Setup for SPR detection

SPR measurements were realized with a dual channel SPR Instrument Reichert SR7000DC connected to a syringe pump (Reichert SR 7500) via an injection valve with a probe loop with a volume of 250 μl or 500 μl (Figure 2.4). Peek tubes were used with 0.010¨ inner diameter. 12.5 x 12.5 mm gold coated glass slides consisting of a 0.33 mm glass slide, a 10 Å chromium layer and a 500 Å gold layer were purchased from XanTec bioanalytics GmbH, Germany and used as sensor substrate. The wavelength of the illumination light was 780 nm. Before implementation of the SPR chips into the device, they were cleaned by oxygen plasma etching for 10 sec at 380 W. For a decreased refraction between the interfaces of the glass prism and the substrate a drop of immersion oil was applied. For the microfluidic chamber a gasket with two channels was mounted between the gold chip and the tube connector. The arrangement of the connected tubes to the microfluidic chamber was alterable. Solutions were infused into one channel after the other or one channel was enclosed and used as reference channel. The SPR device was operated by SPRV4 program. The data was subsequently processed by Matlab software.

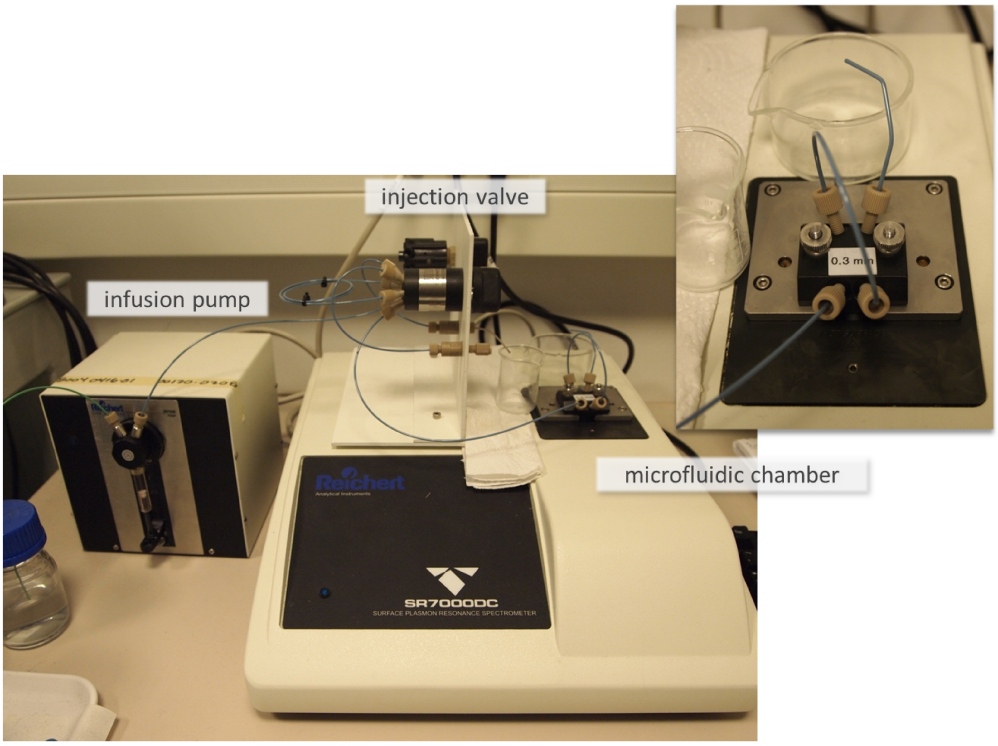

Figure 2.4: Setup of SPR system with infusion pump, injection valve and microfluidic chamber with gold film.

2.3.2 Setup for LSPR detection

The LSPR measuring setup included a halogen light source (HL-2000-FHSA from Ocean Optics, USA) with a filter <400 nm, a UV-VIS linear photodiode array spectrometer Cypher II (B&WTech, USA) and the microfluidic setup as described before. The light was directed to the microfluidic chamber and collected via multimode optical fibers (Figure 2.5). Spectra of dark current and the lamp were recorded initially. The online detection was controlled by custom built LabView program (LabView 8.6) and continuously every 2 s a spectrum was recorded. The data analysis was carried out with home grown Matlab software (Matlab 7.1). In order to minimize the noise in the detection of the LSPR peak, the centroid of the LSPR peak was calculated as in [78].

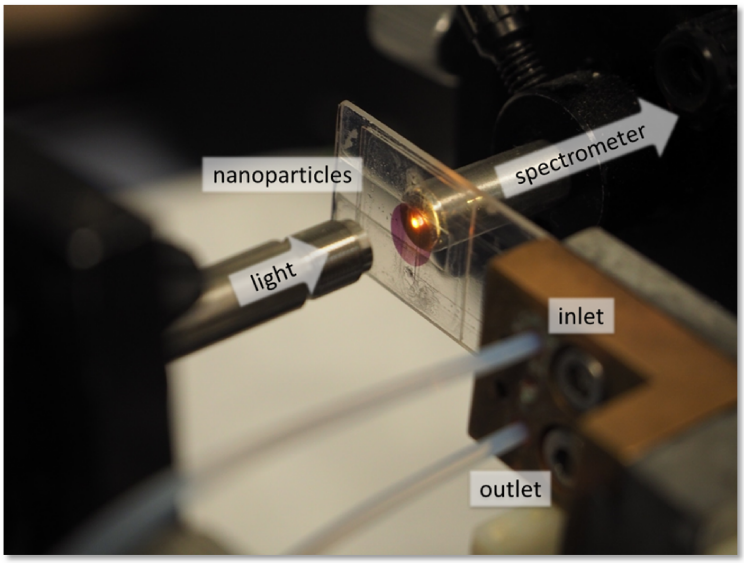

Figure 2.5: LSPR setup with microfluidic chamber with a layer of 80 nm gold nanoparticles (red spot). The light is directed and collected before and after the microfluidic chamber via a multimode optical fiber. A holder connects the tubes for inlet and outlet with the microfluidic chamber.

2.3.3 Setup for sLSPR detection

Before spectra of single nanoparticles are taken, they are observed by microscopy. In the past mainly the light absorption or extinction of metal nanoparticles were detected. Carsten Sönnichsen [79] proved that the scattered light of single nanoparticles can be observed by a dark-field microscope with reflection or transmission geometry. The setup for dark-field microscopy in transmission requires conventional microscope objectives and a dark-field condensor, which illuminates the sample from behind as depicted in Figure 2.6 - A. The aperture in the dark-field condensor blocks the directly light, which would propagate directly into the objective. Information losses due to refractions between the sample-condensor interface are prevented by immersion oil.

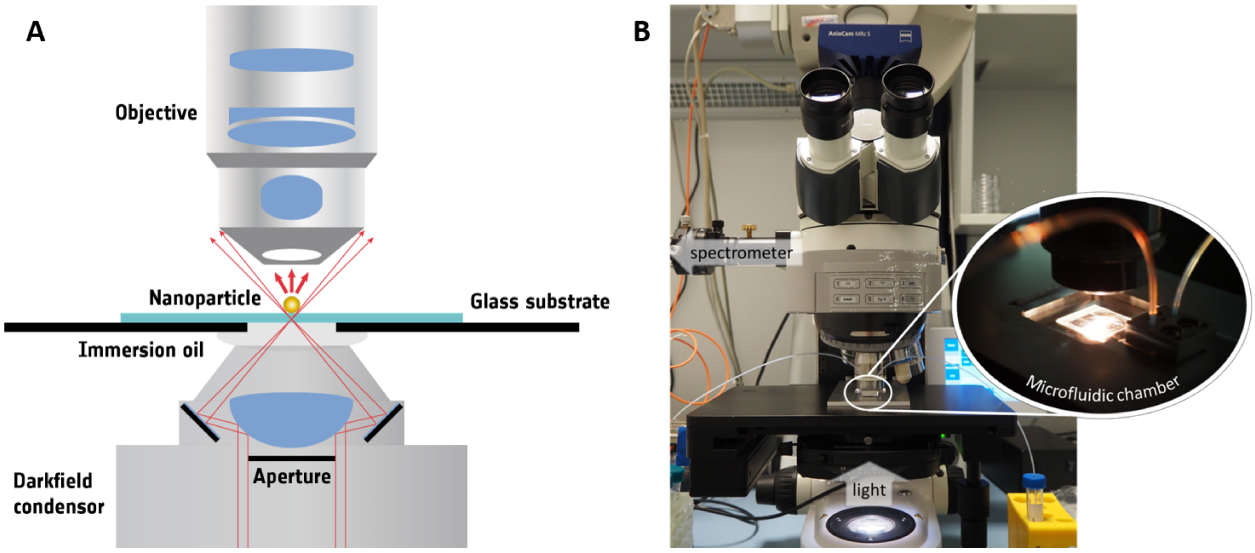

Figure 2.6: A - Dark-field microscope setup with transmission geometry. The light enters a high aperture dark-field condensor and is directed to the nanoparticle. The aperture blocks the direct light and only the scattered light of the nanoparticle propagates directly in the objective. B - Picture of sLSPR setup with microscope and microfluidic chamber.

The sLSPR measurements were conducted with an optical microscope Axio Imager Z1.m (Carl Zeiss Micro-imaging, Göttingen, Germany) in dark-field mode in transmission geometry with a 100x objective (Zeiss EC epiplan-NEOFLUAR, 0.75 HD, DiC,1156-538) (Figure 2.6 - B). The illumination source was a tungsten halogen lamp having a continuous broad band spectrum. The scattered light from a single nanoparticle was collected via a multimode fiber with a pinhole of 100 μm placed at the image plane of the microscope. The fiber was connected to an Acton Research SpectraPro 2300i micro-spectrometer (Princeton Instruments, Trenton, USA) with a grating of 150 lines per mm and a peltier-cooled CCD camera Pixies 256 (Princeton Instruments, Trenton, USA). For the online detection of the spectra and correction of the x-y and z-plane changes a home grown LabView program was used. The dark current (I_{DC}) and lamp spectrum (I_L) were detected in advance to the measurement with an integration time of $\sim$ 0.1 s depending on the light intensity. The background (I_{BG}) was measured directly beside to the measured nanoparticle with an integration time of 10 s. A single nanoparticle (I_{NP}) was chosen on the basis of the color and spectrum and the spectra were measured continuously with an integration time of 10 s. The spectral data was normalized to the lamp spectrum as following

$$I_{norm} = \frac{I_{NP} - I_{BCG}}{I_L - I_{DC}} \tag{2.1}$$

with I_{norm} as final processed data. In order to minimize the noise in the detection of the

LSPR peak, the centroid of the LSPR peak was calculated as described in [78]. Further data analysis was carried out with a Matlab program.

2.4 Bulk refractive index measurements

Bulk refractive index measurements were carried out as following: $3dH_2O$ was used as running buffer which continuously flew with $50\,\mu l/min$ (SPR system) or $20\,\mu l/min$ (LSPR and sLSPR system). Glucose solutions with different mass percentages (1 to 50%) were prepared for the SPR and LSPR measurements. The solutions were continuously infused with the same flow rates as used for $3dH_2O$. In case of the sLSPR measurements glycerol solutions (about 87%, Merck) with mass percentages of 25%, 50% and 75% were prepared and infused with an increased flow rate up to $100\,\mu l/min$. Afterwards the flow was stopped for 5 min. The solutions were freshly prepared for each measurement and the running buffer was filtered by syringe filters (Rotilabo, pore size $0.22\,\mu$m, Carl Roth GmbH & Co. KG, Germany). The refractive indices were measured by the pocket refractometer B331500 from Atago.

2.5 Functionalization of nanoparticles

2.5.1 Layer-by-layer deposition with polyelectrolytes

As running buffer 0.5 M NaCl was used and 30 mg of poly(allylamine hydrochloride) (PAH, $M_w \sim 58\,000$) and poly(sodium 4-styrenesulfonate) (PSS, $M_w \sim 70\,000$) were diluted separately in 15 ml 0.5 M NaCl. The measurements with the SPR system were performed with a probe loop of $60\,\mu l$ and a flow rate of $20\,\mu l/min$ during injection of the polyelectrolyte solutions. The measurements with the LSPR system were performed with a probe loop of $100\,\mu l$ and a flow rate of $20\,\mu l/min$. The running buffer was filtered by syringe filters (Rotilabo, pore size $0.22\,\mu$m, Carl Roth GmbH & Co. KG, Germany) in advance.

2.5.2 Layer-by-layer deposition with proteins

For the protein adsorption a citrate buffer with pH = 4.0 was prepared (see in appendix 6) and used as running buffer. $100\,\mu g/ml$ Bovine Serum Albumin (BSA, Fraction V, M_w~69 000, Carl Roth) was diluted in citrate buffer pH = 4.0. As alternate layer 0.1% dextrane sulfate (sodium salt from Leuconostop, Fluka BioChemika) was used. The solutions were stored at 4°C in fridge after preparation. For the SPR and LSPR measurements citrate buffer pH = 4.0 was used as running buffer and filtered by syringe filters (Rotilabo, pore size $0.22\,\mu$m, Carl Roth GmbH & Co. KG, Germany). The SPR chamber was heated to

35°C, and a flow rate of 50 $\mu l/min$ was adjusted. The LSPR system was performed at room temperature and with a flow rate of 20 $\mu l/min$.

2.5.3 Adsorption of single-stranded DNA and hybridization

Different DNA sequences were used as described in further detail in table 1.

Name	Length	Sequence ($5' - 3'$)	Modification
Asper2_T5	27	$SH-(CH_2)_6-(T)_5GGGTTCAGCCTCACTGTCATGG$	5′-Thiol
Asper2_T10	32	$SH-(CH_2)_6-(T)_{10}GGGTTCAGCCTCACTGTCATGG$	5′-Thiol
Asper2_A10	32	$(A)_{10}-GGGTTCAGCCTCACTGTCATGG$	poly(A)
Asper2_A15	37	$(A)_{15}-GGGTTCAGCCTCACTGTCATGG$	poly(A)
Asper2_T5_A10	37	$(A)_{10}-(T)_5GGGTTCAGCCTCACTGTCATGG$	poly(A)
Asper2_T5_A15	42	$(A)_{15}-(T)_5GGGTTCAGCCTCACTGTCATGG$	poly(A)
Asper2c	22	$CCATGACAGTGAGGCTGAACCC$	
Leg4_A5	24	$(A)_5-CGATACAGAGGGCGGCGAA$	poly(A)
Leg4_A10	29	$(A)_{10}-CGATACAGAGGGCGGCGAA$	poly(A)
Leg4_A20	39	$(A)_{20}-CGATACAGAGGGCGGCGAA$	poly(A)
Leg4_A30	49	$(A)_{30}-CGATACAGAGGGCGGCGAA$	poly(A)
Leg4c	19	$TTCGCCGCCCTCTGTATCG$	
Leg5_T5	25	$SH-(CH_2)_6-(T)_5GGGTTAAGTCCCGTAACGAG$	5′-Thiol
Leg5c	20	$CTCGTTACGGGACTTAACCC$	
PS2.M	22	$SH-(CH_2)_6-(T)_5GGGTAGGGCGGGTTGGG$	5′-Thiol

Table 1: Overview of the different DNA Sequences

The HPLC cleaned and lyophilised DNA strands were purchased from *biomers.net* and stored at 4°C until use. Afterwards the DNA was diluted with $3dH_2O$ according to manufacturer's data. 100 μl of thiol-modified capture DNA diluted in the filtered running buffer (KH_2PO_4 or citrate buffer pH = 3.0) was infused into the microfluidic chamber with a flow rate of 20 $\mu l/min$. The DNA concentrations differed from 10 nM to 1 μM. After capture DNA immobilization the flow rate was increased to 100 $\mu l/min$ and the running buffer was changed to 5xSSC. The target DNA was diluted in 5xSSC with a concentration range of 100 nM to 1 μM depending on measurement. The injection executed at a flow rate of 20 $\mu l/min$. The PCR product was the complementary part of the Leg5 DNA sequence and consisted of 262 bases. The PCR product was diluted in 5xSSC, heated to 95°C for 5 min and cooled in ice for 2 min to gain single strands. Afterwards the target PCR solution was injected at a flow rate of 20 $\mu l/min$. The DNA amplification was executed by Stefanie Hentschel.

2.5.3.1 Coadsorption of mercaptohexanol

As coadsorption 1 mM 6-Mercapto-1-hexanol (MCH) diluted in $3dH_2O$ was used. The solution was infused during continuous flow of 5xSSC as running buffer. The flow rate for MCH was the same as for DNA injection: $20\,\mu l/min$.

Figure 2.7: Chemical structure of 6-Mercapto-1-hexanol.

2.5.3.2 Denaturation of DNA

For denaturation of the target DNA from the capture DNA, 1 M NaOH was injected into the microfluidic chamber with a flow rate of $100\,\mu l/min$.

2.5.3.3 Adsorption of G-quadruplex forming DNA and hemin binding

For the detection of hemin, the DNA for G-quadruplex formation had to be adsorbed on the nanoparticles' surface. Therefore $1\,\mu M$ DNA (sequence PS2.M) in citrate buffer pH = 3.0 was infused into the microfluidic chamber (LSPR). Afterwards the running buffer was changed to Tris-Buffer. For coadsorption 1 mM 6-Mercapto-1-hexanol (97%) diluted in $3dH_2O$ was used. Hemin stock solution was prepared in dimethyl sulfoxide (DMSO) and stored in dark at $-30°$C for max. 1 month. Before injection into the microfluidic chamber, hemin was diluted to $50\,\mu M$ in Tris-Buffer. During injection, a flow rate of $20\,\mu l/min$ was used, else $100\,\mu l/min$ for washing.

3 Results

3.1 Theoretical comparison of SPR and LSPR as transducer

The electromagnetic field of a nanoparticle decays approximately ten times more quickly than on a gold film (Figure 3.1). Therefore, the penetration depth of the electromagnetic field on a nanoparticle is also 10 times lower compared to the SPR sensing system. The penetration depth l_d ranges between 5 - 30 nm depending on the size of the nanoparticle. This big difference of decay length and further sensing volume has to be considered during bulk refractive index measurements and surface refractive index measurements. [80, 81]

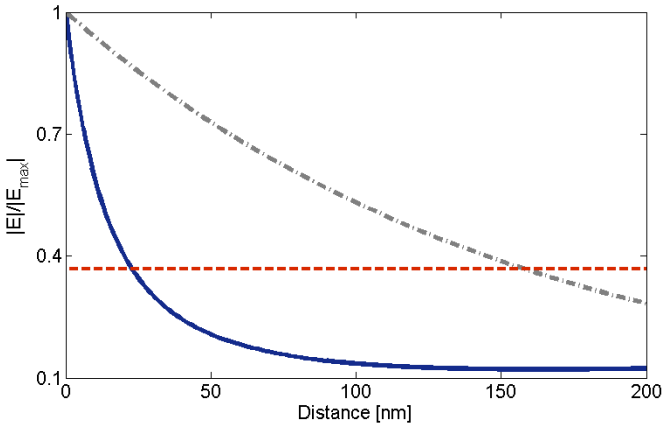

Figure 3.1: Calculated penetration depths for a gold film (grey-dotted) and a 80 nm spherical gold nanoparticle (blue). The penetration depth defined as 1/e is marked by the red dashed line.

Bulk refractive index sensitivity S_b is defined as refractive index change in the whole medium surrounding the gold film/nanoparticle. [82]

$$S_b = \frac{\Delta\lambda_{peak}}{\Delta n_{medium}} \tag{3.1}$$

In contrast, the surface refractive index sensitivity S_s is confined to refractive index changes in a thin layer at the surface of the gold film/nanoparticle. [82]

$$S_s = \frac{\Delta\lambda_{peak}}{\Delta n_{layer}} \tag{3.2}$$

The relationship between the signal of the SPR or LSPR system and the refractive index and thickness of an adsorbed layer can be calculated and is shown in Figure 3.2. For comparable results the effective refractive index change Δn_{eff} in refractive index units (RIU) was

calculated for the SPR system after the equation 1.2 and for nanoparticles after

$$\Delta n_{eff}(d, n_l, n_b) = \frac{\Delta\lambda_{peak}}{S_b}[RIU] \tag{3.3}$$

Additionally, the E-field profiles for a gold film with a thickness of 50 nm and spherical gold nanoparticles with a diameter of 30 and 80 nm are depicted. The calculations base on Maxwell equations for stratified medium and Mie theory of SPR and LSPR. The E-field profiles show that the field of a gold film extends much more than the field on the nanoparticles and that the field distribution depends on the nanoparticle size. It shows that the adsorption of a thin layer on the gold film leads to a linear behavior at the SPR system and a non-linear behavior at the LSPR system. Further the non-linear behavior can be tuned by the size of the nanoparticle. [83]

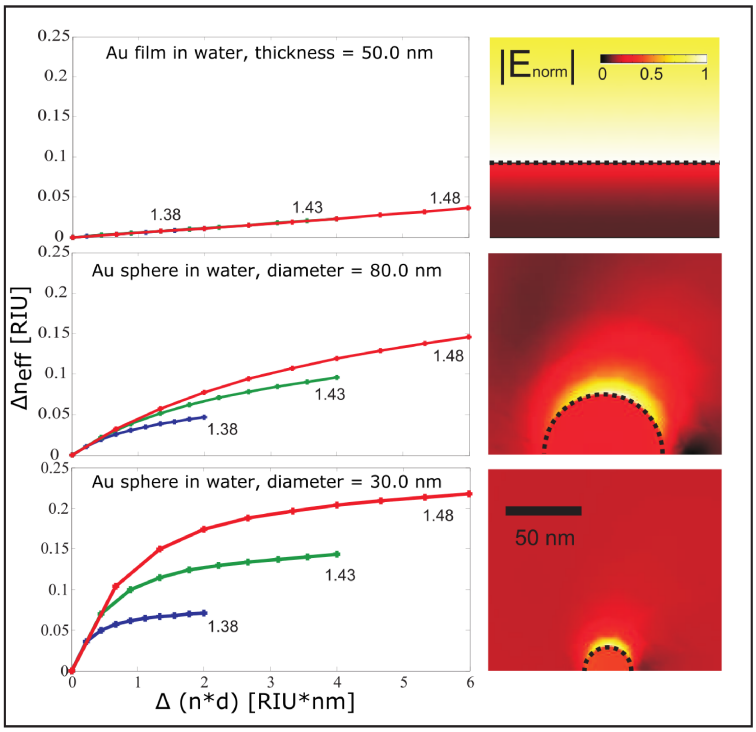

Figure 3.2: Calculated dependence of the transducers signal Δn_{eff} to changes of refractive index of the layer (with water as bulk medium) and the layer thickness. The different curves represent different refractive indices (numbers along the curves) of the adsorbed layer. Top - on a gold layer (SPR), Middle - on a 80 nm spherical gold nanoparticle, Bottom - on a 30 nm spherical gold nanoparticle. Right images - electrical field decaying from the different nanostructures. The electric field is normalized on its maximal value around the nanostructure in the plasmon resonance. The confined field at the nanoparticles is clearly visible.

The graphs in Figure 3.2 show moreover that conformational changes cannot be detected with the SPR system. Δn_{eff} does not change if the refractive index and the thickness of the layer are varied by conformational changes of the molecules, as depicted in Figure 3.2 - top graph. The product of the thickness and refractive index of the layer ($n*d$) is only influenced by the surface density of the adsorbed molecules because the refractive index change will be equalized by the inverse change of the thickness. [84] In contrast, the strong confined electromagnetic field of the nanoparticles allows detection of these conformational changes. In Figure 3.2 - middle, bottom graph, it is clearly visible that a refractive index change and a constant product of $n*d$ induces in total a signal change. This can be used for determination of the layer thickness. [83]

3.2 Characterization and sensitivity determination of applied transducers

3.2.1 Gold film as transducer - SPR

The SPR system based on a flat gold film was initially investigated for its sensoric response by injection of solutions with different refractive indices. As seen in Figure 3.3 - A, a stable signal was achieved before and after infusion (infusion time interval shaded in grey) of the glucose solution with water in continuous flow. Each glucose solution led to a direct change of the SPR signal. The different solutions were prepared with the same proportion; therefore a linear increase of the maximum SPR signal was expected. This was not totally fulfilled, the second solution showed a decreased signal change than expected. The solutions' refractive index were measured with a hand-held refractometer (as described in 2.4) for quantification; their values are inserted in Figure 3.3 - A. The refractive indices measured by the SPR system and the hand-held refractometer are directly compared in Figure 3.3 - B. Ideally, the same refractive indices are measured with both systems resulting in a linear slope of 1. The calculated slope for the presented measurement is 0.82 corresponding to a measuring difference of 18%. The slope difference is influenced by the measurement error at the second solution and by an inaccuracy of the SPR system, which can be eliminated by calibration of the SPR system.

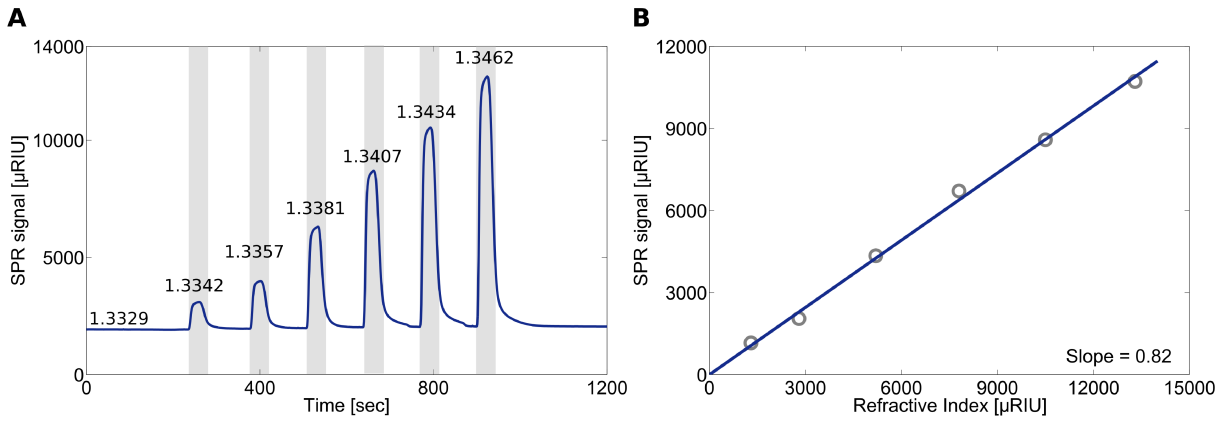

Figure 3.3: A - Detection of SPR signal change induced by refractive index change in the surrounding medium. Glucose solutions with different concentrations were rinsed over the gold film for 2 min (dashed in grey). The values of the refractive indices belong to each solution and were measured with a hand-held refractometer. Water was continuously injected before and after the target solutions. B - Comparison of the solutions' refractive index measured with the hand-held refractometer and the SPR system extracted from the left diagram. The linear slope is 0.82.

3.2.2 Immobilized nanostructures as layer for transducers - LSPR

Nanostructures exist in a wide variety of shapes, material and sizes. Different nanostructures were investigated to determine the most applicable transducer as DNA biosensor with the applied setups. As schematically shown, the different nanostructures included spherical gold nanoparticles with diameters of 30 nm, 60 nm and 80 nm (see Figure 3.4) and anisotropic nanoparticles, so-called gold nanopeanuts (due to their shape) with a size of 65x40 nm (see Figure 3.5) and silver nanoprisms with gold edges with an edge length of 60 nm and a height of 12 nm (see Figure 3.6). The studied nanoparticles were immobilized on glass, characterized spectrally and topologically with Atomic Force Microscopy (AFM), Scanning Electron Microscope (SEM) or Transmission Electron Microscopy (TEM).

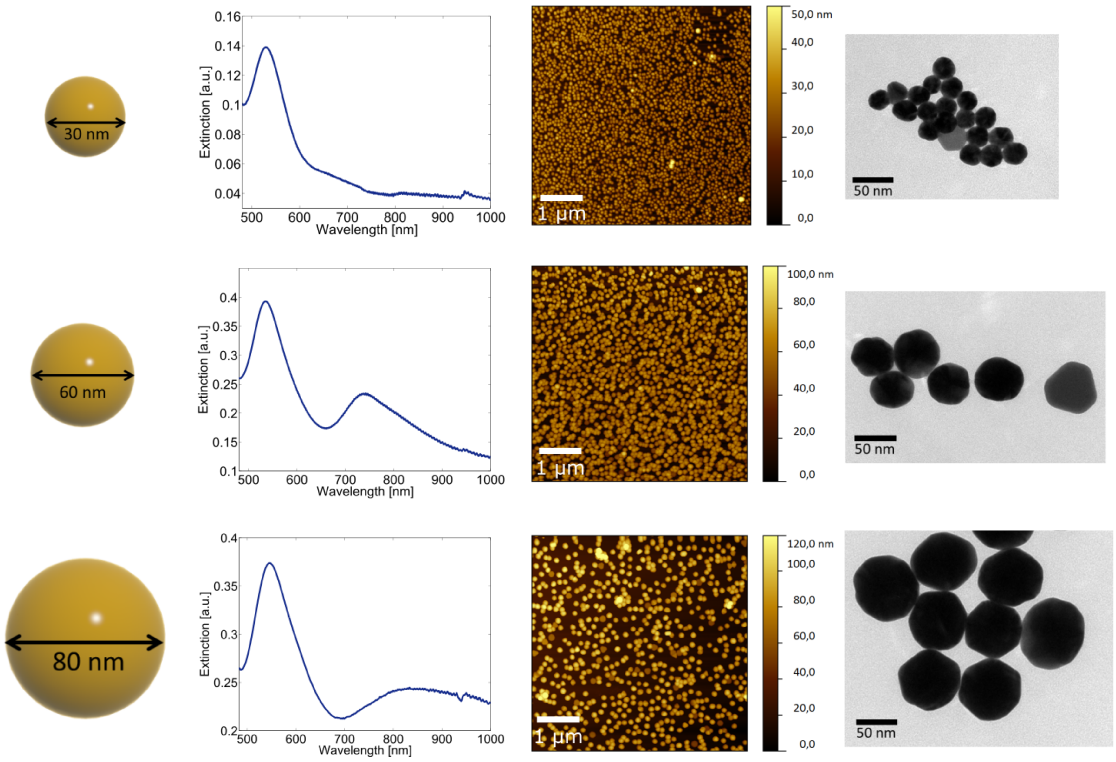

Figure 3.4: Optical and topological overview of the investigated spherical nanostructures. The different sizes are shown schematically on the left side. The optical characteristics are shown by the spectra, which were taken of the nanostructures immobilized on glass, implemented in a microfluidic chamber and embedded in water (middle). The surface topologies of the glass slides with immobilized nanoparticles are shown by AFM and TEM images to further confirm the size and size distribution.

The spectra were taken after the glass substrates with the immobilized nanoparticles were implemented into the microfluidic chamber and flushed with water. The shape of the spectra and the position of the spectral maximum (λ_{max}) varied as expected due to size and shape differences of the nanoparticles (see Figure 1.1.3). The spherical nanoparticles with diameters of 60 and 80 nm and the nanopeanuts showed two peaks in their spectrum. In the case of the spherical nanoparticles the high density on the glass substrate led to so-called coupling effects, an interaction of the electromagnetic fields surrounding the nanoparticles. [85, 86]

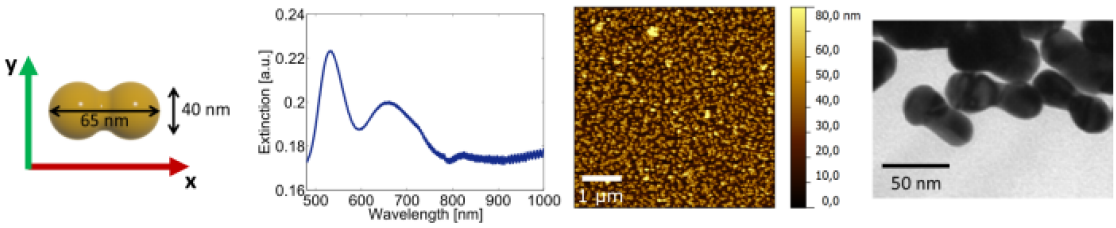

Figure 3.5: Optical and topological overview of the investigated nanopeanuts. The sizes are shown schematically on the left side. The optical characteristics are shown by the spectra, which were taken of the nanostructures immobilized on glass, implemented in a microfluidic chamber and embedded in water (middle). The surface topologies of the glass slides with immobilized nanoparticles are shown by AFM and TEM images to further confirm the size and size distribution.

The nanopeanuts in contrast show a second peak due to their oblongness. They were immobilized on glass with random orientation and the localized surface plasmon resonance was induced with an unpolarized light source. Therefore, two polarization modes are generated, in transverse and longitudinal direction, which can be seen spectrally as peak at 553 nm for transverse direction (y-direction) and 662 nm for longitudinal direction (x-direction).

Silver-Nanoprisms are very sensitive to environmental changes e.g. pH, temperature, chemicals etc. [87] To prevent a reshaping of the nanoprisms to silver nanoparticles, they were coated with gold on the edges. The stability was tested in solution by addition of NaCl. The solution of the pure silver nanoprisms turned yellow caused by Cl-induced degradation and therefore a reshaping to small silver seeds. (Figure 6.1 in appendix) The coated nanoprisms did not change by addition of salt, the solution stayed bluish. The immobilized silver nanoprisms with gold edges showed a very broad peak with low contrast compared to the other nanoparticles. At the immobilized state the nanoprisms are adsorbed flat on the surface and only excitation of the in plane dipole was visible in the spectrum.

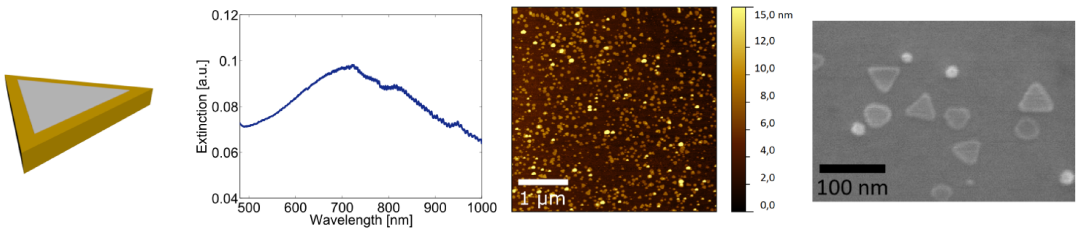

Figure 3.6: Optical and topological overview of the investigated silver nanoprisms with gold edges. The optical characteristics are shown by the spectra, which were taken of the nanostructures immobilized on glass, implemented in a microfluidic chamber and embedded in water (middle). The surface topologies of the glass slides with immobilized nanoparticles are shown by AFM and TEM images to further confirm the size and size distribution.

Measurements with changing bulk refractive index were performed to prove if the immobilized nanoparticles are stable for measurements with continuous flow and sensitive to changes of the surrounding medium (S_b). The glass substrates with the investigated nanoparticles were implemented into the microfluidic chamber and measurements were undertaken with the LSPR setup (setup details are described in chapter 2.3.2).

A representative sensogram of the measurements with spherical 80 nm gold nanoparticles is shown in Figure 3.7. The peak position was determined ($\lambda_{max} = 548.2$ nm), continuously detected and displayed over time. A stable signal was achieved at the beginning of the measurement by continuous flow of water. As already performed with the SPR system, solutions with different refractive indices were injected (as described in 2.4) for 5 min with a washing interval inbetween. The change of the dielectric environment surrounding the nanoparticles between 0.0135 and 0.0688 RIU was clearly detectable. The values of the refractive index were again determined by a hand-held refractometer.

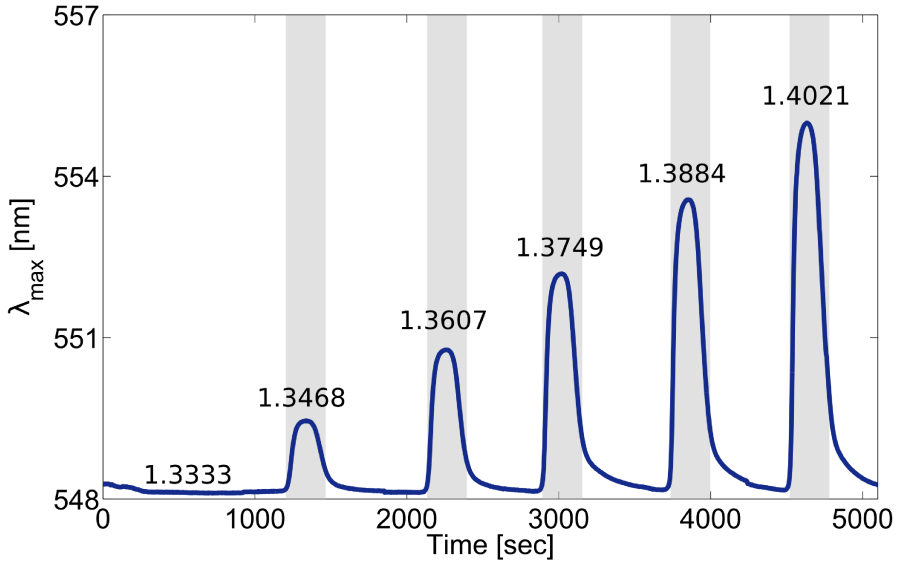

Figure 3.7: Spectral maximum change of 80 nm gold nanoparticles induced by solutions with different refractive indices. Water was used as running agent and different glucose solutions were rinsed for 5 min over the sample (shaded in grey). The refractive index values correspond to each solution and were measured with a hand-held refractometer.

For all nanostructures bulk refractive index measurements were performed, and subsequently their correlation between refractive index change and LSPR signal change ($\Delta\lambda_{max}$) was determined and plotted as shown in Figure 3.8. The linear slope for each nanostructure determines its bulk sensitivity S_b as described in 3.1. The spherical gold nanoparticles show an increase in bulk sensitivity with an increase of size, which is in good agreement with

simulation (section 3.1).

As described before, nanopeanuts show two maximum peaks in their spectrum due to the two plasmon modes. It was possible to detect the signal changes of both spectral maxima during one measurement. Therefore, for both polarization modes the bulk sensitivity was determined. The longitudinal or x-direction mode shows a lower sensitivity than the transverse or y-direction mode with a 4 times higher bulk sensitivity.

The silver nanoprisms with gold edges showed the highest bulk sensitivity. Anisotropic nanoparticles have a confined field at the corners and tips, which leads to a higher sensitivity compared to isotropic (spherical) nanoparticles. But for long-term measurements (several hours) they were not stable in comparison to other nanoparticles. As shown in Figure 3.6 the surface density was low and their extinction peak had a low signal to noise ratio. Small changes on the surface led to high changes in the signal, which could have come from detached residuals on the glass surface (see AFM picture in Figure 3.6).

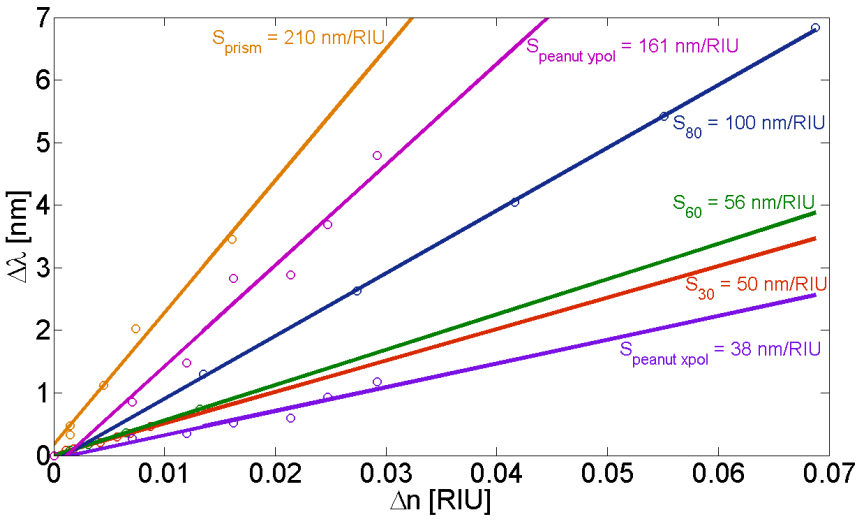

Figure 3.8: Comparison of the bulk sensitivity of the studied nanoparticles. Spectral change induced by refractive index change surrounding the nanoparticles is plotted and the bulk sensitivity for each nanoparticle spot is given by the linear slope.

3.2.3 Single nanoparticles as transducers - sLSPR

Up to now, measurements were conducted by averaging over several nanoparticles densely adsorbed on glass. Sönnichsen et al. [88] had proven that even single nanoparticles can be detected under a microscope in dark-field mode. The question was whether single nanoparticles in a microfluidic chamber can be detected continuously to achieve an online detection for biosensing. A low nanoparticle density on the glass substrate was achieved by dilution

of the nanoparticle solution. It cannot be totally excluded that anisotropic nanoparticles or agglomerations of nanoparticles are adsorbed on the surface. Hence, preliminary investigations were undertaken in air to identify single spherical nanoparticles with a size of 80 nm. The substrate was observed under a dark-field microscope in transmission geometry and the resulting camera image (RGB image) is shown in Figure 3.9. Four nanoparticles were chosen and their spectra were measured and normalized to the lamp spectrum as described in section 2.3.3. The shape of the spectra vary according to the different colors in the camera image. The associated AFM images illustrate clearly the differences of the nanoparticles. The preliminary tests show that single nanoparticles can be identified with the help of the color in the RGB image and the spectrum. In case of 80 nm spherical nanoparticles the spectrum consists of one peak with a maximum at 540 nm and, as a consequence, the nanoparticle color is green in the RGB image. Light spots with other colors or spectral data were not taken into account for single nanoparticle measurements.

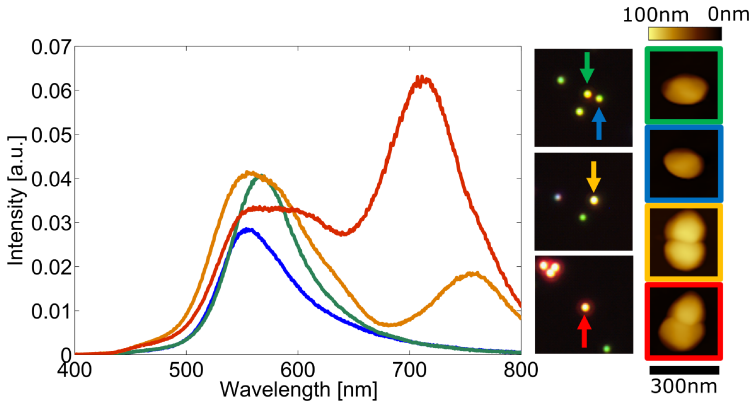

Figure 3.9: Overview of nanoparticles immobilized on glass. The spectral behavior changes with size, shape and distance of close-by nanoparticles. This can be observed by change of the color in the dark-field image and in more detail spectrally.

These pre-observations were important to quickly identify single nanoparticles in the microfluidic chamber. For bulk sensitivity measurements a new microfluidic chamber with holder was designed, where a glass slide with immobilized single 80 nm spherical gold nanoparticles were implemented and mounted into the microscope (details seen in section 2.3.3). The nanoparticles were observed under the microscope and a single one was chosen by dark-field image and verified by spectral analysis. Subsequently, the bulk refractive index measurement was carried out, shown in Figure 3.10 - A. A distinct spectral maximum change was detected with refractive index changes. Each solution was injected twice to confirm the sensoric activity of the single nanoparticle. The flow was stopped after the target solution was inside the chamber, and spectra were continuously measured for 5 min before the chamber

was rinsed with water. At the detection of solutions with higher refractive index, an increase of λ_{max} is visible for approximately 3 min after the stop of the injection. The refractive index values were again measured by a hand-held refractometer. The slight change of the baseline was taken into account at the quantification of the induced shifts ($\Delta\lambda_{max}$), shown in Figure 3.10 - B. The resulting bulk sensitivity for the first injection is 71 nm/RIU and for the second injection 75 nm/RIU.

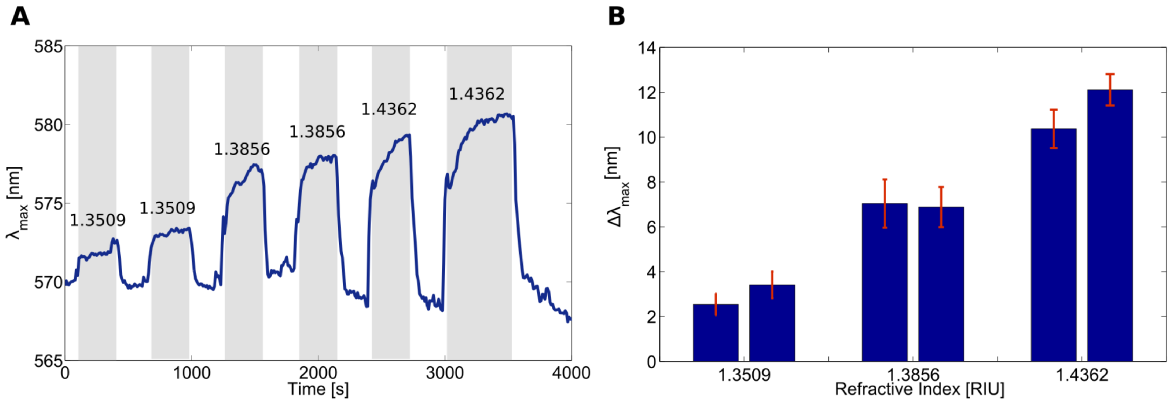

Figure 3.10: A - Spectral maximum change of a single 80 nm gold nanoparticle induced by solutions with different refractive indices. Water was used as running agent and different glycerine solutions were rinsed over the sample (shaded in grey). The different solutions were infused into the chamber, the flow was stopped for 5 min and restarted again afterwards. B - Spectral maximum change of each solution. The change of λ_{max} was calculated from the baseline before injection to the plateau when the solution is inside the microfluidic chamber. The error bars are the average signal noise.

3.3 Comparison of transducer performances by molecular layer adsorption

After detection of solutions with different refractive indices and determination of the nanoparticles' bulk sensitivities, further investigations were realized by application of a biomolecule model to the presented systems. Nanometer thin polyelectrolyte layers (PEL) were adsorbed by layer-by-layer technique on the gold transducers and their kinetic behavior during adsorption was followed. The results of the PEL adsorptions monitored with the different systems SPR, LSPR and sLSPR will be presented and compared.

3.3.1 Polyelectrolyte layers on gold film - SPR

PEL were adsorbed on the gold film under continuous flow. Their alternate adsorption was realized by utilizing their opposite charges: poly(allylamine hydrochloride) (PAH) positively charged and poly(sodium 4-styrenesulfonate) (PSS) negatively charged. As seen in Figure 3.11, a stable signal was achieved with the running buffer 0.5 M NaCl. The PEL solutions were alternately infused (color shaded area) with a period of running buffer inbetween (white area) and a total amount of 20 layers. The SPR signal change of the first five layers is shown in Figure 3.11, where each PEL was adsorbed in 2 min. The kinetic behavior differs compared to the refractive index measurements. It is clearly visible that each layer adsorbs on the gold surface because the SPR signal stabilizes on a different level and does not go back to the baseline. The two polyelectrolytes show different kinetic behavior during adsorption: PAH leads to a lower increase than PSS. The change back to the running buffer results in a slight increase of the SPR signal. Even though the polyelectrolytes were diluted in the running buffer it can be a change of the bulk refractive index or the layers swell due to additional salt ions in the buffer.

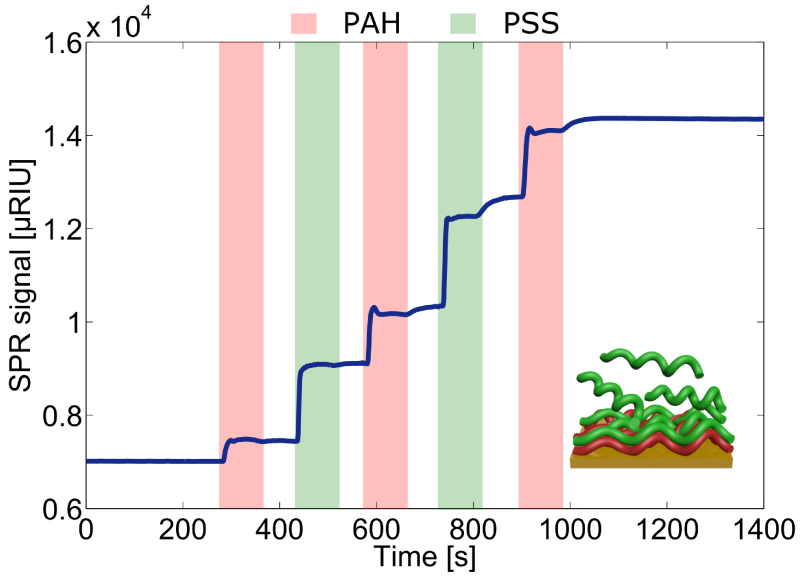

Figure 3.11: Observation of SPR signal change induced by layer-by-layer adsorption of polyelectrolytes on gold film. The alternative adsorbed layer consisted of positively charged poly(allylamine hydrochloride) (PAH - red) and negatively charged poly(sodium 4-styrenesulfonate) (PSS - green). The colored boxes depict the time frame of infusion. 0.5 M NaCl was used as running buffer and buffer for dilution of the polyelectrolytes.

3.3.2 Polyelectrolyte layers on nanostructures - LSPR & sLSPR

After practicability tests of PEL as a biomolecule model on a gold surface, the same system was investigated with the LSPR setup with different nanostructures and the sLSPR setup with single 80 nm nanoparticles. The same nanostructures as introduced before (see chapter 3.2.2) were used as transducers. The measurements with the nanoprisms were excluded because no stable signal could be achieved during continuous flow with running buffer. As a representative example, the alternate PEL adsorption of six layers on 80 nm spherical gold nanoparticles is shown in Figure 3.12. In total, twenty layers were adsorbed and detected. A stable signal was achieved with the running buffer 0.5 M NaCl and a stepwise increase of λ_{max} was measured during layer-by-layer adsorption as with the SPR system. The positively charged polyelectrolyte PAH was applied first because it is generally accepted that nanoparticles have a negatively charged surface induced by the weakly adsorbed negatively charged citrate as stabilization factor.[38] In comparison to the other layers the first layer gives a low signal change, which is comparable to the SPR measurement. Another reproducible observation is that the solutions show different amount of signal change; PAH gives a lower signal change than PSS.

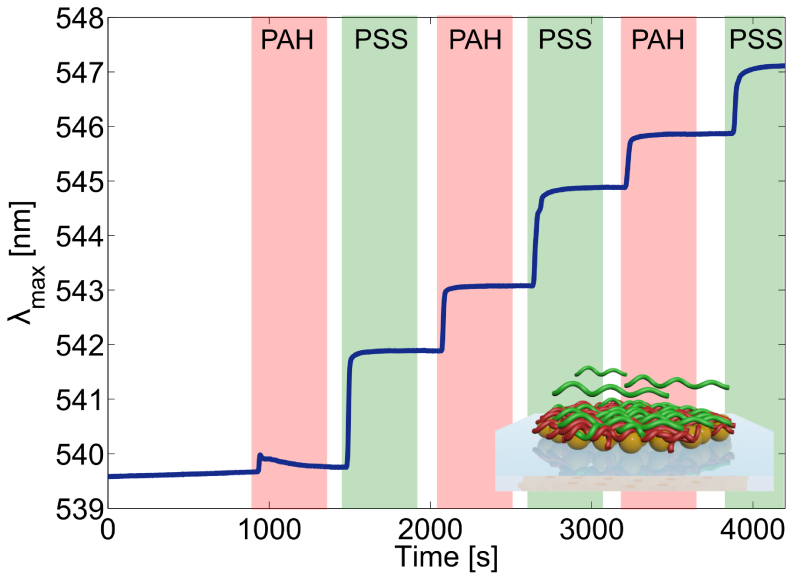

Figure 3.12: Spectral maximum change induced by layer-by-layer adsorption of polyelectrolytes on 80 nm gold nanoparticle layer. The colored boxes (PAH - red, PSS - green) depict the time frame of polyelectrolyte solution infusion. 0.5 M NaCl was used as running buffer and buffer for dilution of the polyelectrolytes.

For all nanostructures the same adsorption behavior was observed, summarized in Figure 3.13. The spectral maximum change induced by PEL layers is plotted for all nanostructures. The highest surface sensitivity was determined for the longitudinal plasmons of the nanopeanuts, consequential they showed the highest shifts with the PEL layers. The spherical nanoparticles showed, as expected, with 30 nm the lowest shifts and with 80 nm the highest. It was also possible to measure the nm-thin layers on a single 80 nm spherical gold nanoparticle with the sLSPR setup. The results show a higher sensitivity compared to the average signal of the 80 nm spherical nanoparticles as a layer (LSPR setup).

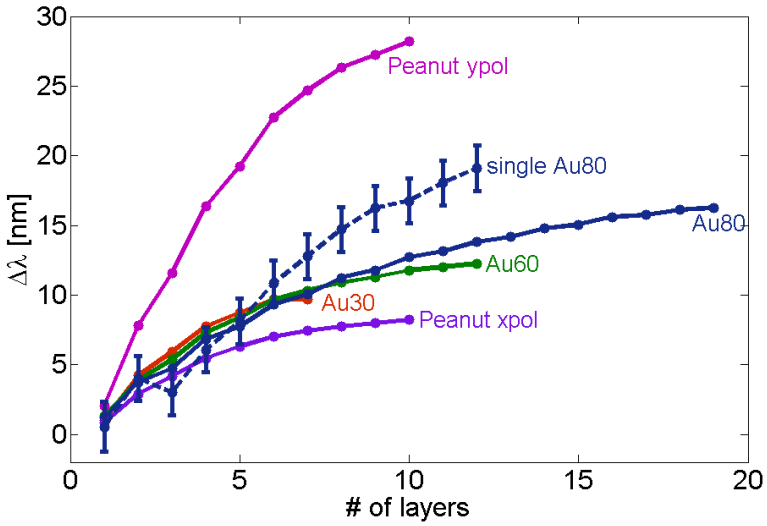

Figure 3.13: Spectral maximum change of the investigated nanoparticles induced by adsorption of polyelectrolyte layers. All measurements were executed with the LSPR system, except single Au80, which was done with the sLSPR system.

3.3.3 Comparison of different systems

On the basis of the PEL detection the new LSPR and sLSPR systems can be compared to the already established SPR system, which gives information about their sensitivity for biomolecule detection. For comparison the LSPR and sLSPR results were changed into the effective refractive index (n_{eff}) after equation 3.3. The difference in error is determined by comparison of the basic signal during continuous flow. For the LSPR and sLSPR system the results with 80 nm nanoparticles were chosen. As shown in Figure 3.14, the most stable signal was achieved with the SPR system. The other systems have 100x (LSPR) or even 1000x (sLSPR) higher signal changes compared to the SPR signal. The noise of the SPR system is 100/1000 times lower than with the other systems.

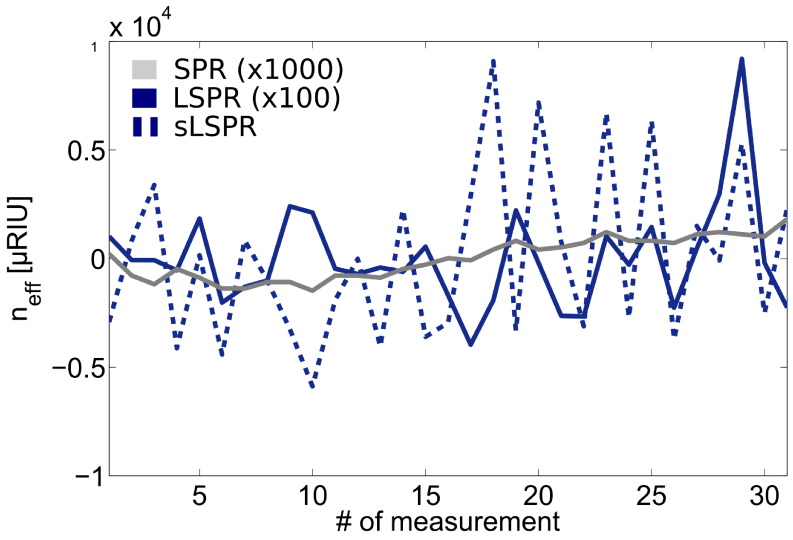

Figure 3.14: Direct comparison of the limit of detection with the different systems: gold film (SPR), gold 80 nm nanoparticle layer (LSPR) and single gold 80 nm nanoparticle (sLSPR).

It is now possible to compare the performance of the three systems during the detection of PEL. In Figure 3.15 the recalculated results of the LSPR and sLSPR systems are depicted together with the result of the SPR system (gold layer). The slope of the increase gives information about the surface sensitivity (S_s) which strongly depends on the penetration depth (as described in 3.1). It is clearly visible that changes directly on the nanostructure surface lead to a higher n_{eff} change than on the gold layer.

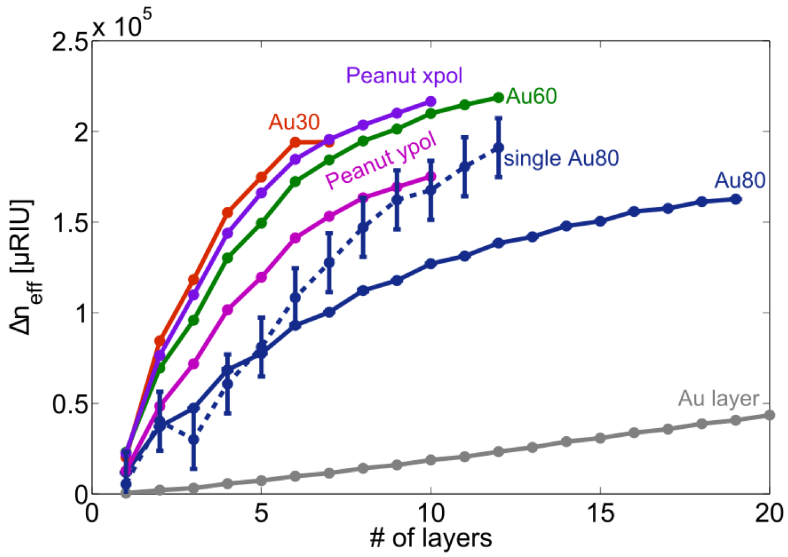

Figure 3.15: Comparison of the induced changes by layer-by-layer adsorption on nanoparticles and gold layer. For comparison the spectral maximum shifts of the nanoparticles were converted into effective refractive index changes by inclusion of the respective bulk sensitivity.

The signal changes for the LSPR with 80 nm nanoparticles and the SPR system are shown in further detail in Figure 3.16. For each layer the n_{eff} change is shown and it can be clearly seen that the signal change decreases with the increase of layer number in case of the LSPR system and stays nearly constant at the SPR system. For both systems PSS gives a higher signal change than with PAH.

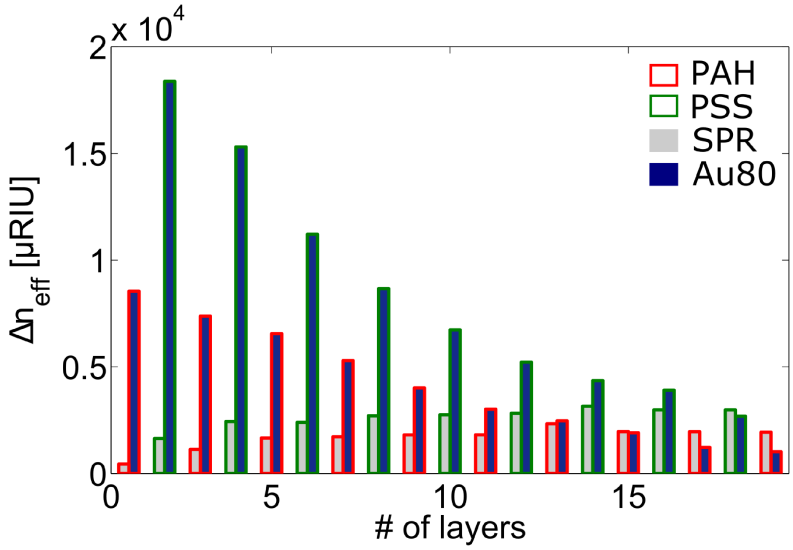

Figure 3.16: Direct comparison of the effective refractive index change by PEL adsorption with the SPR and LSPR system with 80 nm nanoparticles.

3.4 Biomolecule detection

The previous measurements proved the adsorption of the PEL layers. In the following chapter the detection systems are further investigated for detection of biomolecules. Similar to the LbL technique with polyelectrolytes a layer-by-layer adsorption with the protein bovine serum albumin (BSA) and the complex branched glucan dextrane sulfate (DS) will be presented. Subsequently, the main focus will be on the DNA detection and its optimization for a reliable detection of DNA hybridization. In the last chapter, the results of the detection of hemin binding to a G-quadrulex aptamer will be introduced.

3.4.1 Deposition of protein multilayers

After the PEL layer deposition the question was if it is possible to detect adsorption of proteins and protein multilayers. The layer-by-layer deposition was composed of the protein bovine serum albumin (BSA) and the glucan dextrane sulfate (DS) and were applied to the SPR system and the LSPR system with 80 nm nanoparticles. In Figure 3.17 the results for both systems (A - SPR system, B - LSPR system) are shown. Citrate buffer pH = 4.0 was used as running buffer in continuous flow (white background) and alternately the solutions of BSA (red background) and DS (green background) were injected. The results of the LSPR and the SPR in effective refractive index units are directly compared in Figure 3.17 - C.

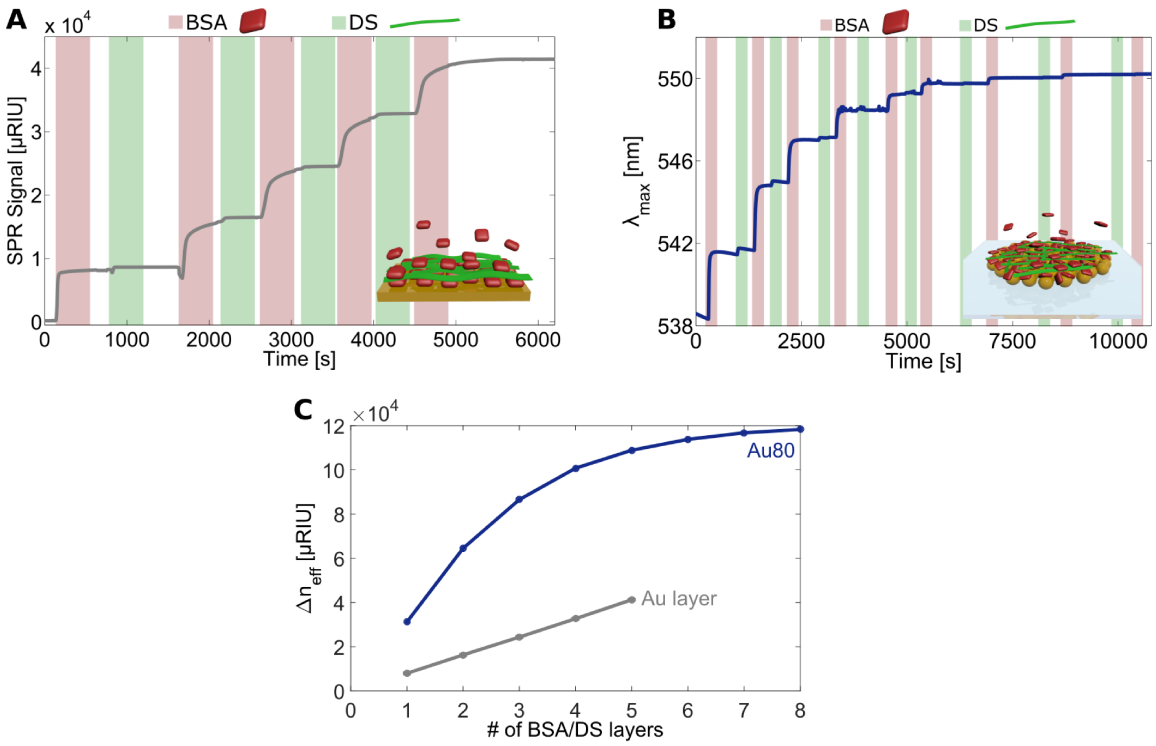

Figure 3.17: SPR signal change (A) and spectral maximum change of 80 nm nanoparticle (B) induced by alternate adsorption of bovine serum albumin (BSA - red) and dextrane sulfate (DS - green) in citrate buffer pH = 4.0, which was also used as running buffer. C - Effective refractive index changes of both systems are plotted.

The same approach with BSA and DS was also studied on the single nanoparticle level (Figure 3.18). Detection of four BSA/DS bilayers was achieved as observable by the spectral maximum change. The BSA or DS solution was infused into the chamber and led to an increase of the signal. Afterwards the flow was stopped and restarted after 5 min incubation time. A maximum of four bilayers were detected because further shifts were not resolvable.

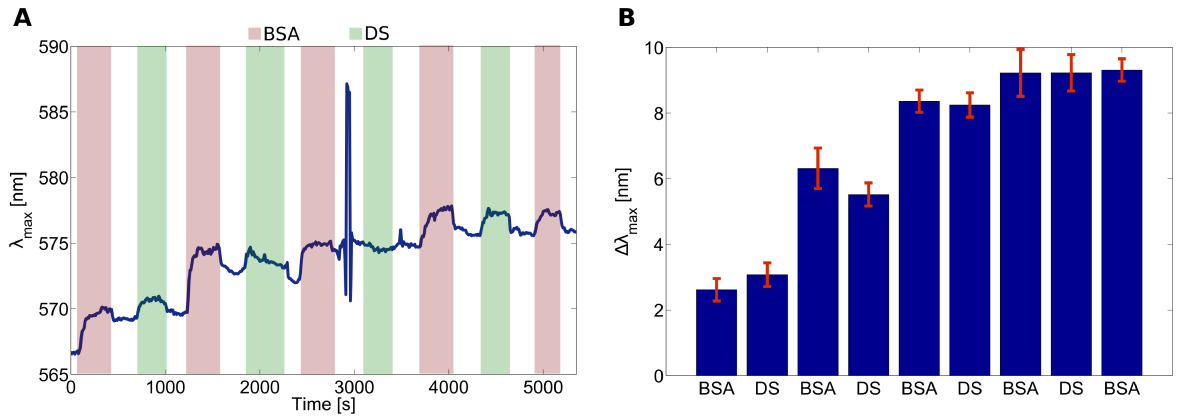

Figure 3.18: A - Spectral maximum change of a single 80 nm nanoparticle induced by alternate adsorption of bovine serum albumin (BSA - red) and dextrane sulfate (DS - green) in citrate buffer pH = 4.0, which was also used as running buffer. B - The spectral maximum change induced by each layer is plotted. The spectral maximum values at the beginning of the measurement (just buffer as surrounding medium) served as baseline. The error bars are the average signal noise.

3.4.2 DNA deposition and hybridization detection

Until now preliminary results were shown to verify the utility of immobilized nanoparticles as biosensor within a microfluidic setup. The following chapter focuses on the main part, the detection of DNA with immobilized nanoparticles. Before the detection of the target DNA can be carried out, the surface of the nanoparticles has to be biofunctionalized with ssDNA. Thereafter, the availability of the DNA for hybridization had to be guaranteed and finally the hybridization of the target DNA was studied.

3.4.2.1 Optimization of biofunctionalization on immobilized nanoparticles

Primarily the immobilized 80 nm spherical nanoparticles were biofunctionalized with ssDNA, capture DNA. As described in chapter 1.2.1, thiol has a high affinity to gold. Therefore, DNA strands with thiol-modification were used as capture DNA. The goal was a homogenous layer of ssDNA (capture DNA) on the nanoparticle's surface with a high accessibility for the hybridization of the target DNA. Different conditions for the biofunctionalization of the nanoparticles were investigated and their influences will be described in the following sections.

Influence of buffer on capture thiol-DNA immobilization

For a fast and reliable immobilization of the capture DNA, two procedures with different buffers were studied. Georgiadis et al. [89] reported the immobilization of ssDNA to gold with 1 M KH_2PO_4 pH = 4.4 as buffer. This protocol was applied to the LSPR system (Figure 3.19 - A). 1 M KH_2PO_4 pH = 4.4 was continuously injected into the microfluidic chamber as running buffer but no stable signal of the baseline was achieved. The injection of 1 μM thiol-modified capture DNA (green shaded) had, after the second infusion, an influence on the signal decrease.

The same procedure was performed with 500 mM citrate buffer pH = 3.0 as buffer after Zhang et al. [52] (Figure 3.19 - B). In contrast to the other buffer, a stable signal of the baseline was achieved and the kinetics of the adsorption of the same capture DNA was directly traceable for both infusions (green shaded). Additionally, it was observed that after the first injection a stable signal was reached and only a small shift was detected with the second injection of the capture DNA. The results show clearly that the citrate buffer with a low pH is the preferable procedure for the adsorption of the capture DNA.

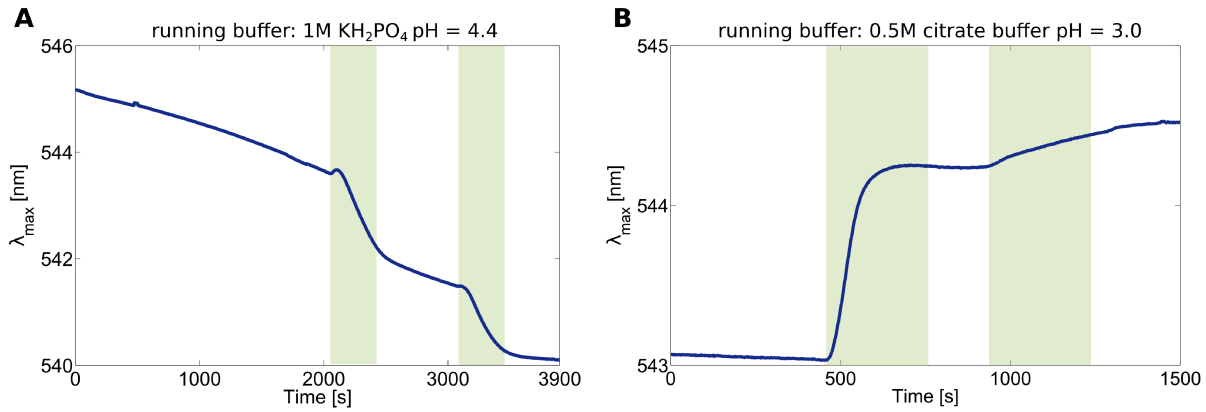

Figure 3.19: Comparison of kinetic behavior of DNA adsorption with 1 M KH_2PO_4 buffer with pH = 4.4 (A) and 0.5 M citrate buffer with pH = 3.0 (B). The DNA sequence Leg5_T5 was used for both experiments.

Effect of plasma etching for transducer surface cleaning

The nanoparticles were stored in a solution with several supplements for stabilization, which are not published by the manufacturer. After immobilization of the nanoparticles on the glass surface, residuals of the stabilization supplements may cause surface impurities. Investigations were conducted to see if the cleaning of the substrates with plasma etching improves the adsorption of the thiol-modified capture DNA to the nanoparticle surface and later on if the hybridization of the target DNA (see in chapter 3.4.2.3) is enhanced. In Figure 3.20, the adsorption of capture DNA to 80 nm spherical nanoparticles with (in grey) and without previous plasma etching (in blue) is depicted. In both cases a spectral maximum shift was visible (Table 2). If the increases of the two conditions are compared, it is visible that with plasma treatment a different signal change was detected. The signal decreases after the first rise and increases again until it stabilizes. In contrast, the measurement without the plasma treatment showed a continuous increase with faster stabilization.

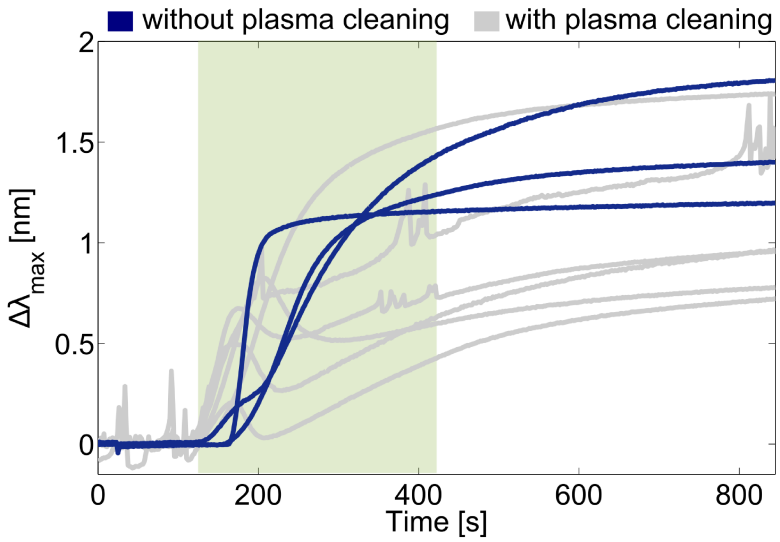

Figure 3.20: Thiol-modified DNA adsorption after transducer cleaning with plasma etching (grey) or without cleaning (blue). All experiments were performed with the DNA sequence Asper2_T5 and citrate buffer pH = 3.0.

	$\Delta\lambda_{max}$	Number of measurements
No plasma treatment	1.49 ± 0.30 nm	3
With plasma treatment	0.99 ± 0.30 nm	6

Table 2: Calculated changes of λ_{max} for measurements with and without plasma treatment.

Effect of different concentrations of capture DNA

For investigations of the sensitivity of the nanoparticles to DNA adsorption, different concentrations of DNA solutions were sequentially infused into the microfluidic chamber (Figure 3.21). The sensogram of the whole measurement is shown in appendix (Figure 6.2).

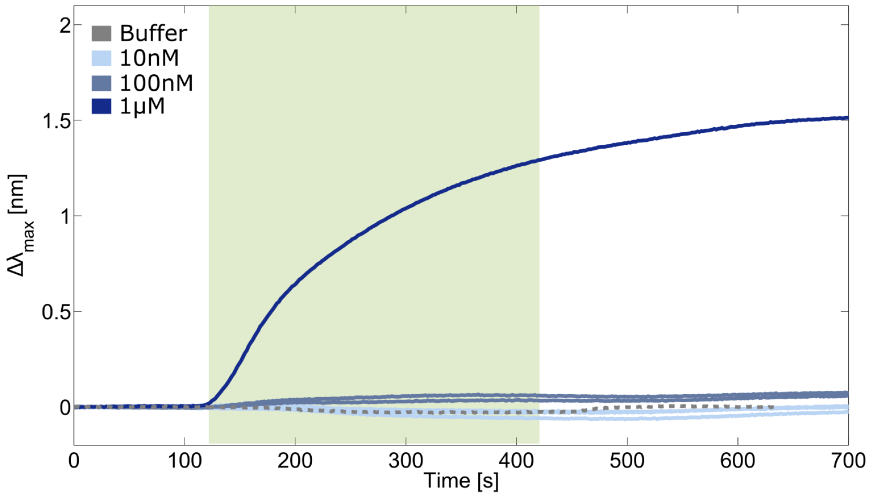

Figure 3.21: Adsorption of thiol-modified DNA (Aspergillus DNA with T5 Spacer) diluted in citrate buffer pH = 3.0 with different concentrations (10 nM, 100 nM, 1 μM). As reference just buffer (dotted grey) with addition of water instead of DNA solution was injected.

The starting concentration of 10 nM show a slight decrease of the spectral maximum. With increase of the concentration to 100 nM a minimal increase of 0.06 nm was detectable. After injection of 10 nM and 100 nM DNA solution twice the usually used 1 μM DNA solution was injected. Even though DNA was already adsorbed onto the surface with lower concentrations a shift of 1.53 nm was achieved. Full saturation of the surface was not achieved with lower concentrations in an appropriate time.

Effect of different capture DNA sequences and spacer lengths

Different sequences were investigated, if they can be detected with the LSPR system. As described in section 1.2.1, from literature it is known that the length of the DNA or the distance between the capture DNA sequence and the nanoparticle surface plays a role in the availability of the sequence for hybridization. Therefore, the spacer length between the thiol-modification and the capture sequence of the DNA was varied. The Aspergillus DNA sequence as well as the Legionella DNA sequence were detectable as shown in Figure 3.22. For both sequences the induced shift of λ_{max} ranged from 0.5 nm to nearly 2 nm (Table 3). Another phenomenon occurred at several measurements, the spectral maximum decreased before it steadily increased.

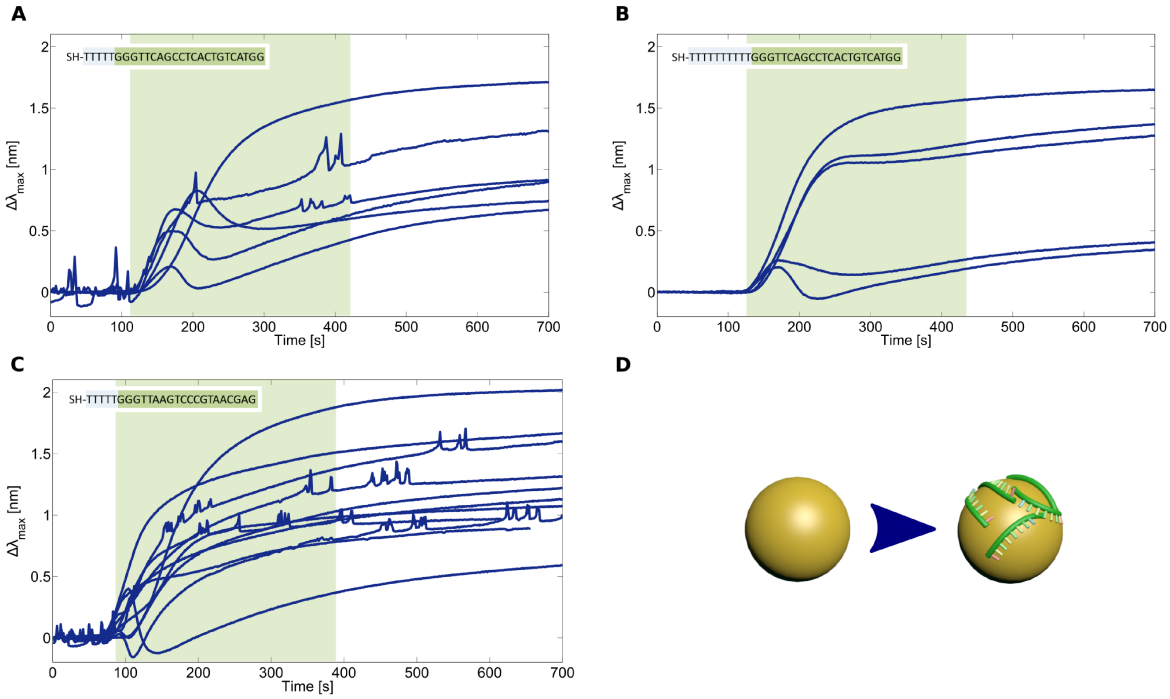

Figure 3.22: Adsorption of thiol-modified DNA with Aspergillus DNA sequence (A & B) and Legionella DNA sequence (C). Further the spacers were varied between 5 (A) and 10 (B) thymine spacer. D - Schematic of the DNA adsorption on a gold nanoparticle.

DNA sequence	$\Delta\lambda_{max}$	Number of measurements
Asper2_T5	1.03 ± 0.41 nm	6
Asper2_T10	1.01 ± 0.61 nm	5
Leg5_T5	1.12 ± 0.36 nm	16

Table 3: Calculated changes of λ_{max} for measurements with different DNA sequences and spacer lengths.

Effect of capture DNA immobilization by poly(A) tail

As described in chapter 1.2.1, the different DNA bases have different affinity to gold. Pei et al. [56] showed that DNA with a poly(A) tail instead of a thiol modification can be adsorbed on gold nanoparticles. This method bears advantages like adjusting distances between the DNA strands and passivate the gold surface at the same time. Experiments were performed with both DNA sequences with different poly(A) tail lengths on the 5' end varying from five to thirty adenine bases. The results and sequences are shown in Figure 3.23. At the Aspergillus sequence an additional thymine spacer was added for better comparison to the results with thiol-modified DNA. All sequences induced a shift as represented in Table 4. The binding and the shifts are comparable to the results with thiol-modified DNA.

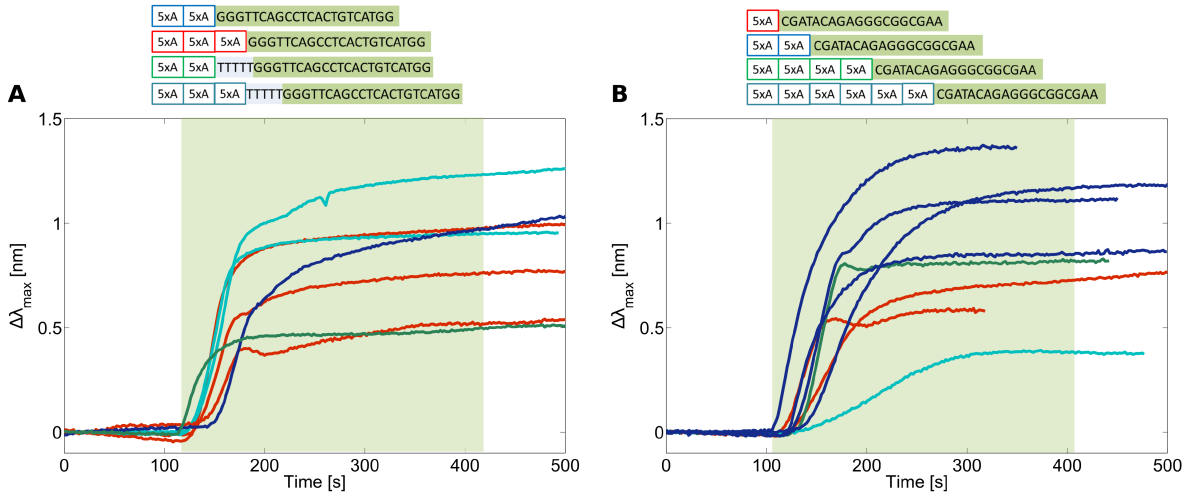

Figure 3.23: Adsorption of DNA with varying poly(A) tails instead of thiol-Modification at 5' end. The DNA sequences are specified above (A - Aspergillus sequence, B - Legionella sequence).

DNA sequence	Number of adenines	Number of thymines	$\Delta\lambda_{max}$	Number of measurements
Asper2	10		0.99 nm	1
Asper2	15		0.77 ± 0.23 nm	3
Asper2	10	5	0.5 nm	1
Asper2	15	5	1.11 ± 0.20 nm	2
Leg4	5		0.65 nm ± 0.1 nm	2
Leg4	10		1.12 ± 0.20 nm	4
Leg4	20		0.83 nm	1
Leg4	30		0.38 nm	1

Table 4: Calculated changes of λ_{max} for measurements with different DNA sequences and poly(A) tails.

3.4.2.2 Effect of coadsorption on capture DNA and hybridization

As already reported in literature (details in chapter 1.2.1), Mercaptohexanol (MCH) improves the accessibility of the capture DNA for hybridization of the target DNA. In the following this method was applied to see if it improves the DNA hybridization. The detection of just MCH to the nanoparticles was tested initially with hybridization buffer (5xSSC) as running buffer (see Figure 3.24 - A). MCH, diluted in water, was injected twice (yellow shaded) with a washing step in between (running buffer). As expected, during both injections a decrease of the signal was visible because the refractive index was changed from 5xSSC to water. The shift induced by MCH adsorption is determined by the change of the baseline from before to after the injection; plotted in Figure 3.24 - B. The first injection induced a

shift of 0.13 nm and the second 0.035 nm. The low shift at the second injection implies that the nanoparticles are fully saturated by MCH after the first injection. Therefore, it is obvious that one injection of MCH is enough.

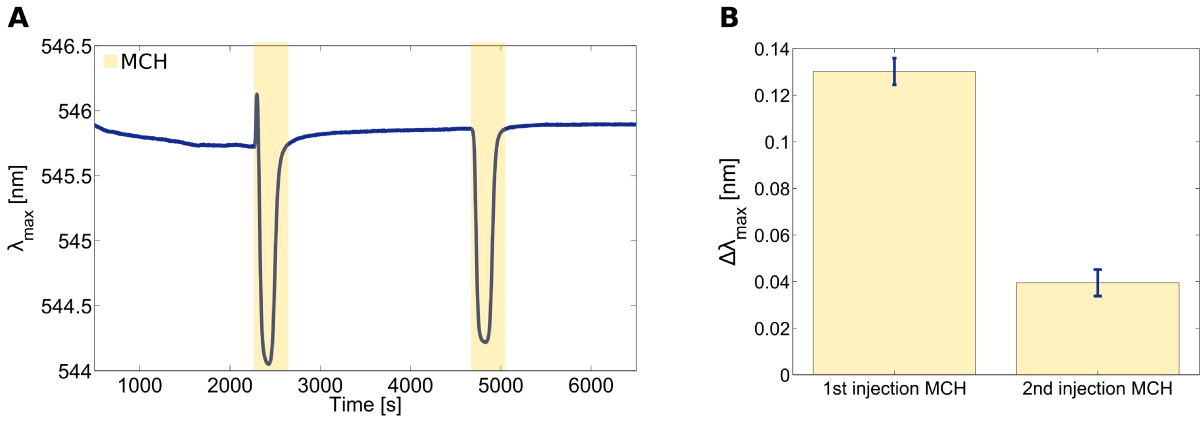

Figure 3.24: A - Adsorption of mercaptohexanol (MCH) on plasma treated 80 nm gold nanoparticle layer. 5xSSC was used as running buffer and the injection was carried out two times. B - Spectral changes compared to the baseline before injection of MCH. The error bars represent the average signal noise.

Afterwards MCH adsorption was included into the measurement of the DNA on the nanoparticles. As described in the chapter before, the nanoparticles were biofunctionalized with thiol-modified capture DNA and afterwards the running buffer was changed to hybridization buffer (5xSSC). As shown in Figure 3.25 - A, 1 μM of the target DNA was injected into the chamber (red shaded), resulting in a slight signal change of 0.12 nm. The subsequent injection of MCH (yellow shaded) showed initially a decrease in signal, which is comparable to the refractive index change in the measurement before. But then the signal increased and decreased with a final stabilization during injection of running buffer. In total a change of 0.14 nm was induced by MCH. An additional injection of target DNA led to a 10 times higher shift of 1.2 nm. This representative experiment shows that MCH plays a major role in the accessibility of the capture DNA for hybridization of the target DNA.

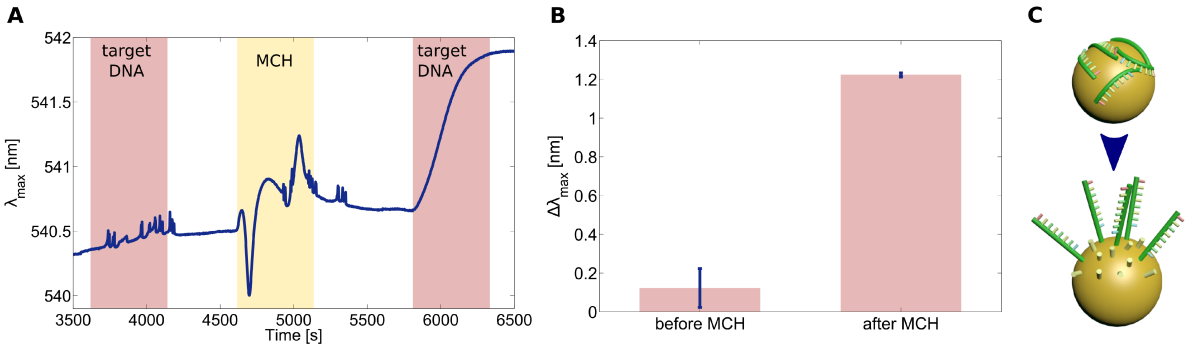

Figure 3.25: A - Kinetics of DNA hybridization before and after coadsorption of MCH on gold 80 nm nanoparticle layer. B - Spectral change induced by hybridization with and without prior MCH coadsorption from the result on the left hand side. C - Schematic of the effect of coadsorption with MCH (short yellow strands) on the adsorbed DNA.

3.4.2.3 Detection of target DNA

Effect of different target DNA concentrations

Different target DNA concentrations were infused during one measurement to determine the sensitivity of the used system. Successive injection of 100 nM target DNA showed a minimal shift (Table 5) and a slow hybridization kinetic (Figure 3.26). In comparison, the 1 μM target DNA showed a fast hybridization kinetics (within 5 min) and a stable signal/plateau. The slow kinetics of the low concentrations did not show such a plateau. It can be assumed if the injection was prolonged, the same plateau would have been reached as with higher concentration.

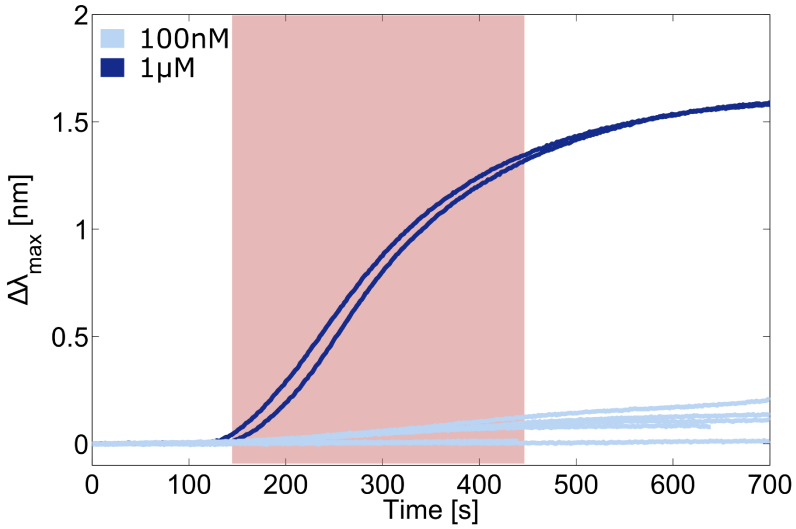

Figure 3.26: Sensitivity determination by injection of DNA with different concentrations (100 nM - 1 μM).

DNA concentration	$\Delta\lambda_{max}$	Number of measurements
100 nM	0.11 ± 0.07 nm	5
1 μM	1.6 ± 0.01 nm	2

Table 5: Calculated changes of λ_{max} for measurements with different target DNA concentrations.

Specificity determination of target DNA detection

In advance to the injection of target DNA, a non-target DNA sequence was injected to ascertain the binding specificity (Figure 3.27). The non-target DNA (sequence Leg4c) induces no shift of the spectral maximum, hence no DNA hybridization occurs. In comparison, the target DNA leads to a shift of 1.8 nm. The representative experiment shows that the ideal

result of no binding event was achieved. But this was not the case for all measurements, the maximal shift with non-target DNA was a third from the shift with target DNA.

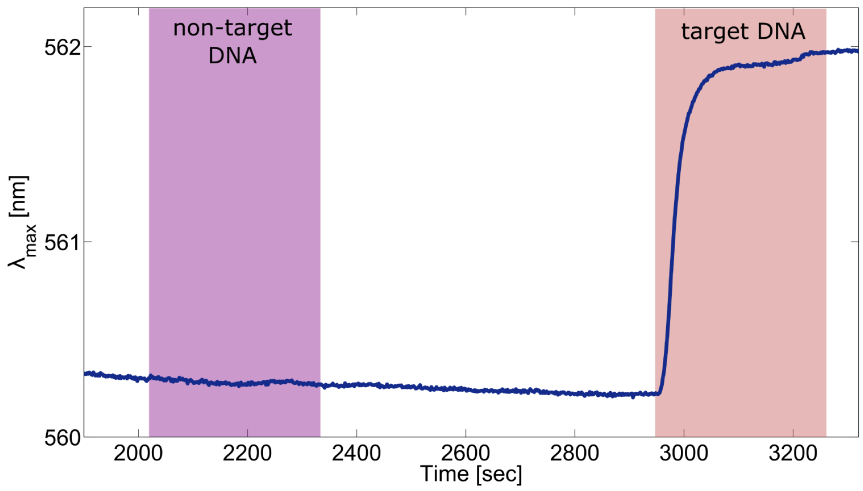

Figure 3.27: Specificity determination by injection of 1μM non-target DNA (Leg4c) and target DNA (Asper2c).

Influence of plasma cleaning on hybridization efficiency

In chapter 3.4.2.1, the results of the effect of plasma etching on adsorption of the capture DNA were shown. A clear difference between the shifts is observable during subsequent hybridization (Figure 3.28). The signal change for hybridization on plasma cleaned substrates is 5 times or even 10 times higher (Table 6). Even though the shifts with the non-cleaned nanoparticles is lower, a shift is observable too. All measurements were performed with the same DNA sequence (Asper2c_T5 and Asper2c) and MCH was coadsorbed before hybridization.

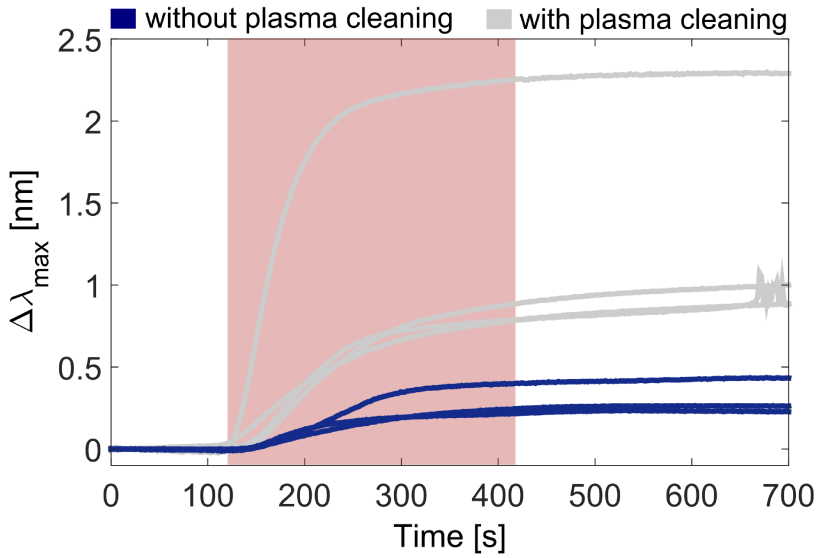

Figure 3.28: DNA hybridization after adsorption of thiol-modified DNA on gold 80 nm nanoparticles from section 3.4.2.1. The transducers were cleaned by plasma etching (grey) or not cleaned (blue). For all experiments Aspergillus DNA and 5xSSC were used.

	$\Delta\lambda_{max}$	Number of measurements
No Plasma treatment	0.31 ± 0.1 nm	3
With plasma treatment	0.91 ± 0.1 nm	3

Table 6: Calculated changes of λ_{max} for measurements with and without plasma treatment.

Effect of different DNA sequences and spacer lengths on hybridization

Different capture DNA sequences with different spacer lengths were adsorbed on the nanoparticles and detected in chapter 3.4.2.1. In all measurements MCH was subsequently adsorbed for DNA erection and the binding of the complementary target DNA to the capture DNA was detected online. In Figure 3.29 the sensograms show that all sequences led to a distinct shift up to 2 nm (Table 7). The final reached plateau varies for the different measurements and the different DNA sequences. The results from the DNA sequence with a ten thymine spacer (see Figure 3.29 - B) showed a higher consistency. Especially the Legionella DNA sequence gives a high variety of reached shifts (Figure 3.29 - C).

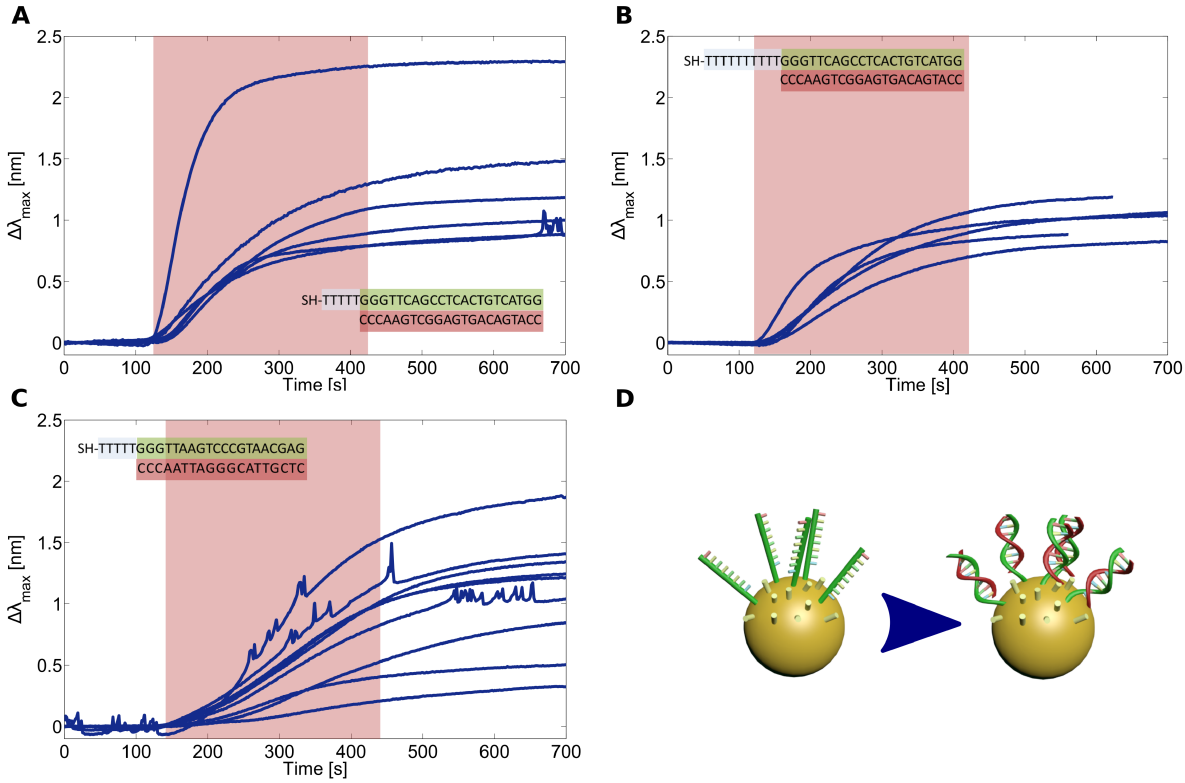

Figure 3.29: Hybridization of target DNA to the different sequences as in section 3.4.2.1. Hybridization of the Aspergillus target DNA (A) and hybridization of Legionella target DNA (B). Further the hybridization to the DNA with different spacer lengths are separated: 5 thymines (A) and 10 thymines (B). D - Schematic of the hybridization on nanoparticles.

DNA sequence	$\Delta\lambda_{max}$	Number of measurements
Asper2_T5	1.30 ± 0.56 nm	6
Asper2_T10	1.00 ± 0.15 nm	5
Leg5_T5	0.96 ± 0.51 nm	11

Table 7: Calculated changes of λ_{max} for measurements with different DNA sequences and spacer lengths.

Hybridization to capture DNA with poly(A) tail

In chapter 3.4.2.1, DNA with a poly(A) tail instead of thiol-modification was adsorbed on the nanoparticle surface. The sensograms of the adsorption in Figure 3.23 showed promising results for the hybridization. However, in Figure 3.30 the sensograms are shown from the two sequences Aspergillus (Figure 3.30 - A) and Legionella (Figure 3.30 - B) with their different poly(A) tails and spacers. It is clearly visible that no hybridization was detectable with both DNA sequences. The Aspergillus DNA led to a higher signal response (Table 8), but

in comparison to the results with thiol-modified DNA, the hybridization is significant lower.

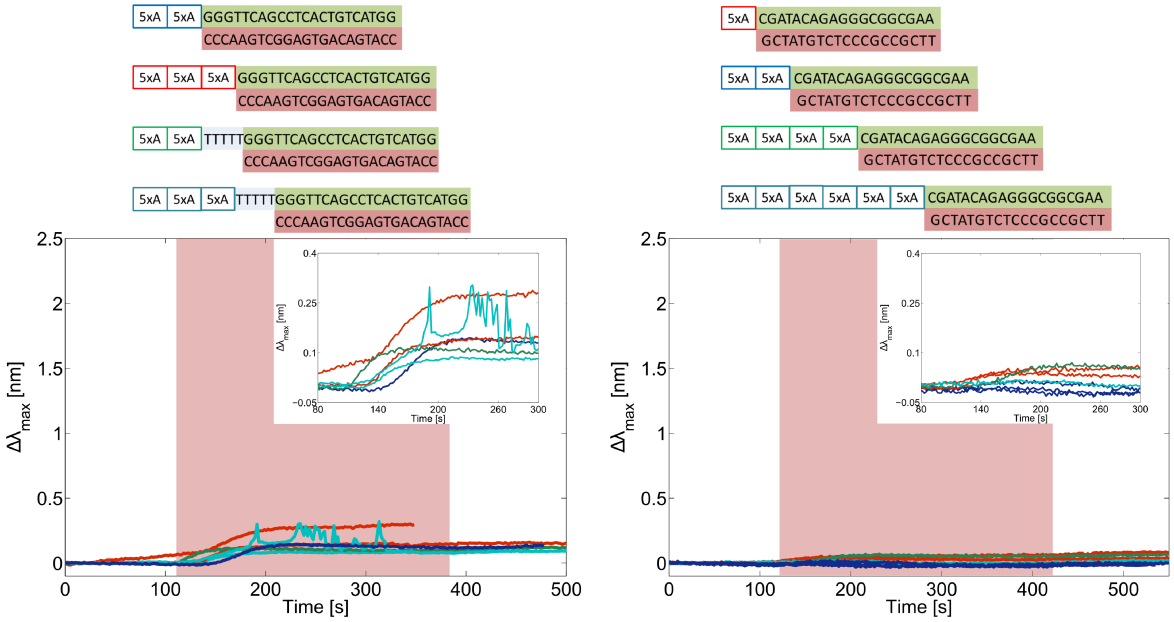

Figure 3.30: Hybridization of target DNA to the DNA with varying poly(A) tails instead of thiol-modification. The DNA sequences are specified above (A - Aspergillus sequence, B - Legionella sequence). Inset shows a zoom-in of the sensograms.

DNA sequence	Number of adenines	Number of thymines	$\Delta\lambda_{max}$	Number of measurements
Asper2	10		0.13 nm	1
Asper2	15		0.13 ± 0.18 nm	3
Asper2	10	5	0.12 nm	1
Asper2	15	5	0.08 ± 0.01 nm	2
Leg4	5		0.05 ± 0.03 nm	2
Leg4	10		-0.01 ± 0.01 nm	3
Leg4	20		0.06 nm	1
Leg4	30		0.01 nm	1

Table 8: Calculated changes of λ_{max} for measurements with different DNA sequences and poly(A) tails.

3.4.2.4 Regeneration of sensor after hybridization

For a multiple use of the biosensor the target DNA has to be denaturated and repeatedly hybridized. NaOH was chosen as denaturation solution. The 1 M NaOH solution was injected with a higher flow rate of $100\mu l/min$ to have an exposure time of 1 min to the nanoparticles and the DNA. This guarantees that the solution has only an effect on the DNA and not to the nanoparticles, e.g. desorption of the nanoparticles. In Figure 3.31 one representative measurement is shown, where the target DNA was hybridized for several times after

denaturation with NaOH. The full DNA hybridization was proven by injection of additional target DNA after the first injection (dashed line). It can be clearly seen that with the first injection a full saturation is reached and no additional DNA can be hybridized. The variance of the signal cannot be related to the number of denaturations/hybridizations. The shifts are comparable to the results of DNA hybridization in chapter 3.4.2.3. The sensogram of the whole measurement is shown in appendix (Figure 6.3).

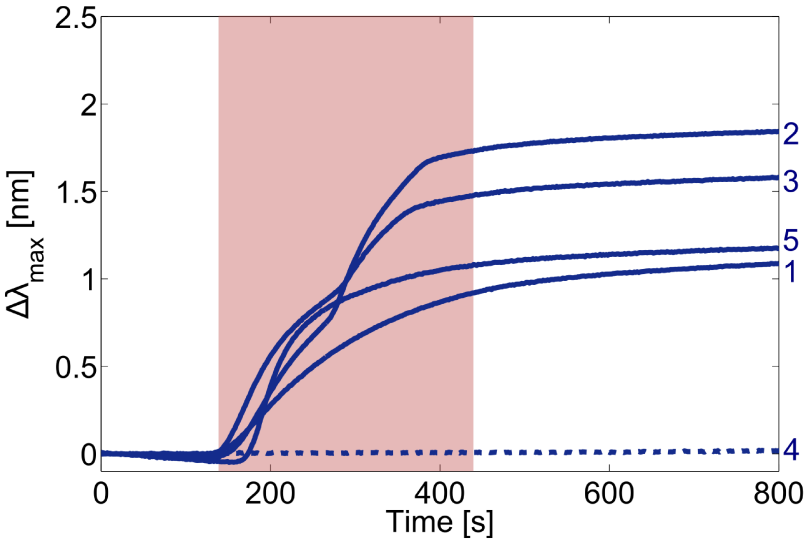

Figure 3.31: Sensogram of target DNA hybridization after regeneration of one LSPR spot with 1 M NaOH for four times (order numbered). The dashed line depicts an additional hybridization of target DNA for saturation control.

3.4.2.5 Detection of real target DNA samples

In medical diagnostic usually DNA fragments amplified by PCR want to be detected. For that reason, the detection of a PCR product was investigated with the LSPR. The system was tested with synthetic target DNA, and after regeneration with NaOH the Legionella PCR Product (262 nucleotides) was infused. As seen in Figure 3.32, a signal change was induced with the PCR product, but the kinetic behavior differed from the observed hybridization in section 3.4.2.3. The sensogram of the whole measurement is shown in appendix (Figure 6.4). The signal did not reach a plateau as usual, it decreased after the change to hybridization buffer and the subsequent hybridization of the synthetic DNA led to an additional spectral shift similar to the other spectral shifts. This indicates that the hybridization is not carried out properly, which my be attributed to the length difference of the DNA sequences. For comparison to the DNA hybridization with synthetic target DNA, the flow rate was kept

constant ($20\,\mu l/min$). In another measurement the flow rate was decreased to $5\,\mu l/min$, but no increase at the spectral shift was detectable. In general, detection of the PCR product was possible but not the same shift was achieved as with the synthetic DNA strand.

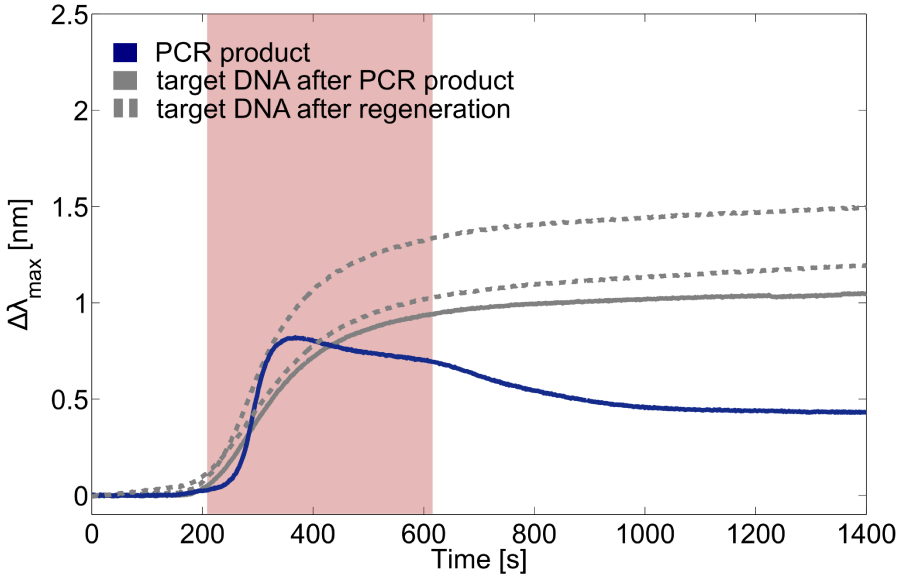

Figure 3.32: Hybridization of PCR Product (blue) and synthetic target DNA (grey) to thiol-modified DNA on gold 80 nm nanoparticle layer. The synthetic target DNA was hybridized after regeneration with 1 M NaOH (dashed grey line). Additionally, synthetic target DNA was injected directly after the PCR Product hybridization (grey line).

3.4.3 Detection of hemin with G-quadruplex

As mentioned in section 1.2.3, DNA can form G-quadruplex and bind hemin to form a DNAzyme with catalytic activity. Studies were carried out if DNAzymes and the binding of hemin can be detected in real-time with the LSPR system. PS2.M sequence with thiol-modification at the 5' end was injected into the microfluidic chamber, as observable in the sensogram in Figure 3.33. The DNA adsorbed on the nanoparticle surface and showed the same kinetic behavior as the other DNA sequences in section 3.4.2.1. Afterwards, the buffer change from citrate buffer pH = 3.0 to Tris-Buffer led to the G-quadruplex formation. The change of λ_{max} is induced by the different refractive indices of the buffer solutions.

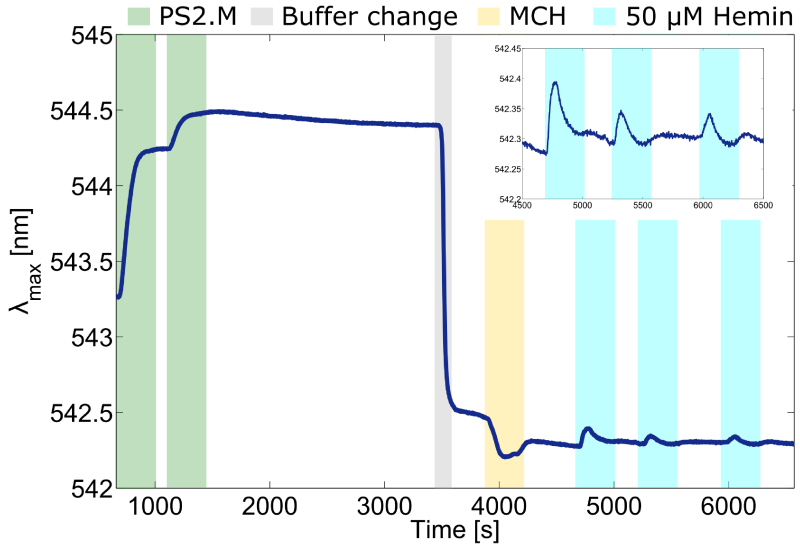

Figure 3.33: The figure can be divided into four sections: Adsorption of thiol-modified PS2.M DNA sequence on gold 80 nm nanoparticle, buffer change for G-quadruplex forming of the DNA, coadsorption of Mercaptohexanol (MCH) for passivation and erection of the DNA and injection of 50 μM hemin for several times (highlighted in the insert).

Afterwards, MCH was infused for coadsorption, erection of the DNA and passivation of the nanoparticle surface. Three times in a row 50 μM hemin was injected at the same flow rate (20 $\mu l/min$). For each injection a spectral shift is observable, as highlighted in the insert of Figure 3.33. But only after the first injection λ_{max} the baseline is raised by 0.05 nm.

For verification if hemin binds to the G-quadruplex, experiments were performed without immobilization of the G-quadruplex. As shown in Figure 3.34, 50 μM hemin was injected into the microfluidic chamber. Tris-buffer was used as running buffer, as before. The hemin induced a spectral shift of 0.1 nm. Afterwards MCH was injected and the level of λ_{max} decreased nearly to the same level as before the hemin injection. Anew 50 μM hemin was injected twice, but a lower shift than before was detected.

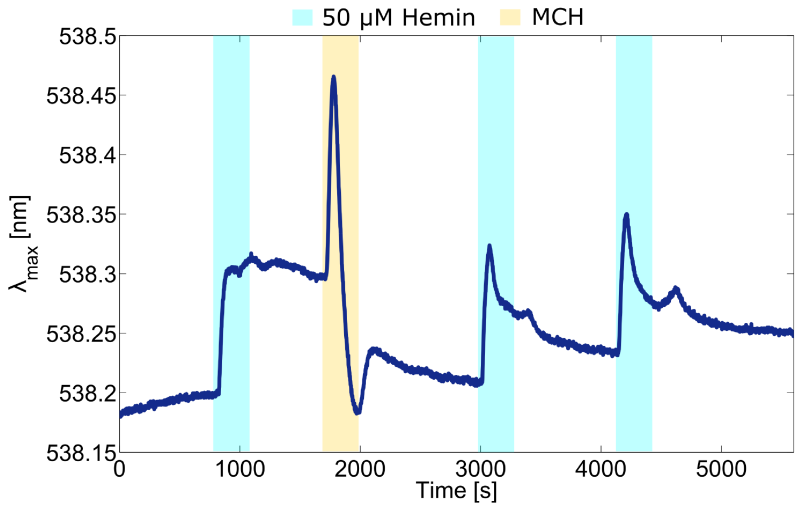

Figure 3.34: Detection of 50 μM hemin without previous G-quadruplex DNA adsorption on nanoparticle layer. For similar surface properties as with DNA the surface was passivated with Mercaptohexanol (MCH) and afterwards 50 μM hemin was injected again.

4 Discussion

4.1 Comparison of SPR, LSPR and sLSPR

Characterization of investigated transducers

Glass chips with densely immobilized nanoparticles with different shapes (spherical, nanopeanuts and nanoprisms) were prepared. All nanostructures were successfully adsorbed on the glass chip over an area of $\sim 0.25\,cm^2$. The AFM images show a rather homogeneous nanoparticle distribution with rare nanoparticle aggregations. The height of the nanoparticles correspond to the given diameters and is relatively uniform for all structures. The surface concentration of the nanostructures is increasing with decreasing nanoparticle size. Larger nanoparticles have a higher total charge on their surface leading to stronger repulsion between the nanoparticles and causing larger spaces between the immobilized nanostructures. This assumption is confirmed by the AFM images of 60 nm spherical nanoparticles and nanopeanuts with a length of 60 nm. The immobilized nanostructures showed a comparable density. The lowest surface density was measured for silver nanoprisms with gold edges caused by lower concentrations in solution.

Measurement of bulk refractive index

Solutions with different refractive indices were utilized to determine the bulk sensitivity S_b of the investigated nanoparticles. The bulk sensitivity for spherical nanoparticles changes with size. An increase in size leads to a higher sensitivity. This is in agreement with theoretical results in literature [82]. Nanostructures with higher aspect ratios or sharp edges are well known for their increased sensitivity compared to spherical nanoparticles. Therefore, nanopeanuts with a similar shape to nanorods and nanoprisms were investigated.

Two plasmon modes were induced and detected with the nanopeanuts. The detected spectra were comparable to nanorods with two peak maxima.[90] The resulting bulk sensitivities for the nanopeanuts differed with their plasmon mode. The transverse mode (y-polarization) showed a higher bulk sensitivity because of the confined field on the tip of the nanopeanuts.

The spectrum of the silver nanoprisms were detectable, even though the AFM image confirmed a low surface concentration. In comparison to the other nanostructures, the nanoprisms showed the highest sensitivity to bulk refractive index changes. As described in literature, so-called hot spots (confined electromagnetic fields at the tips of the nanoprisms) result in an increased sensitivity to dielectric changes. [91, 92] The bulk sensitivity confirms the high potential for nanoprisms as transducers as described already in literature [87, 93].

The bulk sensitivity measurements on single nanoparticle level were the initial performance tests of the microfluidic system integrated into the microscopy set-up. The advantage of sLSPR is the localization of the detection volume on a single nanoparticle; the nanoparticles at the LSPR setup are excited everywhere on the substrate. The online detection of the bulk refractive index change was successful, spectral changes with each solution were clearly visible. The calculated bulk sensitivity was lower compared to the measurements with 80 nm spherical nanoparticles layer (LSPR). The difference originate from the fact that the measured nanoparticle geometry at sLSPR can deviate from the average size of the nanoparticles measured with LSPR. During sLSPR measurements the maximal signal change was not accurately defined as with LSPR. Even though the flow was stopped after the injection, the signal increased. It indicates that the solution is still moving and the refractive index is changing until it reaches the final value. This can be explained by the high viscosity of the solution, compared to water, which leads to a slower diffusion in the chamber.

The bulk refractive index measurements were realized for all nanostructures and even on a single nanoparticle. The calculated bulk sensitivities are comparable to results from literature and confirm that oblonged nanostructures or nanostructures with hot spots are more sensitive to dielectric changes.

Measurement of thin polyelectrolyte layers

Thin molecular layer adsorption was chosen to mimic the adsorption of biomolecules on the nanostructure surface. PEL are charged polymers forming a monomolecular layer with a defined and constant thickness in the lower nm range. [94] By LbL technique PEL layers with different opposite charges were alternately adsorbed from solution to the gold layer (SPR) and nanostructures (LSPR and sLSPR) except nanoprisms. Even though the silver nanoprisms were coated with gold on the edges to prevent a reshaping, the salt concentration of the running buffer induced a degradation. The subsequent PEL adsorption was not feasible.

The sensogram of LSPR and SPR demonstrate the adsorption of each PEL layer and the self-termination of PEL adsorption. The curve of the first layer differs from the other layers. This may come from an inhomogeneous adsorption of the polyelectrolyte molecules on to the gold surface. An adsorption up to twenty subsequent PEL layers was detectable with the LSPR and the SPR system. The total signal response was different for each layer caused by different layer thickness as shown by Caruso et al. [95]. PSS has a higher layer thickness compared to PAH and causes a higher signal change. Hence, thickness differences in nm range were traceable. At the LSPR system the dependence on the number of deposited

PEL layers is non-linear with an asymptotic value of 200 000 μRIU for all nanostructures. The SPR system results followed a linear behavior as expected from the calculations. The maximum values of Δn_{eff} were reached faster with smaller nanoparticles. These results are similar to the calculated data and confirm that the E-field is maximal on the nanostructure surface and decays into the dielectric bulk. Further, the resulting Δn_{eff} approve that the decay depends on the radius of the nanoparticle and the order of mode. The penetration depth for 30 nm and 80 nm spherical nanoparticles is calculated to ~ 9 nm and ~ 19 nm. Beyond the penetration depth changes on the surface are not detected anymore. Hence, the adsorption of the polyelectrolyte layers was only detectable until 9 and 19 nm. After 6 and 20 PEL layers no further increase in signal was detectable with 30 nm and 80 nm nanoparticles. Consequently, the estimated thickness for each PEL layer is 1 to 3 nm.

On a 80 nm single nanoparticle (sLSPR) twelve PEL layers were adsorbed and detected in real-time. The signal change Δn_{eff} is comparable to the LSPR result with 80 nm nanoparticles, but the rate of the signal change is different. The local adsorption at the single nanoparticle is not identical with the average adsorption on nanoparticle layer, and, as mentioned before, the nanoparticle geometry can deviate from the average size.

From the peak position variation over time the lowest detectable Δn_{eff} was determined to be better than 100 μRIU for the LSPR system and 1 000 μRIU for the sLSPR system. However, the SPR system gave the lowest detectable Δn_{eff} around 1 μRIU. This comparison shows that the SPR system is better in the determination of the bulk refractive index. These values for n_{eff} precision is influenced by the physical principles and the instrumentation, which is well established in the SPR system. Especially the collection of the optical signal with the sLSPR setup is very sensitive to small mechanical movement/vibrations occurring during the measurement.

Apparently, the stronger E-field confinement is no advantage for the bulk refractive index measurements. However, its advantage is present for measurements in thin films. The strongest surface sensitivity (S_s) was achieved by the LSPR system with 30 nm nanoparticles and the first layers. Δn_{eff} of the first 2 PEL layers was 40 times higher compared to the values of the SPR system (Δn_{eff} (LSPR - 30) = ~ 86 000 μRIU; Δn_{eff} (SPR) = ~ 2 090 μRIU). The 80 nm nanoparticles showed a 6 times higher change of n_{eff} compared to the SPR system (Δn_{eff} (LSPR - 80) = ~ 30 000 μRIU). This signal improvement confirms that the surface sensitivity of nanostructures is higher compared to the SPR system. However, the dynamic range of the layer thickness detection is reduced. The nanoparticle size has to be chosen depending on the size of the target biomolecules and the type of application (molecule detection or detection of molecule's conformational changes).

4.2 Biomolecule detection

4.2.1 Measurement of protein multilayers

Multilayers can be formed with the protein bovine serum albumin (BSA) and the glucan dextrane sulfate (DS). The alternate adsorption is similar to the LbL technique with PEL. Assuming that the dimension of BSA are 5.5 x 5.5 x 9 nm [96] and DS is a flat glucan chain with less than 1 nm, then the maximal number of BSA/DS bilayers would be 5 because of the penetration depth of 80 nm spherical nanoparticles. The thickness difference of the two layers was observable in the signal changes. Comparable to the results with the PEL layer, a linear behavior was detected with the SPR system and a non-linear behavior with the LSPR system. The maximum values of Δn_{eff} were approximately reached at 6 bilayers of BSA/DS. This result confirms that up to 20 nm dielectric changes in the nanoparticle environment can be detected and that nanoparticles are more sensitive compared to the SPR system.

The detection of four BSA/DS multilayers was achieved on a single 80 nm spherical nanoparticle. The shifts were comparable to the results with the LSPR, but at 4 bilayers already the asymptotic value was reached. As mentioned before the geometry of the single nanoparticle may differ compared to the average nanoparticle geometry. The data show again that the sLSPR system is very sensitive to mechanical movement/vibrations occurring during the measurement. Thus, the sLSPR is inapplicable for DNA detection due to the low signal-to-noise ratio.

4.2.2 DNA immobilization and hybridization

The promising results with the LSPR with 80 nm nanoparticles gave the opportunity to use this setup as DNA biosensor with the aim to detect the hybridization of the target DNA to the adsorbed single-stranded capture DNA. As capture DNA a short DNA strand with a length of 19 or 22 bases was applied, which corresponds to a length of around 7 nm [97]. The PEL measurements and the protein multilayers confirmed that with 80 nm nanoparticles it is possible to detect a change up to 20 nm in the surrounding of the nanoparticles due to the penetration depth l_d of ~ 19 nm. The DNA is in close proximity to the nanoparticle surface during adsorption and hybridization and should lead to a shift of the nanoparticle spectrum. Different strategies were pursued to succeed in detecting DNA hybridization in real-time.

Effect of different buffers on covalent DNA adsorption

Two different buffers were investigated for covalent adsorption of capture DNA. Herne et al. [62] showed that thiol-modified DNA can be bound to gold films in 1 M KH_2PO_4 pH = 4.4.

This procedure was already applied in the working group for DNA measurements on nanoparticles in dry-state [98]. With KH_2PO_4 as running buffer no stable signal was reached and the kinetic behavior implies a continuous change of the refractive index surrounding the nanoparticles. The signal decrease may come from surface changes of the nanoparticles, e.g. removement or addition of surfactants. The injection of capture DNA led to stable signal and thus implies a passivation of the nanoparticle surface. On one hand these results did not verify an adsorption of the capture DNA and on the other hand a stable signal is needed to determine the signal change induced by capture DNA adsorption. From the measurements with LbL technique similar adsorption kinetics with an increase of signal was expected. Besides, this procedure did not show auspicious results to achieve a fast detection of capture DNA adsorption. Unlike former measurements, where capture DNA was exposed to the nanoparticles for several hours, here the adsorption should be carried out in several minutes.

Zhang et al. [52] published that fast adsorption is possible with a pH 3.0 citrate buffer. Their measurements were carried out in nanoparticle solution and indicated that thiol-modified DNA can be adsorbed on the gold surface within a few minutes. The presented results confirm that the same method can be adopted to nanoparticles immobilized on a surface. The signal was stable compared to the measurements with KH_2PO_4 buffer. This may come from the stabilization of the nanoparticles by citrate. The following adsorption of the DNA showed similar binding kinetics as with polyelectrolytes or proteins and within 5 min a stable signal was reached once again. The second injection verified that the nanoparticle surfaces were almost saturated with DNA and one injection is completely sufficient. The results show clearly that the citrate buffer with a low pH is the preferable buffer for the adsorption of the capture DNA.

Effect of different DNA concentrations on immobilization

Different capture DNA concentrations were injected to study if a fully saturation can be achieved with less amount of DNA. The injection 10 nM DNA showed a slight decrease of the signal. For explanation of this phenomenon instead DNA solution buffer with water instead of DNA was injected via the probe loop. The same decrease was detectable as with 10 nM DNA and shows that the change comes from a minimal refractive index change. 100 nM DNA induced an increase in signal, but 25 times less than the signal induced by 1 μM DNA. The results show that a full saturation within 5 min cannot be achieved with low DNA concentrations.

Effect of plasma etching on DNA immobilization and hybridization

The investigated nanoparticles were purchased and the company does not give information on the supplementaries for stabilization of the nanoparticles in solution. Although the nanoparticles were rinsed with water and dried under nitrogen stream, it cannot be assured that no residuals were left on the nanoparticle surface. To ascertain if the substrates have to be cleaned before biofunctionalization, measurements were performed with and without additional plasma etching.

The comparison of the induced shifts by capture DNA adsorption did not show a distinct difference. In both cases the DNA adsorbed on the surface. Only the kinetic differed at the measurements with plasma cleaning in advance. A increase and decrease was observable at the beginning. This can be explained by the DNA adsorption process consisting of the physical adsorption and the slower chemical bonding. The decrease may originate from DNA strands which did not adsorb properly on the nanoparticle surface and are removed during chemical adsorption and erection of the other DNA strands. [89, 50]

The subsequent hybridization disclose that plasma cleaning is necessary to achieve higher hybridization efficiencies. With plasma cleaning the shifts were 3 times higher compared to the substrates without plasma cleaning. It can be assumed that the surface of the nanoparticles is still covered with residuals and stabilization factors from storage solution. Therefore, the thiol-modified DNA cannot bind properly to the nanoparticle surface.

At the non-cleaned substrates, the coadsorption of MCH did not induce a shift of the spectral maximum, which emphasizes that there are no free binding sights on the nanoparticle surface and the DNA cannot be erected or does not have to be erected. The low spectral maximum shift with the target DNA supports the assumption that a low number of capture DNA strands are adsorbed on the surface.

The substrates were also investigated in dry state. Spectra were taken before and after plasma cleaning and a shift to lower wavelengths were clearly visible. This implies that something is removed from the nanoparticle surface. A high purity of the substrates is crucial to adsorb the capture DNA on the nanoparticle surface and reach accordingly a high hybridization efficiency.

Effect of coadsorption with MCH on hybridization

Herne and Tarlov [62] asserted that the accessibility of the capture DNA for the target DNA can be enhanced by coadsorption of a small blocking molecule, mercaptohexanol. As described by Sandström et al. [99] single-stranded DNA molecules can bind nonspecifically to the nanoparticle surface despite their negative charge. The additional treatment of the

substrate with MCH should result in a displacement of the nonspecifically bound ssDNA and blocks free binding sites on the surface. To assure that the same process occurs also on the nanoparticles, MCH was applied after biofunctionalization of the nanoparticles with capture DNA.

The measurements on nanoparticles without adsorbed DNA showed that MCH is adsorbed on the nanoparticles and after one injection the nanoparticles are almost saturated. A big signal change was observable due to the refractive index change from 5xSSC (running buffer during hybridization) to water. 5xSSC was applied to compare the kinetic behavior to the results with DNA. The measurements with DNA were carried out after capture DNA immobilization and change to 5xSSC.

The injection of the target DNA before MCH induced a 10 times lower shift compared to the results after coadsorption of MCH. This supports the assumption that thiol-modified DNA lies down on the gold surface due to nonspecific adsorption and are raised off the surface by addition of MCH. The desorption of the DNA is visible in the kinetic during MCH adsorption. The signal decrease is induced by the local refractive index change of the solution, but the rise comes from the capture DNA movement. The repeated injection of the target DNA shows clearly that the capture DNA is now accessible for hybridization.

The results approve that coadsorption of MCH is needed to increase the availability of the capture DNA and that the method can be implied under continuous flow. It was even possible to adsorb MCH and raise the capture DNA within 1 min.

Investigation of different DNA sequences and spacer lengths

Two different DNA sequences and spacer lengths were investigated to determine their influence on DNA adsorption on the nanoparticle surface and on hybridization efficiency. The immobilization for both DNA sequences and spacer lengths resulted in an average spectral shift of 1 nm but with a high divergency. No correlation was traceable for the signal differences. The injection with capture DNA was repeated at the measurements with 10 thymine spacer. If a high shift was detected at the first injection no shift was detected during repetition. If a low shift was injected in advance the same total shift was detected again at the repetition. Hence, shifts of 1 nm and more are caused by fully saturation of the nanoparticles with capture DNA. In all three cases some adsorption sensograms show a decrease of the spectral maximum and a subsequent increase. As already explained in the section before, this may come from the two adsorption steps of thiol-DNA to gold surfaces.

For both DNA sequences and spacer lengths a spectral change was detectable caused by hybridization. The results from the DNA sequence with a ten thymine spacer showed a higher

consistency. This can be explained by a higher accessibility of the capture DNA for the target DNA. The short spacer leads to a decreased distance between the DNA strands. Therefore, an interaction between the capture DNA strands is more likely. Again the total spectral shifts resulted in a high divergency. The previous capture DNA adsorption was considered as possible factor. A low spectral shift with the capture DNA may lead to a low shift with the target DNA because less DNA was adsorbed on the surface, or the other way around leads to a higher shift because the DNA distance is increased and more accessible. The hybridization results were compared to the shifts at the adsorption but no correlation was found. The results from the measurements without cleaning of the nanoparticles with plasma etching showed a low spectral shift comparable to the lowest results with the Legionella DNA sequence. Hence, low shifts may come from not properly cleaned nanoparticle surfaces, even though the same protocol was used for all measurements.

Furthermore it has to be considered that the measurements were carried out at room temperature. The chance of unspecific binding increases between the DNA strands at low temperature. The capture DNA strands and target DNA strands can bind unspecifically among each other leading to a decreased accessibility for specific hybridization.

The binding of complementary target DNA was detected with both DNA sequences and spacer lengths within 5 min. The inconsistencies require additional investigations. An increased accessibility of the capture DNA was not achieved with longer spacer length.

Specificity test by hybridization of non-target DNA

The detected binding specificity was verified by injection of a sequence non-complementary to the capture DNA. The representative example showed no spectral shift, hence no binding of the non-target DNA to the capture DNA. At additional measurements a shift was detectable, but the signal change was maximal a third from the shift with target DNA.

The non-target DNA binding was clearly distinguishable from the binding of the target DNA. Therefore, the presented sensor shows a high specificity for the target DNA, even though the detection temperature is at room temperature.

Effect of different DNA concentrations on hybridization

The concentration of 1 μM DNA was set as default for all measurements. A lower concentration of 100 nM target DNA solution was investigated to study if lower concentrations are detectable. A slight signal increase was observable with each injection of the 100 nM DNA. The spectral shift was 14 times less compared to the shifts with 1 μM DNA. For comparability the flow rate was kept the same during all injections. If less DNA is present in solution

the DNA strands need more time to reach the nanoparticle surfaces. It can be assumed that with an elongation of the injection time the same plateau would have been reached as with higher concentration. Hence, the diffusion rate has to be considered at measurements with low concentrations. The distinct signal change with 1 μM DNA verified that the capture DNA was available for hybridization.

Hybridization of PCR product

One application field for biosensors is the detection of pathogens. Pathogens are present in solution at very low concentrations. Therefore the pathogen DNA is amplified by PCR. The final DNA fragments or PCR products consisted of 262 nucleotides, 10 times more compared to the synthetic target DNA. With longer DNA the chance of secondary structures is more likely and causes less effective or no hybridization to the capture DNA. Even though the DNA was heated and cooled down before measurement, it cannot be excluded that the DNA builds secondary structures in the tube on the way from the injection valve to the microfluidic chamber (approx. 2 min). For comparison, the flow rate was kept constant ($20 \mu l/min$), which may result in too fast flow for longer DNA to hybridize. In another measurement the flow rate was decreased to $5 \mu l/min$, but no increase at the spectral shift was detectable. In general, detection of the PCR product was possible but not the same shift was achieved as with synthetic DNA strands.

Regeneration of transducer

The ability to regenerate the sensor surface gives the opportunity to reuse the biosensor for several measurements. The transducers do not have to be replaced between every use. This is highly desirable because it reduces costs and improves the repeatability of the measurements. The regeneration technique has to be adapted to the interaction between the recognition element and the target element and depends on the binding strength.

Nucleic acid denaturants can be physical (e.g. thermal denaturation) or chemical (e.g. chemical agents). Heating is the most frequent method for DNA denaturation, but bears disadvantages for measurements with a microfluidic device. The solution heating in the chamber increase the probability for bubble format and the denaturation process is slower compared to chemical denaturation. For a rapid denaturation and renaturation of the DNA chemical denaturation agents provide an ideal alternative to physical denaturation. Studies [100] showed that alkaline agents such as NaOH can denaturate DNA and a renaturation can be repeated after the change to hybridization buffer. In case of NaOH the DNA is denaturated by the increase of the pH. The hydrogen bonds between the two DNA strands

are broken because the hydrogen-bonds contributing protons from guanine and thymine are removed.

The displacement of the target DNA was studied by injection of 1 M NaOH within 1 min. The flow rate was increased to $100\,\mu l/min$ to minimize the exposure time. The regeneration of the sensor was tested at all hybridization measurements and comparable results achieved. The representative example showed that even an increased signal was detectable at the second and third injection after DNA denaturation. This may have two reasons: nonspecific bindings were denaturated or the capture DNA was more accessible because the DNA strands were separated. Zhang et al. [101] claimed that ssDNA strands are fully deprotonated at high pH 8.5 and the separation between the strands increases because of electrostatic repulsion forces.

The substrates were fully saturated by target DNA because no signal change was observable during additional injection of target DNA. The target DNA was successfully displaced by changing of the pH. The environmental changes did not have an impact to the capture DNA and the immobilized nanoparticles. On the contrary, the results emphasized that the capture DNA was more accessible for hybridization after denaturation.

Investigation of direct adsorption with poly(A) tails

The direct adsorption of the recognition element instead of self-assembled monolayers can result in the immobilization of large quantities with definable packing densities as claimed by Pei et al. [56]. The DNA base with the highest affinity to gold is adenine. Therefore the immobilization of two different DNA sequences with poly(A) tails in various lengths were investigated. To increase the availability of the ssDNA for hybridization additional spacers with thymine were added. At the immobilization all sequences induced a shift, but it was not possible to determine a trend or graduation that longer/shorter DNA sequences or poly(A) tails lead to an increased/decreased shift. The binding kinetics and the resulted shifts are comparable to the results with DNA adsorbed covalently to gold. Also the fast adsorption with citrate buffer pH = 3.0 was realized as described in literature [56].

However, the subsequent DNA hybridization did not result in a spectral maximum change, even though the reliable DNA hybridization is described by Pei et al. [56] with nanoparticles in solution. The direct adsorption is based on a weak attachment of the DNA bases to the nanoparticle surface by van der Waals and electrostatic forces. In contrast to the results in literature, the nanoparticles were immobilized on a surface and implemented in a microfluidic chamber. Hence, the flow of the solution has an impact on the ssDNA. The results may conclude that the DNA strands did not adsorb properly to the nanoparticle or

did not withstand the pressure by the flow and were washed away during the change to the hybridization buffer. This assumption was confirmed by additional infusion of capture DNA in citrate buffer after hybridization. Again a spectral maximum change was reached as before hybridization. If MCH was coadsorbed after hybridization no shift during capture DNA infusion was detectable because the surface was fully saturated with thiols. This verifies that the capture DNA adsorbs on the surface but with low stability.

Hence, both sequences with the different poly(A) tails were not available for DNA hybridization and the direct adsorption technique was not transferable on immobilized nanoparticles under flow.

4.2.3 Detection of hemin with G-quadruplex

As mentioned in section 1.2.3, DNA can form G-quadruplex and bind hemin to form a DNAzyme with catalytic activity. The catalytic reaction of silver deposition is well known in combination with horseradish peroxidase. [102, 25] Until now the silver deposition reaction was not applied to DNAzymes. It allows the development of new bioassays with surface plasmon resonance or electrochemistry as detection techniques. Especially the application on noble metal nanoparticles is interesting because of their high sensitivity to local refractive index changes. Even small peroxidase activity on the nanoparticle surface could be detected. Hence, first steps were undertaken to combine the LSPR system with DNAzymes.

The results show that with the LSPR system it was not possible to differentiate between the binding of hemin to the G-quadruplex or the adsorption directly to gold. The adsorption of the PS2.M DNA sequence was successful, but it could not be verified if the G-quadruplex formation was present after buffer change. The preliminary results were not distinct therefore no silver deposition was applied.

4.3 Conclusion

The investigated biosensor setups confirmed the potential of nanostructures for bioanalytical applications. The highly localized LSPR sensing volume eliminates the need of additional labeling or adsorbed matrices for signal enhancement as often done with SPR system. Especially the simple LSPR setup showed promising results for a fast, reliable and real-time detection of target analytes for routine point-of-care clinical evaluation or real-time diagnosis of diseases.

5 Summary

Metal nanostructures with their attractive optical properties are of great interest in the field of biosensing. In this thesis, a label-free online detection of biomolecules with immobilized nanoparticles in a microfluidic chamber was realized. Two label-free sensor arrangements based on densely adsorbed (LSPR) and single nanostructures (sLSPR) were combined with a microfluidic system and compared to a commercial available system (SPR). The experimentally determined bulk sensitivities for spherical and anisotropic nanostructures were comparable to the results from literature and confirmed that oblonged nanostructures or nanostructures with hot spots are more sensitive to dielectric changes.

The surface sensitivity of the three sensing systems were investigated by sequential deposition of charged PEL layers and protein multilayers. The measurements confirmed that the LSPR signal has a non-linear dependency on the number of deposited layer in opposite to the SPR system, that the signal change is higher compared to the SPR system and that the signal depends on the size of the nanoparticle and the plasmon mode. Even though the signal noise of the LSPR system was higher compared to the SPR system, the higher surface sensitivity minimizes this disadvantage.

It was also possible to detect the successive adsorption of PEL layers and protein multilayers online on an area smaller than $0.02\,\mu m^2$ on a single 80 nm spherical nanoparticle. However, the signal noise of the sLSPR was substantial larger compared to the other systems, caused by the lower intensity of the detected scattered light from the single nanoparticles and the mechanical instability. The low signal-to-noise ratio showed that the setup is non-applicable for DNA detection.

The real-time detection of DNA-DNA binding was realized on 80 nm spherical gold nanoparticles (LSPR setup) in a microfluidic chamber without labeling. Two DNA sequences were successfully adsorbed covalently on the nanoparticles' surfaces and the subsequent hybridization was traceable within 5 min at room temperature. The additional application of non-target DNA verified the specific binding between the capture and target DNA and the binding process was repeatable by a chemical denaturation agent. Investigations concerning the buffer during biofunctionalization, the pre-treatment of the substrates with plasma and the coadsorption of mercaptohexanol resulted in an enhanced capture DNA adsorption and availability for target DNA hybridization. Although direct adsorption is reported as possible biofunctionalization technique, the hybridization of target DNA to capture DNA with poly(A) tails was not transferable to immobilized nanoparticles (LSPR setup) due to the weak binding forces between the nucleotides and the gold surface.

The DNA sequence forming a G-quadruplex was successfully adsorbed on the nanoparticles, but it could not be verified if the G-quadruplex formation was present after buffer change and if hemin bound to the 3D DNA structure. Further investigations on DNAzymes in combination with immobilized nanoparticles have to be executed.

6 Zusammenfassung

Metallische Nanostrukturen mit ihren einzigartigen optischen Eigenschaften zeigen ein großes Potential für biosensorische Anwendungen. In dieser Arbeit wurde eine marker-freie Detektion von Biomolekülen in Echtzeit mit Hilfe von immobilisierten Nanopartikeln in einer mikrofluidischen Kammer gezeigt. Zwei experimentelle Anordnungen mit dicht immobilisierten (LSPR) und einzelnen Nanostrukturen (sLSPR) wurden mit einem Fluidsteuerungssystem kombiniert und mit einem kommerziell erhältlichen System verglichen (SPR). Die experimentell bestimmte Sensitivität bei Brechungsindexänderungen war für die sphärischen und anisotropischen Nanostrukturen in Konsens mit den Daten in der Literatur. Die Ergebnisse haben auch bestätigt, dass anisotropische Nanostrukturen eine höhere Sensitivität aufzeigen.

Die Oberflächensensitivität der drei untersuchten Systeme wurde mit PEL-Schichten und Protein-Multischichten bestimmt. Die Messungen haben gezeigt, dass das LSPR-Signal, im Gegensatz zum SPR-Signal, eine nicht-lineare Abhängigkeit bei der Adsorption der Schichten aufweist. Außerdem konnte gezeigt werden, dass die Änderung des LSPR-Signals von der Größe der Nanopartikel und der Plasmonmode abhängt und insgesamt höher ist, als beim SPR system. Das erhöhte Rauschsignal bei dem LSPR System konnte durch die höhere Oberflächensensitivität kompensiert werden.

Die Adsorption der Polyelektrolytschichten und Protein-Multischichten konnte auch erfolgreich in Echtzeit auf einer Fläche kleiner als $0.02\,\mu m^2$ auf einem einzelnen 80 nm sphärischen Nanopartikel detektiert werden. Das Rauschsignal war jedoch viel höher verglichen zu den anderen Systemen hervorgerufen durch die geringere Intensität des gestreuten Lichtes des Nanopartikels und aufgrund von mechanischer Instabilitäten. Das geringe Signal-Rausch-Verhältnis hat gezeigt, dass der verwendete Messbau nicht für DNA-Messungen geeignet ist.

Eine Echtzeit-Detektion von DNA-DNA Bindung konnte mit dem LSPR System mit 80 nm sphärischen Gold-Nanopartikeln gezeigt werden. Zwei verschiedene DNA Sequenzen wurden erfolgreich kovalent auf den Nanopartikeln als Fänger-DNA gebunden und die anschließende Hybridisierung war innerhalb von 5 Minuten bei Raumtemperatur detektierbar. Messungen mit unspezifischer DNA haben die hohe Spezifität der DNA Bindung bestätigt und die Hybridisierung war durch eine Lauge-Denaturierung wiederholbar. Untersuchungen bezüglich des Puffers während der Biofunktionalisierung, der Reinigung der Substrate mit Plasmaätzen und der Coadsorption von Merkaptohexanol haben zu einer erhöhten Adsorption und Erreichbarkeit der Fänger-DNA geführt. Obwohl die direkte Adsorption von Fänger-DNA mit

poly(A)-Schwanz in der Literatur beschrieben wird, war diese Methode auf immobilisierte Nanopartikel nicht anwendbar. Die Anziehungskräfte zwischen den Nukleotiden und der Gold-Oberfläche waren zu gering.

Thiol-modifizierte DNA, die eine G-quadruplex Struktur bilden kann, wurde erfolgreich auf den Nanopartikeln adsorbiert. Aber es konnte nicht nachgewiesen werden, ob die 3D Struktur nach dem Pufferwechsel vorhanden war bzw. ob Hämin an der DNA Struktur gebunden hat. Weitere Untersuchungen müssen mit DNAzymen und immobilisierten Nanopartikeln durchgeführt werden.

List of Figures

References

[1] Robert S. Marks, David C. Cullen, Isao Karube, Christopher R. Lowe, and Howard H Weetall. *Handbook of Biosensors and Biochips*, volume 1. John Wiley & Sons Chichester, UK, 2007.

[2] Alexandre G. Brolo. Plasmonics for future biosensors. *Nature Photonics*, 6(11):709–713, 2012.

[3] Leland C. Clark. Monitor and control of blood and tissue oxygen tensions. *Transactions American Society for Artificial Internal Organs*, (2):41–48, 1956.

[4] Leland C. Clark and Champ Lyons. Electrode systems for continous monitoring in cardiovascular surgery. *Annals of the New York Academy of Sciences*, (102):29–45, 1962.

[5] Anthony P. F. Turner. Biosensors: sense and sensibility. *Chemical Society Review*, 42:3184–3196, 2013.

[6] Borja Sepúlveda, Paula C. Angelomé, Laura M. Lechuga, and Luis M. Liz-Marzán. Lspr-based nanobiosensors. *Nano Today*, 4(3):244–251, 2009.

[7] Reinhard Renneberg, Dorothea Pfeiffer, Fred Lisdat, George Wilson, Ulla Wollenberger, Frances Ligler, and Anthony P. F. Turner. *Frieder Scheller and the Short History of Biosensors*, volume 109 of *Advances in Biochemical Engineering/Biotechnology*. Springer Berlin Heidelberg, 2008.

[8] Alexandre Dmitriev. *Nanoplasmonic Sensors*. Number 1. Springer-Verlag New York, 2012.

[9] Paul D'Orazio. Biosensors in clinical chemistry. *Clinica Chimica Acta*, 334(1):41 – 69, 2003.

[10] William E. Moerner. New directions in single-molecule imaging and analysis. *Proceedings of the National Academy of Sciences*, 104(31):12596–12602, 2007.

[11] Xudong Fan, Ian M. White, Siyka I. Shopova, Hongying Zhu, Jonathan D. Suter, and Yuze Sun. Sensitive optical biosensors for unlabeled targets: A review. *Analytica Chimica Acta*, 620:8 – 26, 2008.

[12] Jiří Homola. Present and future of surface plasmon resonance biosensors. *Analytical and Bioanalytical Chemistry*, 377(3):528–539, 2003.

[13] Audrey Sassolas, Béatrice D. Leca-Bouvier, and Loïc J. Blum. DNA biosensors and microarrays. *Chemical Reviews*, 108(1):109–139, 2008.

[14] Xiaowei Guo. Surface plasmon resonance based biosensor technique: A review. *Journal of Biophotonics*, 5(7):483–501, 2012.

[15] Stefan Maier. *Plasmonics: Fundamentals and Applications*. Springer, 2007.

[16] Heather K. Hunt and Andrea M. Armani. Label-free biological and chemical sensors. *Nanoscale*, 2:1544–1559, 2010.

[17] Jiří Homola. *Surface Plasmon Resonance Based Sensors*. Springer Berlin Heidelberg, 2006.

[18] Jiří Homola, Sinclair S. Yee, and Günter Gauglitz. Surface plasmon resonance sensor: review. *Sensor and Actuators B*, 54:3–15, 1999.

[19] Chad A. Mirkin, Robert L. Letsinger, Robert C. Mucic, and James J. Storhoff. A DNA-based method for rationally assembling nanoparticles into macroscopic materials. *Nature*, (382):607–609, 1996.

[20] Armand P. Alivisatos. Semiconductor clusters, nanocrystals, and quantum dots. *Science*, 271:933–937, 1996.

[21] Francis P. Zamborini, Lanlan Bao, and Radhika Dasari. Nanoparticles in measurement science. *Analytical Chemistry*, 84(2):541–576, 2012.

[22] Kathryn M. Mayer and Jason H. Hafner. Localized surface plasmon resonance sensors. *Chemical Reviews*, 111(6):3828–3857, 2011.

[23] Xianmao Lu, Matthew Rycenga, Sara E. Skrabalak, Benjamin Wiley, and Younan Xia. Chemical synthesis of novel plasmonic nanoparticles. *Annual Review of Physical Chemistry*, 60(1):167–192, 2009.

[24] Gustav Mie. Beiträge zur Optik trüber Medien speziell kolloidaler Metallösungen. *Annalen Der Physik*, 25:377–445, 1908.

[25] Uwe Kreibig and Michael Vollmer. *Optical Properties of Metal Clusters*, volume 25 of *Series in Materials Science*. Berlin, 1995.

[26] Craig F. Bohren and Donald R. Huffman. *Absorption and Scattering of Light by small Particles*. John Willey & Sons, Inc., 1983.

[27] Prashant K. Jain, Kyeong Seok Lee, Ivan H. El-Sayed, and Mostafa A. El-Sayed. Calculated absorption and scattering properties of gold nanoparticles of different size, shape, and composition: Applications in biological imaging and biomedicine. *The Journal of Physical Chemistry B*, 110(14):7238–7248, 2006.

[28] Katherine A. Willets and Richard P. Van Duyne. Localized surface plasmon resonance spectroscopy and sensing. *Annual Review of Physical Chemistry*, 58(1):267–297, 2007.

[29] Eleonora Petryayeva and Ulrich J. Krull. Localized surface plasmon resonance: Nanostructures, bioassays and biosensing - a review. *Analytica Chimica Acta*, 706(1):8 – 24, 2011.

[30] Kyoungweon Park. *Synthesis, Characterization, and Self Assembly of Size Tunable Gold Nanorods*. PhD thesis, Georgia Institute of Technology, 2006.

[31] Luis M. Liz-Marzán. Tailoring surface plasmons through the morphology and assembly of metal nanoparticles. *Langmuir*, 22(1):32–41, 2006.

[32] Adam D. McFarland and Richard P. Van Duyne. Single silver nanoparticles as real-time optical sensors with zeptomole sensitivity. *Nano Letters*, 3(8):1057–1062, 2003.

[33] Celine I.L. Justino, Ana C. Freitas, Ruth Pereira, Armando C. Duarte, and Teresa A.P. Rocha Santos. Recent developments in recognition elements for chemical sensors and biosensors. *Trends in Analytical Chemistry*, 68:2 – 17, 2015.

[34] James Chambers, Bernard Arulanandam, Leann L. Matta, Alex Weis, and James Valdes. Biosensor recognition elements. *Current Issues Molecular Biology*, 10:1–12, 2008.

[35] Yoon-Kyoung Cho, Sunhee Kim, Young A Kim, Hee Kyun Lim, Kyusang Lee, Dae-Sung Yoon, Geunbae Lim, Eugene Pak, Tai Hwan Ha, and Kwan Kim. Characterization of DNA immobilization and subsequent hybridization using in situ quartz crystal microbalance, fluorescence spectroscopy, and surface plasmon resonance. *Journal of Colloid and Interface Science*, 278(1):44 – 52, 2004.

[36] Joseph Wang. Survey and Summary: From DNA biosensors to gene chips. *Nucleic Acids Research*, 28(16):3011–3016, 2000.

[37] James D. Watson and Francis H. C. Crick. A structure for deoxyribose nucleic acid. *Nature*, (171):737–738, 1953.

[38] Juewen Liu. Adsorption of DNA onto gold nanoparticles and graphene oxide: surface science and applications. *Physical Chemistry Chemical Physics*, 14:10485–10496, 2012.

[39] Fredrik Höök, Arghya Ray, Bengt Nordén, and Bengt Kasemo. Characterization of PNA and DNA Immobilization and Subsequent Hybridization with DNA Using Acoustic-Shear-Wave Attenuation Measurements. *Langmuir*, 17(26):8305–8312, 2001.

[40] Ann C. Pease, Dennis Solas, Edward J. Sullivan, Maureen T. Cronin, Christopher P. Holmes, and Stephen P. Fodor. Light-generated oligonucleotide arrays for rapid DNA sequence analysis. *Proceedings of the National Academy of Sciences*, 91(11):5022–5026, 1994.

[41] Uwe Maskos and Edwin M. Southern. A study of oligonucleotide reassociation using large arrays of oligonucleotides synthesised on a glass support. *Nucleic Acids Research*, 21(20):4663–4669, 1993.

[42] Newton C. Fawcett, Jeffrey A. Evans, Liang-Chy Chien, and Naomi Flowers. Nucleic acid hybridization detected by piezoelectric resonance. *Analytical Letters*, (21):1099–1114, 1988.

[43] Hadi Ravan, Soheila Kashanian, Nima Sanadgol, Arastoo Badoei-Dalfard, and Zahra Karami. Strategies for optimizing DNA hybridization on surfaces. *Analytical Biochemistry*, 444(0):41 – 46, 2014.

[44] XanTec bioanalytics GmbH. SPR Sensor chips, 02 2016.

[45] GE Healthcare Bio-Sciences AB. *Biacore - Sensor Surface Handbook*. GE Healthcare Bio-Sciences, BR-1005-71 AB 05 edition, 2008.

[46] Alexander W. Peterson, Richard J. Heaton, and Rosina M. Georgiadis. The effect of surface probe density on DNA hybridization. *Nucleic Acids Research*, 29(24):5163–5168, 2001.

[47] Onur Tokel, Fatih Inci, and Utkan Demirci. Advances in plasmonic technologies for point of care applications. *Chemical Reviews*, 114(11):5728–5752, 2014.

[48] F. Teles and Luis P. Fonseca. Trends in DNA biosensors. *Talanta*, 77(2):606 – 623, 2008.

[49] Kevin A. Peterlinz, Rosina M. Georgiadis, Tonya M. Herne, and Michael J. Tarlov. Observation of hybridization and dehybridization of thiol-tethered DNA using two-color surface plasmon resonance spectroscopy. *Journal of the American Chemical Society*, 119(14):3401–3402, 1997.

[50] V. S. Dilimon, Sundar Rajalingam, Joseph Delhalle, and Zineb Mekhalif. Self-assembly mechanism of thiol, dithiol, dithiocarboxylic acid, disulfide and diselenide on gold: an electrochemical impedance study. *Physical Chemistry Chemical Physics*, 15:16648–16656, 2013.

[51] Christopher Love, Lara A. Estroff, Jennah K. Kriebel, Ralph G. Nuzzo, and George M. Whitesides. Self-assembled monolayers of thiolates on metals as a form of nanotechnology. *Chemical Reviews*, 105(4):1103–1170, 2005.

[52] Xu Zhang, Biwu Liu, Neeshma Dave, Mark R. Servos, and Juewen Liu. Instantaneous attachment of an ultrahigh density of nonthiolated DNA to gold nanoparticles and its applications. *Langmuir*, 28(49):17053–17060, 2012.

[53] Hiromi Kimura-Suda, Dmitri Y. Petrovykh, Michael J. Tarlov, and Lloyd J. Whitman. Base-dependent competitive adsorption of single-stranded DNA on gold. *Journal of the American Chemical Society*, 125(30):9014–9015, 2003.

[54] Aric Opdahl, Dmitri Y. Petrovykh, Hiromi Kimura-Suda, Michael J. Tarlov, and Lloyd J. Whitman. Independent control of grafting density and conformation of single-stranded DNA brushes. *Proceedings of the National Academy of Sciences*, 104(1):9–14, 2007.

[55] Sarah M. Schreiner, David F. Shudy, Anna L. Hatch, Aric Opdahl, Lloyd J. Whitman, and Dmitri Y. Petrovykh. Controlled and efficient hybridization achieved with DNA probes immobilized solely through preferential dna-substrate interactions. *Analytical Chemistry*, 82(7):2803–2810, 2010.

[56] Hao Pei, Fan Li, Ying Wan, Min Wei, Huajie Liu, Yan Su, Nan Chen, Qing Huang, and Chunhai Fan. Designed diblock oligonucleotide for the synthesis of spatially isolated and highly hybridizable functionalization of dna-gold nanoparticle nanoconjugates. *Journal of the American Chemical Society*, 134(29):11876–11879, 2012.

[57] Nak-Han Jang. The coordination chemistry of DNA nucleosides on gold nanoparticles as a probe by SERS. *Bulletin of the Korean Chemical Society*, 23:1790–1800, 2002.

[58] Thomas Doneux and Lukáš Fojt. Interaction of cytidine 5'-monophosphate with Au(111): An in situ infrared spectroscopic study. *ChemPhysChem*, 10(9-10):1649–1655, 2009.

[59] Kristin B. Cederquist and Christine D. Keating. Curvature effects in DNA:Au nanoparticle conjugates. *ACS Nano*, 3(2):256–260, 2009.

[60] Adam B. Steel, Rastislav L. Levicky, Tonya M. Herne, and Michael J. Tarlov. Immobilization of nucleic acids at solid surfaces: effect of oligonucleotide length on layer assembly. *Biophysical Journal*, 79(2):975–981, 2000.

[61] Haley D. Hill, Jill E. Millstone, Matthew J. Banholzer, and Chad A. Mirkin. The role radius of curvature plays in thiolated oligonucleotide loading on gold nanoparticles. *ACS Nano*, 3(2):418–424, 2009.

[62] Tonya M. Herne and Michael J. Tarlov. Characterization of DNA probes immobilized on gold surfaces. *Journal of the American Chemical Society*, 119(38):8916–8920, 1997.

[63] Rastislav Levicky, Tonya M. Herne, Michael J. Tarlov, and Sushil K. Satija. Using self-assembly to control the structure of DNA monolayers on gold: A neutron reflectivity study. *Journal of the American Chemical Society*, 120(38):9787–9792, 1998.

[64] Sunho Park, Katherine A. Brown, and Kimberly Hamad-Schifferli. Changes in oligonucleotide conformation on nanoparticle surfaces by modification with mercaptohexanol. *Nano Letters*, 4(10):1925–1929, 2004.

[65] Stefan Lorkowski, Gerhard Lorkowski, and Paul Cullen. Biochips: Das Labor in der Streichholzschachtel. *Chemie in unserer Zeit*, 34(6):356 – 372, 2000.

[66] Helen J. Watts, Debra Yeung, and Helen Parkes. Real-time detection and quantification of DNA hybridization by an optical biosensor. *Analytical Chemistry*, 67(23):4283–4289, 1995.

[67] Rüdiger Benters, Christof M. Niemeyer, Denja Drutschmann, Dietmar Blohm, and Dieter Wöhrle. DNA microarrays with PAMAM dendritic linker systems. *Nucleic Acids Research*, 30(2), 2002.

[68] Sara Tombelli, Maria Minunni, and Marco Mascini. Analytical applications of aptamers. *Biosensors and Bioelectronics*, 20(12):2424 – 2434, 2005.

[69] Alexander Jung, Irene Stemmler, Andreas Brecht, and Günter Gauglitz. Covalent strategy for immobilization of DNA-microspots suitable for microarrays with label-free and time-resolved optical detection of hybridization. *Fresenius' Journal of Analytical Chemistry*, 371(2):128–136, 2014.

[70] Branislav Ruttkay-Nedecky, Jiri Kudr, Lukas Nejdl, Darina Maskova, Rene Kizek, and Vojtech Adam. G-quadruplexes as sensing probes. *Molecules*, 18(12):14760–14779, 2013.

[71] Joanna Kosman and Bernard Juskowiak. Peroxidase-mimicking DNAzymes for biosensing applications: A review. *Analytica Chimica Acta*, 707(1):7 – 17, 2011.

[72] Sarah Burge, Gary N. Parkinson, Pascale Hazel, Alan K. Todd, and Stephen Neidle. Quadruplex DNA: sequence, topology and structure. *Nucleic Acids Research*, 34(19):5402–5415, 2006.

[73] Yingfu Li and Dipankar Sen. Toward an efficient DNAzyme. *Biochemistry*, 36(18):5589–5599, 1997.

[74] Paola Travascio, Yingfu Li, and Dipankar Sen. DNA-enhanced peroxidase activity of a DNA aptamer-hemin complex. *Chemistry & Biology*, 5(9):505 – 517, 1998.

[75] Itamar Willner, Bella Shlyahovsky, Maya Zayats, and Bilha Willner. DNAzymes for sensing, nanobiotechnology and logic gate applications. *Chemical Society Review*, 37:1153–1165, 2008.

[76] Joanna Kosman and Bernard Juskowiak. Optimization study of the catalytic activity of DNAzymes based on telomeric G-quadruplexes. *Central European Journal of Chemistry*, (2), 2011.

[77] Julian L. Huppert. Hunting G-quadruplexes. *Biochimie*, 90(8):1140 – 1148, 2008.

[78] Andreas B. Dahlin, Jonas O. Tegenfeldt, and Fredrik Höök. Improving the instrumental resolution of sensors based on localized surface plasmon resonance. *Analytical Chemistry*, 78(13):4416–4423, 2006.

[79] Carsten Sönnichsen. *Plasmons in metal nanostructures*. PhD thesis, July 2001.

[80] Erik Martinsson, Mohammad Mehdi Shahjamali, Karin Enander, Freddy Boey, Can Xue, Daniel Aili, and Bo Liedberg. Local refractive index sensing based on edge gold-coated silver nanoprisms. *The Journal of Physical Chemistry C*, 117(44):23148–23154, 2013.

[81] Ludovic S. Live and Jean-Francois Masson. High sensitivity of plasmonic microstructures near the transition from short-range to propagating surface plasmon. *The Journal of Physical Chemistry C*, 113(23):10052–10060, 2009.

[82] Pavel Kvasnička and Jiří Homola. Optical sensors based on spectroscopy of localized surface plasmons on metallic nanoparticles: Sensitivity considerations. *Biointerphases*, 3(3):FD4–FD11, 2008.

[83] Jacqueline Jatschka, André Dathe, Andrea Csáki, Wolfgang Fritzsche, and Ondrej Stranik. Propagating and localized surface plasmon resonance sensing ? a critical comparison based on measurements and theory. *Sensing and Bio-Sensing Research*, 7(Supplement C):62 – 70, 2016.

[84] Janos Vörös. The density and refractive index of adsorbing protein layers. *Biophysical Journal*, 87(1):553–561, 2004.

[85] Peter Nordlander, C. Oubre, Emil Prodan, K. Li, and Mark I. Stockman. Plasmon hybridization in nanoparticle dimers. *Nano Letters*, 4(5):899–903, 2004.

[86] Alastair Cunningham, Stefan Mühlig, Carsten Rockstuhl, and Thomas Bürgi. Coupling of plasmon resonances in tunable layered arrays of gold nanoparticles. *The Journal of Physical Chemistry C*, 115(18):8955–8960, 2011.

[87] Jill E. Millstone, Sarah J. Hurst, Gabriella S. Métraux, Joshua I. Cutler, and Chad A. Mirkin. Colloidal gold and silver triangular nanoprisms. *Small*, 5(6):646–664, 2009.

[88] Carsten Sönnichsen, N. Geier, N. E. Hecker, G. von Plessen, and J. Feldmann. Spectroscopy of single metallic nanoparticles using total internal reflection microscopy. *Applied Physics Letters*, 77(19):2949–2951, 2000.

[89] Rosina Georgiadis, Kevin A. Peterlinz, and Alexander W. Peterson. Quantitative measurements and modeling of kinetics in nucleic acid monolayer films using SPR spectroscopy. *Journal of the American Chemical Society*, 122(13):3166–3173, 2000.

[90] S. Link, Z. L. Wang, and M. A. El-Sayed. Alloy formation of gold-silver nanoparticles and the dependence of the plasmon absorption on their composition. *Journal of Physical Chemistry B*, 103(18):3529–3533, 1999.

[91] Amanda J. Haes, Shengli Zou, George C. Schatz, and Richard P. Van Duyne. Nanoscale optical biosensor: Short range distance dependence of the localized surface plas-

mon resonance of noble metal nanoparticles. *The Journal of Physical Chemistry B*, 108(22):6961–6968, 2004.

[92] Amanda J. Haes, Shengli Zou, George C. Schatz, and Richard P. Van Duyne. A nanoscale optical biosensor: The long range distance dependence of the localized surface plasmon resonance of noble metal nanoparticles. *The Journal of Physical Chemistry B*, 108(1):109–116, 2004.

[93] Matthias Thiele, Isabell Götz, Steffen Trautmann, Robert Müller, Andrea Csáki, Thomas Henkel, and Wolfgang Fritzsche. Wet-chemical passivation of anisotropic plasmonic nanoparticles for LSPR-sensing by a silica shell. *Materials Today: Proceedings*, 2(1):33 – 40, 2015.

[94] Gero Decher and Joe B. Schlenoff. *Multilayer Thin Films Sequential Assembly of Nanocomposite Materials*. WILEY-VCH Verlag GmbH, 2003.

[95] Frank Caruso, Kenichi Niikura, D. Neil Furlong, and Yoshio Okahata. Ultrathin multilayer polyelectrolyte films on gold: Construction and thickness determination. *Langmuir*, 13:3422–3426, 1997.

[96] Kurosch Rezwan, Lorenz P. Meier, Mandana Rezwan, Janos Vörös, Marcus Textor, and Ludwig J. Gauckler. Bovine Serum Albumin adsorption onto colloidal Al_2O_3 particles: A new model based on zeta potential and UV-Vis measurements. *Langmuir*, 20(23):10055–10061, 2004.

[97] Florian Horn. *Biochemie des Menschen: Das Lehrbuch für das Medizinstudium*. Thieme Verlag, 2006.

[98] Thomas Schneider, Norbert Jahr, Jacqueline Jatschka, Andrea Csáki, Ondrej Stranik, and Wolfgang Fritzsche. Localized surface plasmon resonance (LSPR) study of DNA hybridization at single nanoparticle transducers. *Journal of Nanoparticle Research*, 15(4):1–10, 2013.

[99] Pär Sandström, Mila Boncheva, and Björn Åkerman. Nonspecific and thiol-specific binding of DNA to gold nanoparticles. *Langmuir*, 19(18):7537–7543, 2003.

[100] Xiaofang Wang, Hyun Jeong Lim, and Ahjeong Son. Characterization of denaturation and renaturation of DNA for DNA hybridization. *Environmental Health and Toxicology*, 29(0):e2014007–0, 2014.

[101] Jiayun Zhang, Hans Peter Lang, Genki Yoshikawa, and Christoph Gerber. Optimization of DNA hybridization efficiency by pH-driven nanomechanical bending. *Langmuir*, 28(15):6494–6501, 2012.

[102] Thomas Schüler, Andrea Steinbrück, Grit Festag, Robert Möller, and Wolfgang Fritzsche. Enzyme-induced growth of silver nanoparticles studied on single particle level. *Journal of Nanoparticle Research*, 11(4):939–946, 2009.

Appendix

Chemicals

Chemical	Purity, Concentration	Manufacturer
Acetic acid	100% p.a.	Carl Roth GmbH & Co. KG , Germany
Acetone		Carl Roth GmbH & Co. KG , Germany
(3-Aminopropyl)triethoxysilane (APTES)	98 %, 25 g	abcr GmbH, Germany
Bovine Serum Albumin	$\geq$ 98%, Fraktion V, M_w~69 000	Carl Roth GmbH & Co. KG , Germany
Citric acid monohydrate	for analysis	Merck KGaA, Germany
Dextrane sulfate	Sodium salt from Leuconostoc ssp.	Fluka BioChemika
Ethanol	pro analysi; denatured with 1% methyl ethyl ketone	Merck KGaA, Germany
D-(+)-Glucose	$\geq$ 99.5%	Sigma Aldrich
Glycerol	~ 87%, GR for analysis	Merck KGaA, Germany
Hemin		Sigma Aldrich
Hydrochloric acid	37%	Merck KGaA, Germany
6-Mercapto-1-hexanol	97%	Sigma Aldrich
Poly(allylamine hydrochloride)	M_w~58 000	Sigma Aldrich
Poly(sodium 4-styrenesulfonate)	M_w~70 000	Sigma Aldrich
Potassium dihydrogen phosphate	$\geq$ 99%, p.a., ACS	Carl Roth GmbH & Co. KG , Germany
Sodium chloride	> 99.8%, M = 58,44 g/mol	Carl Roth GmbH & Co. KG , Germany
Sodium hydroxide	$\geq$ 99%, p.a., ISO	Carl Roth GmbH & Co. KG , Germany
20 x SSC	Roti-Stock, steam sterilized	Carl Roth GmbH & Co. KG , Germany
Trisodiumcitratedihydrate	$\geq$ 99%, p.a., ACS	Carl Roth GmbH & Co. KG , Germany

Buffer and solution preparation

- Citrate Buffer for BSA and DS measurements:
  4.7 g of Trisodiumcitratedihydrate dissolved in 170 ml $3dH_2O$
  pH adjusted to 4.0 by dissolving of 5.1 g citric acid
  fill up to 200 ml with $3dH_2O$
- BSA: 7.33 mg in 50 ml citrate buffer pH = 4.0
- DS: 5 mg in 50 ml citrate buffer pH = 4.0
- 0.5 M Citrate buffer pH = 3.0 for DNA measurments:
  29.409 g of Trisodiumcitratedihydrate dissolved in 200 ml $3dH_2O$
  pH adjusted to 3.0 with HCl

Additional results

Stability test of nanoprisms

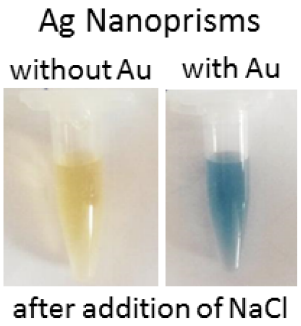

Figure 6.1: Silver nanoprisms in solution with (right) and without gold edges (left) after addition of NaCl for stability test.

Effect of different concentrations of capture DNA

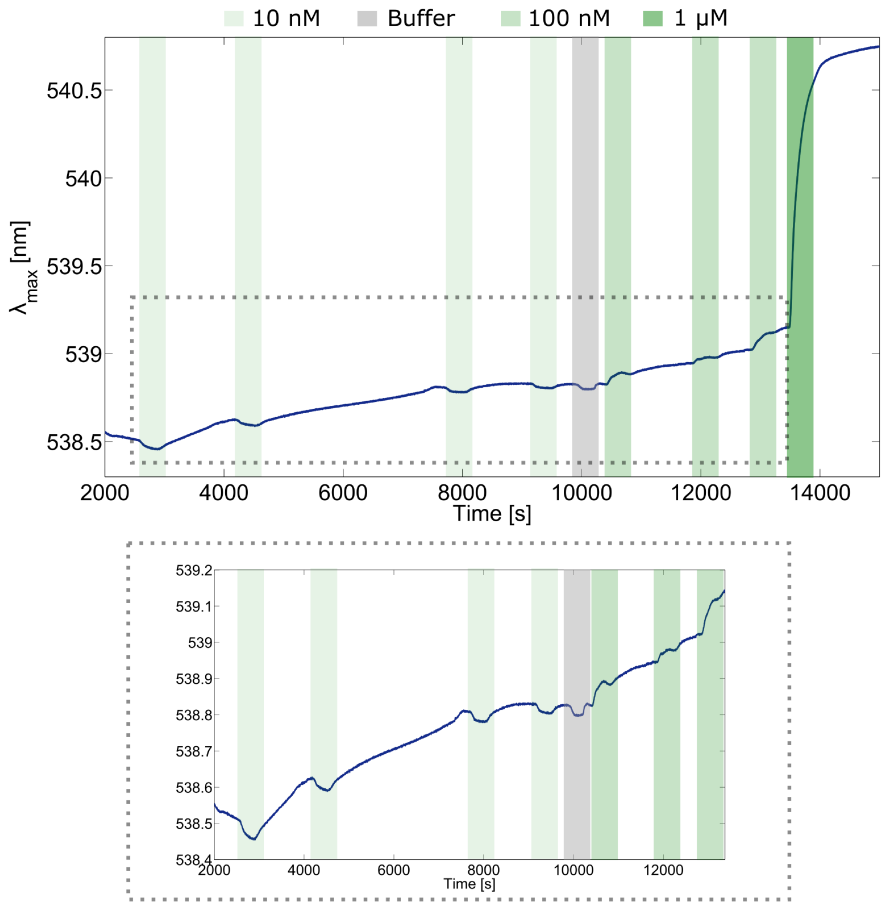

Figure 6.2: Sensogram of capture DNA adsorption with different concentrations. Solutions with 10 nM, 100 nM and 1 μM were subsequently infused into the microfluidic chamber.

Sensogram of sensor regeneration with NaOH

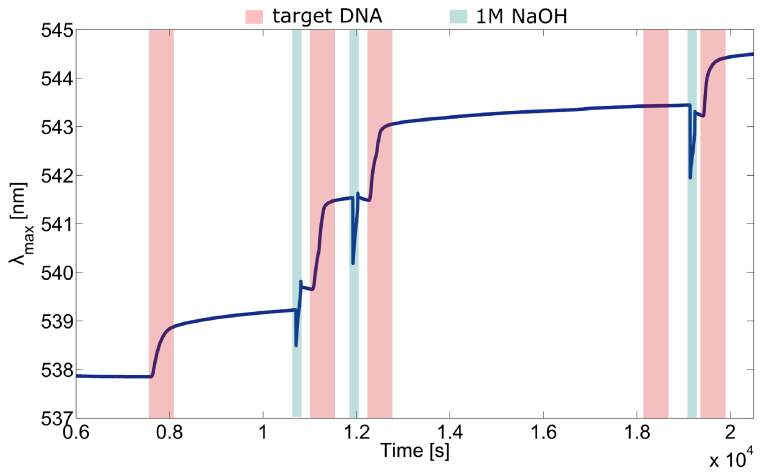

Figure 6.3: Sensogram of the regeneration of the LSPR transducer with 1 M NaOH. The sensor was several times denaturated and regenerated.

Sensogram of PCR product detection

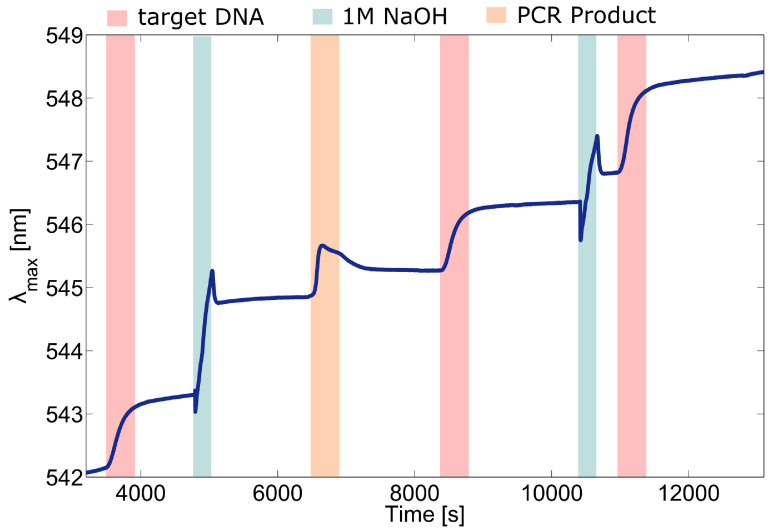

Figure 6.4: Detection of PCR product on gold 80 nm nanoparticle layer. For reference the synthetic target DNA was infused in advance.

Acknowledgements

If you talk to a man in a language he understands, that goes to his head.
If you talk to him in his language, that goes to his heart. – Nelson Mandela

In this sense, I want to thank everybody who supported me during my doctorate journey in my mother tongue.

Herrn Prof. Dr. Stefan H. Heinemann danke ich für die Betreuung seitens der Friedrich-Schiller-Universität Jena und vor allem für die Unterstützung bei der Finalisierung der Dissertation.

Mein herzlichster Dank gilt PD Dr. Wolfgang Fritzsche für die Bereitstellung des Promotionsthemas und die Betreuung in der Arbeitsgruppe Nanobiophotonik am Leibniz-Institut für photonische Technologien. Er hat durch sein besonnenes Wesen und seine Freundlichkeit immer Zuversicht ausgestrahlt. Vielen Dank auch für die vielen Reisemöglichkeiten, durch die ich die wissenschaftliche Praxis in anderen Ländern kennen lernen durfte.

Ich möchte mich herzlich bei Dr. Ondrej Stranik für die umfangreiche Betreuung bedanken. Er hatte immer neue kreative Ideen, hat mich bei wissenschaftlichen, experimentellen und vor allem physikalischen Fragen stets unterstützt.

Ein großer Dank gilt auch Dr. Andrea Csáki für das zu Hause, dass sie mir am Anfang der Promotion gegeben hat, die unermüdliche Organisationsarbeit bezüglich der Projekte und die Möglichkeit jederzeit Fragen zu stellen.

Bei Franka Jahn möchte ich mich für die zuverlässigen Aufnahmen mit dem Elektronenmikroskop bedanken und für die Organisation der Seminarfahrten und der eigenen Tagungen. Sie hat uns ermöglicht entspannte und abwechslungsreiche Tage zu verbringen.

Prof. Dr. Eulália Pereira, Prof. Ding Ping Tsai, Prof. Dr. Bernard Juskowiak und ihren Arbeitsgruppen möchte ich danken für die angenehmen Aufenthalte und das näher bringen ihrer Kultur. Im Speziellen möchte ich mich bei Dr. Joanna Kosman für die Zusammenarbeit bezüglich der "DNAzymes" bedanken.

Von ganzem Herzen gilt der Dank meiner "Doktoranden-Generation" für eine unvergessliche Zeit. David Zopf möchte ich für die tiefe Freundschaft und den Beistand bei Höhen und Tiefen danken und, dass er meine Arbeit mehrmals Korrektur gelesen hat. Stefanie Hentschel sage ich von ganzem Herzen Danke für die enge Freundschaft, das stets offene Ohr und die Fürsorge. Dr. Frank Theil möchte ich für die Synthese der "nanopeanuts" und die täglichen Umarmungen, die vor allem bei schlechten Tagen Balsam für die Seele waren, danken. Bei Matthias Thiele bedanke ich mich für die Synthese der Nanoprismen, die fachlichen und nicht-fachlichen Gespräche und die positive Ausstrahlung. André Dathe möchte ich für die Unterstützung bei den Labview und Matlab-Skripten danken, im Speziellen für die Software

bei den sLSPR Messungen. Ohne ihn hätte ich die Ergebnisse nicht in der Form produzieren können. Außerdem danke ich Dr. Andy Wolff für die lustigen Gespräche, die aufbauenden Worte und die Freitag-Früh Tradition. Vielen Dank auch an meine Bürokollegin Eileen Heinrich für die Hilfe im Chemielabor als auch den unterhaltsamen Gesprächen im Büro. Ihr ward wie eine Familie für mich und habt den Arbeitsplatz zu einem zu Hause gemacht.

Bei allen weiteren Mitarbeiterinnen und Mitarbeitern der Abteilung und des IPHTs möchte ich mich für die Zusammenarbeit und die unvergesslichen Weihnachtsfeiern und deren Vorbereitungen bedanken.

Meiner Familie gilt besonderer Dank. Sie hat mir Halt gegeben, mich stets auf meinem Weg unterstützt und mir den Freiraum gegeben meinen eigenen Weg zu gehen.
Danke.

Eigenständigkeitserklärung

Hiermit erkläre ich, dass mir die geltende Promotionsordnung der Fakultät bekannt ist, und ich die vorliegende Arbeit selbstständig und nur unter Verwendung der angegebenen Hilfsmittel und Literatur angefertigt und bisher keiner anderen Hochschule als Dissertation oder Prüfungsarbeit vorgelegt habe. Ich habe weder die Hilfe eines Promotionsberaters in Anspruch genommen, noch unmittelbar oder mittelbar geldwerte Leistungen in Zusammenhang mit dem Inhalt meiner Dissertation an Dritte erbracht.

Jacqueline Jatschka